

TECHNISCHE UNIVERSITÄT MÜNCHEN

MAX-PLANCK-INSTITUT
FÜR
ASTROPHYSIK

**Two- and Three-Dimensional Simulations
of Core-Collapse Supernova Explosions of
Massive Stars Applying Neutrino
Hydrodynamics**

Florian Hanke

Vollständiger Abdruck der an die Fakultät für Physik der Technischen Universität München
zur Erlangung des akademischen Grades eines

Doktors der Naturwissenschaften (Dr. rer. nat.)

genehmigten Dissertation.

Vorsitzende: Univ.-Prof. Dr. Elisa Resconi
Prüfer der Dissertation: 1. Priv.-Doz. Dr. Hans-Thomas Janka
 2. Univ.-Prof. Dr. Björn Garbrecht

Die Dissertation wurde am 14.04.2014 bei der Technischen Universität München
eingereicht und durch die Fakultät für Physik
am 02.07.2014 angenommen.

Contents

1	Introduction	1
1.1	The Paradigm of the Delayed Neutrino-driven Explosion Mechanism	1
1.2	The Importance of Hydrodynamic Instabilities	2
1.3	Advancing to Three-dimensional Modeling	4
1.4	Organization of this Thesis	5
2	The Vertex-Prometheus Neutrino Radiation Hydrodynamics Code	7
2.1	The Hydrodynamics Part: The PROMETHEUS Code	8
2.1.1	Numerical Solution	9
2.1.2	Treatment of Self-Gravity	10
2.1.3	Equation of State	10
2.2	The Neutrino Radiation Part: the VERTEX Code	12
2.2.1	Overview	12
2.2.2	The System of Equations	13
2.2.3	Method of Solution	15
2.2.4	Coupling to the Hydrodynamics	18
3	The Progenitor Structure Dependence of the Explosion Mechanism in Axisymmetry	21
3.1	Overview of the investigated Set of axisymmetric Simulations	22
3.2	Dependence of the Postbounce Evolution on the Precollapse Structure	25
3.3	Conditions in the Gain Layer	30
3.4	The Concept of a Critical Curve	35
3.5	Driver of the Explosion, the Growth of Instabilities	38
3.6	Shock Expansion and Explosion Energy	45
3.7	Investigation of Models based on the Presupernova Models of Woosley & Heger (2007)	48
3.8	Summary of the Results based on our Axisymmetric Simulations	50
4	The Dependence of the Postbounce Evolution on the Grid Setup in Axisymmetry	53
4.1	The Influence of Numerical Resolution	53
4.2	A slightly simplified setup	55
5	SASI Activity and Convective Overturn in Fully Self-consistent 3D Core-Collapse Supernova Simulations	59
5.1	Numerical Methods and Modeling Setup of our 3D Simulations	62
5.2	SASI Activity in 3D Models and its Comparison to 2D	64
5.3	The Spiral Mode of the SASI	76
5.4	Revival of SASI Activity	80

5.5	Runaway Conditions and Explosion Indicators	83
5.6	Turbulent Mass Motions and the Rise of Buoyant Plumes	87
5.7	Discussion and Conclusions	91
6	A Purely Convective model: The $11.2 M_{\odot}$ SN Progenitor	97
6.1	Shock Propagation and Heating Conditions	97
6.2	Growth of Convection and the Suppression of SASI Activity	101
7	Summary and Conclusions	105
	Bibliography	109

1 Introduction

Core-collapse supernova explosions are the catastrophic deaths of stars, with more than about eight times the mass of our sun. They are among the most powerful cosmic events. During such an explosion more energy is released in a few seconds than the star has previously emitted by radiation over its whole lifetime. These events are highly complex phenomena, where a variety of physical ingredients, such as fluid dynamics, relativistic gravity, weak interactions, nuclear reactions, and the thermodynamics of nonrelativistic and relativistic plasmas of arbitrary degeneracy play a role in the gravitational collapse of a massive star and the subsequent explosion. Thus, all four known forces of nature, are involved in making supernovae a prime example for a “multi-physics problem.” To make progress by quantitative investigations of this highly complex and nonlinear problem towards a deeper understanding of the explosion mechanism, one needs to rely heavily on large-scale computer simulations. It is the goal of this thesis to take a major step forward in the numerical modeling of supernovae to gain an improved understanding of the underlying explosion mechanism.

1.1 The Paradigm of the Delayed Neutrino-driven Explosion Mechanism

Ever since Colgate & White (1966) proposed that neutrinos play an important role in powering the explosion of core-collapse supernovae, the favored scenario for more than 40 years has been the delayed neutrino-heating explosion mechanism. The current state of research into the detailed process of the core-collapse supernova mechanism has been reviewed by Bethe (1990); Janka et al. (2007); Janka (2012); Janka et al. (2012); Burrows (2013). We provide here a brief summary of the basic picture.

All stars create energy by the fusion of lighter elements to heavier ones. In the case of stars with more than about eight times the mass of our sun, they pass through successive stages of nuclear burning of hydrogen, helium, carbon, neon, oxygen, and finally silicon. Since iron possesses the highest binding energy per nucleon, no more energy can be released by further nuclear burning. Thus, such stars develop an onion-shell like structure with a cores consisting of iron-group nuclei. The mass of this core is continuously increasing, since silicon burning still takes place at the surface of the iron core. When the iron core at the center of the massive star reaches the Chandrasekhar mass limit of roughly 1.4 solar masses, the electron degeneracy pressure can no longer stabilize the core. It collapses because the stabilizing pressure of degenerated electrons is reduced by captures on nuclei and photo-dissociation of heavy nuclei. These processes decrease the number of leptons per baryon, the electron fraction Y_e , and thus, result in a further pressure reduction. Consequently, the collapse is accelerated. A huge amount of neutrinos is released, which can initially freely escape from the inner core of

the star. When the central density reaches $\rho \approx 10^{12} \text{ g/cm}^3$, an important development during collapse sets in. At these densities, neutrinos essentially become trapped in the core, as their diffusion time becomes larger than the collapse time. From this point on, the inner core of the star collapses almost adiabatically and homologously, until the central density reaches nuclear saturation density ($2.7 \cdot 10^{14} \text{ g/cm}^3$). The collapse is stopped by the stiffening of the equation of state due to repulsive interactions between nucleons. The rebound of the inner core launches a shock wave into the outer core as it collides with the outer regions of the iron core, which are still falling inwards at supersonic speed. However, it turns out that this formed shock wave is not sufficiently energetic to directly trigger a supernova explosion. It quickly loses energy because of photo-dissociation of heavy nuclei into free nucleons. Once it reaches densities below 10^{11} g/cm^3 , the shock wave is further weakened because rapid deleptonization associated with an energy loss occurs in the region behind the shock front as it becomes transparent to neutrinos. Within a few milliseconds, the post-shock matter stops to move outwards. However, the shock front continues to be pushed to larger radii, since more and more matter is accreted onto the nascent proto-neutron star. Typically, the outward-moving shock finally stalls at a radius between 100 and 200 km and afterwards recedes again. As the matter behind the shock has negative velocities and thus is falling inward, the shock becomes an accretion shock.

Neutrinos streaming off the forming neutron star can revive the stalled shock. Most of the gravitational energy released during the collapse of the inner core of the star is carried away by neutrinos. They deposit a small fraction of their energy in the layers between the young proto-neutron star and the shock surface. Mainly by charged current neutrino ν_e captures on free nucleons the material behind the shock is heated up by the following reaction channels,



and these layers are cooled by the corresponding inverse processes,



Neutrino heating is proportional to r^{-2} , whereas neutrino cooling falls much steeper with a r^{-6} dependency (Janka 2001; Janka et al. 2012). As a consequence, there exists a so-called gain radius, where neutrino heating and cooling balance each other.

By the persistent energy deposition of neutrinos into the region between the gain layer and the shock front, i.e. the gain layer, the pressure behind the supernova shock front is increased. If neutrino heating is strong enough to overcome the ram pressure of the infalling material, the shock can be driven outwards leading to a supernova explosion.

1.2 The Importance of Hydrodynamic Instabilities

The observation of the supernova SN1987 was a major breakthrough in the understanding of the mechanism of core-collapse supernovae. For the first time, it was shown that the ejected

mass distribution was highly anisotropic (Hillebrandt et al. 1989; Arnett et al. 1989; McCray 1993; Nomoto et al. 1994; Müller 1998). This insight can only be explained if hydrodynamic instabilities grow shortly after core bounce (Kifonidis et al. 2003, 2006; Hammer et al. 2010).

Even more importantly, in modeling core-collapse supernovae it turned out that spherically symmetric simulations with a self-consistent treatment of neutrino effects fail to explode for stars above 10 solar masses (Bruenn 1985, 1987; Burrows et al. 1995; Mezzacappa et al. 2001; Rampp & Janka 2000, 2002; Liebendörfer et al. 2001, 2005; Buras et al. 2003b; Thompson et al. 2003) with the notable exception of low-mass progenitors incorporating a O-Ne-Mg core (see the 1D explosion of Kitaura et al. 2006 investigating a $8.8 M_{\odot}$ progenitor of Nomoto 1987).

Thus, nowadays there is a universal consensus in supernova theory that the neutrino-driven explosion mechanism heavily relies on the supporting action of multidimensional effects. Two hydrodynamic instabilities have been identified that play a potentially important role in the accretion flow between the stalled supernova shock and the forming neutron star:

Neutrino heating is strongest near the gain layer, as its strength decreases quickly with increasing distance from the gain radius, and thus, establishes a negative entropy gradient in the gain layer, which is unstable to buoyancy-driven convection as already recognized by Bethe (1990). Neutrino-driven convection manifests itself in the form of high-entropy bubbles, that transport heated material from close to the gain layer to the shock front, pushing the shock front farther out (Dolence et al. 2013). Moreover, cool matter can flow down towards the gain layer to be heated more efficiently. Indeed, the first generation of multi-dimensional simulations confirmed convective activity in the postshock layer (hot-bubble convection) and its supportive effect for a neutrino-driven explosion (Herant et al. 1992; Burrows & Fryxell 1992; Herant et al. 1994; Burrows et al. 1995; Janka & Müller 1996; Müller & Janka 1997).

A distinctly different phenomenon, which plays an important role in the supernova core, was found by Blondin et al. (2003) through purely hydrodynamic simulations of adiabatic accretion flows behind a stalled shock. This so-called “standing-accretion shock instability” (SASI) is demonstrated by large-scale $\ell = 1$ and $\ell = 2$ sloshing motions of the shock front (i.e., the dipole and quadrupole terms of an expansion in spherical harmonics) manifesting in bipolar sloshing of the shock with pulsational strong expansion and contraction. In three dimensions it can also develop $\ell = 1, m = \pm 1$ spiral modes (Blondin & Mezzacappa 2007; Iwakami et al. 2009; Fernández 2010). This instability of the shock itself has been further studied by several follow-up hydrodynamic studies (Blondin & Mezzacappa 2006, 2007; Ohnishi et al. 2006; Scheck et al. 2008; Iwakami et al. 2008, 2009; Fernández & Thompson 2009b; Fernández 2010). While Blondin & Mezzacappa (2006) and Laming (2007) propose a purely acoustic cycle, with the help of a linear stability analysis for the instability, Foglizzo (2002); Foglizzo et al. (2006, 2007); Yamasaki & Yamada (2007) suggested an advective-acoustic cycle for amplifying the characteristic oscillatory growth of the SASI. Guilet & Foglizzo (2012) have recently given strong arguments for the hypothesis of an advective-acoustic cycle by a detailed analysis of the mode frequencies. Furthermore, Foglizzo et al. (2012) have developed a shallow water analogue, the SWASI experiment, in which the water flow between a circular reservoir and a central tube as sink mimics the accretion flow that feeds the nascent neutron star. With the role of the shock and of acoustic waves being played by a hydraulic jump and surface water waves, respectively, similar sloshing and spiral motions are observed as in the hydrodynamic

simulations of collapsing stellar cores.

Violent hydrodynamic mass motions in the postshock layer push the shock farther out and prolong the dwell time of the accreted matter in the heating region. Thus, it is expected that both convection and the SASI increase the volume-integrated energy deposition rate of neutrinos in the gain layer sufficiently to enable a supernova explosion. Indeed, multi-dimensional hydrodynamic simulations proved that neutrino-driven explosion are enabled by nonradial mass motions, while the corresponding spherical symmetric models failed to explode. (Herant et al. 1994; Burrows & Fryxell 1992; Burrows et al. 1995; Janka & Mueller 1995; Janka & Müller 1996; Fryer & Heger 2000; Marek & Janka 2009; Murphy & Burrows 2008; Nordhaus et al. 2010; Hanke et al. 2012; Suwa et al. 2010).

The first multi-dimensional simulations performed with self-consistent energy-dependent neutrino transport on the same level as in the state-of-the art 1D models, could only partially confirm the success of the mentioned studies with a simplified description of neutrino effects (Buras et al. 2006a,b; Marek & Janka 2009). Although the important role of non-radial effects on the development of a successful explosion has been confirmed, a rather small number of progenitors could be evolved into the explosion phase. Fortunately, in the past years the number of successful self-consistent explosion models is growing (Müller et al. 2012b,a; Bruenn et al. 2013; Suwa et al. 2010 and the reviews of Janka 2012; Janka et al. 2012). However, one still has to prove the robustness of the delayed neutrino-driven explosion mechanism for a wide range of progenitor models. Is the support of hydrodynamic instabilities sufficient to enable explosions for arbitrary progenitor structures?

1.3 Advancing to Three-dimensional Modeling

Indeed, the aforementioned 2D studies have underlined the importance of non-radial hydrodynamic mass motions in the postshock layer, such as convection and the SASI for reviving the stalled supernova shock. While these studies have confirmed the concept of the delayed neutrino-driven explosion mechanism, they suffer from the assumption of axisymmetry. Once this artificial symmetry assumption is dropped, the fluid dynamics in the postshock layer will essentially evolve in a different manner in a full 3D setup. The imposition of 2D symmetry incorporates artifacts, such as numerical perturbations along the preferred symmetry axis, which amplifies the growth of hydrodynamic instabilities, and the “inverse turbulent energy cascade” (Kraichnan 1967), which transports turbulent energy from small to large spatial scales in 2D. Fragmentation of the postshock flow and the development of vortex structures is not possible, whereas hydrodynamic structures, such as convective bubbles, are forced to a toroidal structure around the artificial symmetry axis and thus, are inherently larger. As nature is 3D, it is the most urgent goal in core-collapse supernova modeling to advance to fully three-dimensional simulations to gain insight into the effect of the deficiencies of forced symmetry.

As three-dimensional hydrodynamic simulations of core-collapse supernovae are computationally very challenging, the first generation of studies comparing 2D and 3D simulations employed simple, analytical neutrino heating and cooling terms. This approach allows to mimic the principal effect of neutrinos on the hydrodynamic flow, while avoiding the extreme computational load of full neutrino transport (Nordhaus et al. 2010; Hanke et al. 2012;

Burrows et al. 2012; Murphy et al. 2013; Dolence et al. 2013; Couch 2013). Employing the simple neutrino heating and cooling scheme of Murphy & Burrows (2008), the Princeton group claimed that their 3D models explode more easily and readily compared to the 2D cases (Nordhaus et al. 2010; Burrows et al. 2012; Dolence et al. 2013). Contrary, we found that there is little difference in the onset of the explosion in 2D and 3D (Hanke et al. 2012). A further study of Couch (2013) reported a yet different conclusion, claiming that 3D explosions are even harder to obtain.

In the light of the diverging results of the simplified 3D studies with a neutrino heating and cooling scheme, full three-dimensional neutrino-radiation hydrodynamic simulations are urgently needed to clarify the role of 3D effects for the neutrino-driven mechanism, although such simulations are far more challenging than the ones reported so far reported. The mentioned studies neglected neutrino losses from the neutron star interior such that the neutron star was not able to shrink below ~ 60 km. Compared to simulations with full neutrino transport (e.g. Marek & Janka 2009; Müller et al. 2012b,a), the shock radius remained rather large and the time matter can stay in the gain layer was long. Under such conditions, the development of the SASI is suppressed (Scheck et al. 2008), while the growth of neutrino-driven convection is supported (Foglizzo et al. 2006). As 3D models with higher sophistication of neutrino transport might meet the conditions for SASI growth, further refinement of the sophistication in 3D models is necessary to clarify the role of the different hydrodynamic instabilities in the supernova core for the explosion mechanism.

1.4 Organization of this Thesis

As the available high-performance computing resources have increased sufficiently, the goal of this project is to perform the very first 3D simulations of core-collapse supernova explosions with fully self-consistent neutrino transport on the level of the most sophisticated axisymmetric simulations (Buras et al. 2006a,b; Marek & Janka 2009; Müller et al. 2012b,a). In doing so, we take a major step forward in our understanding of the true nature of the neutrino-driven explosion mechanism.

Furthermore, we have performed a large set of fully self-consistent simulations in axisymmetry. So far, successful explosion models were restricted to some selected progenitors. By investigating a great number of stellar progenitors in multi dimensions we prove the viability of the neutrino-driven mechanism for several progenitor structures. For example, Müller et al. (2012a) pointed out the dependence of the growth condition of the SASI on the details of the conditions in the supernova core. Moreover, our investigations are motivated by recent systematic studies of the connection between progenitors and remnants (O'Connor & Ott 2011) as well as the properties (Uglio et al. 2012) of core-collapse supernovae. Mainly with the help of the latter study, we can identify promising candidates for an explosion, which are worth investigating in a fully self-consistent setup. The exploration of the parameter space of progenitor models in 2D helps us to identify promising candidates for an explosion to be simulated in 3D.

In this thesis, we present the performed multi-dimensional neutrino radiation-hydrodynamics simulations in the following manner: In Chapter 2, we introduce the VERTEX-PROMETHEUS

code and the underlying equations of neutrino radiation-hydrodynamics. Within a brief report about the employed numerical methods, we generalize the 2D program of Buras et al. (2006a) to a full 3D code. Our set of axisymmetric simulations performed with the VERTEX-PROMETHEUS code is presented in Chapter 3, where we study the dependence of the neutrino-driven explosion mechanism on the progenitor structure. We complete the analysis of our multi-dimensional simulations in Chapter 4 by studying the influence of the numerical setup. The main topic of this thesis, the first self-consistent multi-dimensional simulations of core-collapse supernova explosions without any symmetry restrictions, is discussed in Chapters 5 and 6. Presenting 3D simulations of a $27 M_{\odot}$ progenitor model of Woosley et al. (2002) and a $20 M_{\odot}$ star based on the presupernova models of Woosley & Heger (2007), we focus in Chapter 5 on the growth of hydrodynamic instabilities, the SASI and convection, in a 3D setup. For the first time, we report about unambiguously identified SASI activity in a 3D simulation with detailed neutrino transport (see Hanke et al. 2013 for the discussion of the $27 M_{\odot}$ progenitor case). As our 3D models fail to explode opposite to the corresponding 2D cases, we identify possible reasons for the negative outcome of the 3D simulations along the arguments of Hanke et al. (2012) as well as Dolence et al. (2013) and Couch (2013). A purely convective 3D model based on the $11 M_{\odot}$ progenitor model of Woosley et al. (2002), is discussed in Chapter 6. Chapter 7 contains a summary of our work.

2 The Vertex-Prometheus Neutrino Radiation Hydrodynamics Code

To investigate the physical driving mechanism that is responsible for the supernova explosion, we apply the numerical code VERTEX-PROMETHEUS throughout this thesis. This tool was specifically developed to perform simulations of core-collapse supernova explosions of massive stars. VERTEX-PROMETHEUS was originally developed by Rampp & Janka (2002) for tackling the problem of neutrino transport in spherical symmetry (1D). The code was extended to a two-dimensional (2D) version by Buras et al. (2006a). In this thesis we present the three-dimensional (3D) version without symmetry restrictions.

Since the 1D and 2D version of the VERTEX-PROMETHEUS code have already been described extensively in the literature, this chapter puts a stronger emphasis on the governing equations underlying the multidimensional problem and their basic numerical implementation, instead of an in-depth documentation of the full code. Nevertheless, we will shortly elaborate on the implementation of the additional terms necessary for the 3D version.

The inner core of a massive star consists of matter that can be treated as an ideal fluid (Müller 1998), for which viscosity and heat conduction can be neglected, although including neutrino transport re-introduces some of these non-ideal effects self-consistently. Therefore, the equations of hydrodynamics, supplemented by advection equations for the chemical composition of the fluid, can be applied to follow the time evolution of the stellar plasma. However, neutrinos have to be treated completely different from the stellar plasma, namely as radiation, since the mean free path of neutrinos between interactions becomes comparable to or even larger than the dimensions of the system in the supernova problem. The concept of hydrodynamics is then no longer valid and neutrinos have to be treated as a radiation field described by a distribution function that evolves according to kinetic theory. Thus, the propagation of neutrinos and their interaction with the stellar medium has to be treated by solving the Boltzmann equation separately. For this reason, our algorithm employs an operator splitting approach to couple the two sets of evolution equations; i.e., for each cycle of the code the hydrodynamic part and the neutrino radiation transport part are solved subsequently in two independent steps.

When we present both parts of the code in the following, we formulate the underlying equations in spherical coordinates with radius r , latitudinal angle θ , and azimuthal angle ϕ . Spherical coordinates are well suited for exploiting the approximate symmetry of the stellar core and to ensure that the investigated part of the star is well resolved.

2.1 The Hydrodynamics Part: The Prometheus Code

In the hydrodynamics part, the stellar matter is described by the Eulerian, non-relativistic equations of hydrodynamics for an ideal, inviscid fluid. These conservation laws for mass, momentum, and energy read in spherical coordinates (r, θ, ϕ) as follows:

- Mass conservation:

$$\frac{\partial \rho}{\partial t} + \frac{1}{r^2} \frac{\partial}{\partial r} (r^2 \rho v_r) + \frac{1}{r \sin \theta} \frac{\partial}{\partial \theta} (\rho \sin \theta v_\theta) + \frac{1}{r \sin \theta} \frac{\partial}{\partial \phi} (\rho v_\phi) = 0. \quad (2.1)$$

- Momentum conservation:

$$\begin{aligned} \frac{\partial \rho v_r}{\partial t} + \frac{1}{r^2} \frac{\partial}{\partial r} (r^2 \rho v_r^2) + \frac{1}{r \sin \theta} \frac{\partial}{\partial \theta} (\rho \sin \theta v_\theta v_r) + \frac{1}{r \sin \theta} \frac{\partial}{\partial \phi} (\rho v_\phi v_r) \\ + \left\{ \rho \frac{-v_\theta^2 - v_\phi^2}{r} \right\} + \frac{\partial P}{\partial r} = -\rho \frac{\partial \Phi}{\partial r} + Q_{M,r}, \end{aligned} \quad (2.2)$$

$$\begin{aligned} \frac{\partial \rho v_\theta}{\partial t} + \frac{1}{r^2} \frac{\partial}{\partial r} (r^2 \rho v_r v_\theta) + \frac{1}{r \sin \theta} \frac{\partial}{\partial \theta} (\rho \sin \theta v_\theta^2) + \frac{1}{r \sin \theta} \frac{\partial}{\partial \phi} (\rho v_\phi v_\theta) \\ + \left\{ \rho \frac{v_r v_\theta - v_\phi^2 \cot \theta}{r} \right\} + \frac{1}{r} \frac{\partial P}{\partial \theta} = - \left[\rho \frac{\partial \Phi}{\partial \theta} \right] + Q_{M,\vartheta}, \end{aligned} \quad (2.3)$$

$$\begin{aligned} \frac{\partial \rho v_\phi}{\partial t} + \frac{1}{r^2} \frac{\partial}{\partial r} (r^2 \rho v_r v_\phi) + \frac{1}{r \sin \theta} \frac{\partial}{\partial \theta} (\rho \sin \theta v_\theta v_\phi) + \frac{1}{r \sin \theta} \frac{\partial}{\partial \phi} (\rho v_\phi^2) \\ + \left\{ \rho \frac{v_r v_\phi + v_\theta v_\phi \cot \theta}{r} \right\} + \frac{1}{r \sin \theta} \frac{\partial P}{\partial \phi} = +Q_{M,\phi}. \end{aligned} \quad (2.4)$$

- Energy conservation:

$$\begin{aligned} \frac{\partial e}{\partial t} + \frac{1}{r^2} \frac{\partial}{\partial r} [r^2 (e + P) v_r] + \frac{1}{r \sin \theta} \frac{\partial}{\partial \theta} [(e + P) \sin \theta v_\theta] + \frac{1}{r \sin \theta} \frac{\partial}{\partial \phi} [(e + P) v_\phi] \\ = -\rho v_r \frac{\partial \Phi}{\partial r} - \left[\rho \frac{v_\theta}{r} \frac{\partial \Phi}{\partial \theta} \right] \\ + Q_E + v_r Q_{M,r} + v_\theta Q_{M,\vartheta} + v_\phi Q_{M,\phi}. \end{aligned} \quad (2.5)$$

Here, ρ denotes the mass density, v_r , v_θ , and v_ϕ the radial, lateral, and azimuthal components of the velocity, P the pressure, $e = \rho[\varepsilon + (v_r^2 + v_\theta^2 + v_\phi^2)/2]$ the specific total energy (with ε the specific internal energy), and Φ the gravitational potential of the fluid. The term $\frac{\partial \Phi}{\partial \phi}$ does not appear in the equations above and terms containing $\frac{\partial \Phi}{\partial \theta}$ are marked with squared brackets, because in all 3D runs and their corresponding 2D runs only the monopole approximation of the Poisson equation is applied to treat self-gravity (see Section 2.1.2). The neutrino source terms for momentum and energy transfer are labelled by $Q_{M,r}$, $Q_{M,\vartheta}$, $Q_{M,\phi}$, and Q_E , respectively.

Note that the terms in curly brackets are fictitious forces. They appear because the directions of the base unit vectors in spherical polar coordinates vary in space in general curvilinear coordinates such as the spherical coordinates applied here.

The set of equations (2.1–2.5) has to be closed by an equation of state (EoS) which relates the gas pressure P to the density ρ , and to the internal energy ε . Since in general the equation of state also requires the chemical composition for determining the gas pressure P , one has to solve additional conservation laws for the mass fractions X_i of individual nuclear species i to follow the time evolution of the composition:

$$\frac{\partial(\rho X_i)}{\partial t} + \frac{1}{r^2} \frac{\partial}{\partial r} [r^2 (\rho X_i) v_r] + \frac{1}{r \sin \theta} \frac{\partial}{\partial \theta} [(\rho X_i) \sin \theta v_\theta] + \frac{1}{r \sin \theta} \frac{\partial}{\partial \phi} [(\rho X_i) v_\phi] = R_i. \quad (2.6)$$

Here, R_i is the source term for an individual nucleus, which expresses the rate of composition changes by nuclear reactions for species i . In case the medium reaches nuclear statistical equilibrium (NSE), the chemical composition is determined via the equation of state by the gas density, the temperature, and one additional quantity, the electron fraction Y_e . It is also needed in the non-NSE regime for computing the contributions of electrons and positrons in the equation of state. Thus one additional conservation law for Y_e has to be solved as follows:

$$\frac{\partial(\rho Y_e)}{\partial t} + \frac{1}{r^2} \frac{\partial}{\partial r} [r^2 (\rho Y_e) v_r] + \frac{1}{r \sin \theta} \frac{\partial}{\partial \theta} [(\rho Y_e) \sin \theta v_\theta] + \frac{1}{r \sin \theta} \frac{\partial}{\partial \phi} [(\rho Y_e) v_\phi] = Q_N. \quad (2.7)$$

The source term Q_N represents the rate of change of the net electron number density and is caused by emission and absorption of electron flavor neutrinos. Yet, even in case of NSE, the equations (2.6) have to be solved for each individual species to be able to follow temporal compositional changes, which are caused by mixing processes that lead to changes in the internal energy.

2.1.1 Numerical Solution

In the hydrodynamics part of the code, we employ the Newtonian finite-volume code PROMETHEUS (Fryxell et al. 1989, 2000) as a hydrodynamics solver to numerically integrate the equations (2.1–2.7). It is a direct implementation of the “Piecewise Parabolic Method” (PPM) of Colella & Woodward (1984), which is a time-explicit, third-order in space, second-order in time conservative Godunov-type scheme (Godunov 1959) that employs an exact Riemann-solver (Colella & Glaz 1985). PROMETHEUS is particularly well suited for following discontinuities in the fluid flow like shocks, contact discontinuities, or boundaries between layers of different chemical composition. Its capability of solving multi-dimensional problems with high computational efficiency and numerical accuracy is of great advantage in performing the simulations presented in this thesis. PROMETHEUS was improved and supplemented by additional problem specific features to be applicable to core-collapse supernova simulations by Keil (1997) and Kifonidis et al. (2003). It makes use of the “Consistent Multifluid Advection” (CMA) method of Plewa & Müller (1999) for ensuring an accurate advection of different chemical components of the fluid. In the vicinity of strong shocks the hydrodynamics solver is switched to the HLLE solver of Einfeldt (1988) to avoid spurious oscillations. This so-called “odd-even

decoupling” occurs if such shocks are aligned with one of the coordinate axis of the grid employed in multi-dimensional simulations (Quirk 1994; Kifonidis et al. 2003).

The hydrodynamics solver PROMETHEUS integrates only the left-hand sides of equations (2.1–2.7). All terms which appear on the right-hand sides are computed separately in operator split steps. Firstly, the source terms R_i responsible for changes of the composition depend on nuclear burning, nuclear dissociation, and recombination of the chemical elements, which is taken into account in an approximative fashion according to Appendix B.2 of Rampf & Janka (2002). The neutrino source terms of momentum and energy transfer Q_{M_r} , Q_{M_ϑ} , Q_{M_ϕ} , and Q_E are calculated by solving the equations of neutrino transport, which will be described in the following section.

2.1.2 Treatment of Self-Gravity

Although PROMETHEUS is essentially a Newtonian code, some effects of general relativity are taken into account approximately in the calculation of the gravitational potential Φ . In spherical symmetry, the gravitational potential $\Phi = \Phi_{1D}^{GR}$ includes general relativistic effects such as contributions of the pressure and energy of the stellar medium and neutrinos as described in detail in Marek et al. (2006). In the 3D simulations presented in this thesis and the corresponding 2D runs we use only the spherically symmetric potential Φ_{1D}^{GR} (i.e. the monopole term) computed from angular averages of the evolved variables. In all further 2D simulations a multi-dimensional gravitational potential is applied with the effects of general relativity taken into account as described in Buras et al. (2006a). The gravitational potential can be written symbolically as $\Phi_{2D} = \Phi_{2D}^{\text{Newt}} + (\Phi_{1D}^{GR} - \Phi_{1D}^{\text{Newt}})$. As described in Müller & Steinmetz (1995), the Newtonian gravitational potential Φ_{2D}^{Newt} for a 2D axisymmetric mass distribution is evaluated by expanding the integral solution of the Poisson equation into a Legendre series. General relativistic effects are incorporated approximately by the correction term $\Phi_{1D}^{GR} - \Phi_{1D}^{\text{Newt}}$, where Φ_{1D}^{Newt} is the Newtonian counterpart of the spherical symmetric effective general relativistic potential. This procedure ensures very good consistency with full general relativistic simulations of core-collapse supernovae in one-dimensional (Liebendörfer et al. 2005) and in 2D simulations (Müller et al. 2012b).

2.1.3 Equation of State

The equations of hydrodynamics have to be closed by an appropriate equation of state, which must be suitable for the extreme physical conditions in the supernova core. During the collapse of the core of a massive star, the nuclear saturation density $\rho_0 \approx 2.7 \cdot 10^{14} \text{ g/cm}^3$ and temperatures of about the 10 MeV and more are reached. Since for example the density decreases by several decades from the innermost part of the core to the outer burning shells, different equations of state have to be applied to cover the whole density range.

To accommodate the whole density range, the equation of state is divided into a “high density” and a “low density” part. In this thesis, the tabulated nuclear equation of state of Lattimer & Swesty (1991) with a nuclear incompressibility of 220 MeV and a symmetry energy parameter of 29.3 MeV is applied in the “high density” regime. This nuclear equation of

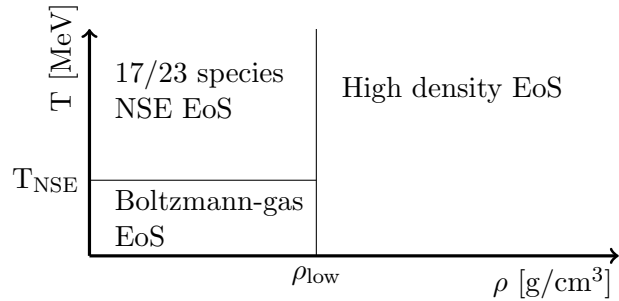


Figure 2.1: Sketch of the different equations of state applied in the simulations in the density-temperature plane. Above a threshold value ρ_{low} the high-density EoS is applied. The low-density regime is divided in two parts: above a temperature of 0.5 MeV NSE is assumed, and below that value matter is treated as a Boltzmann gas taking into account nuclear burning.

state is chosen for all simulations in this thesis, because it best matches current constraints of nuclear theory and astrophysical observations (see Hempel et al. 2012; Hebeler et al. 2010; Steiner et al. 2010) compared to other commonly used equations of state. On the one hand measurements give a value of 240 MeV for the bulk incompressibility modulus of symmetric nuclear matter (Shlomo et al. 2006), and on the other hand the employed EoS is compatible with a recently observed neutron star mass of two solar masses (Demorest et al. 2010). The nuclear equation of state of Lattimer & Swesty (1991) is based on the compressible liquid drop model of Lattimer et al. (1985), which describes the transition from inhomogeneous to homogeneous matter using a Maxwell construction. In this EoS the nucleon-nucleon interactions is expressed through a Skyrme-like potential and the nuclear statistical equilibrium NSE is assumed above a temperature of 0.5 MeV. It describes the baryonic part of inhomogeneous matter as a mixture of free protons, neutrons, α -particles, and one representative heavy nucleus, whereas the homogeneous supernuclear phase consists only of interacting protons and neutrons.

Below a threshold density ρ_{low} , the EoS described above is extended by an equation of state that considers electrons, positrons, photons, free protons and neutrons, α -particles, and up to 20 nuclear species in thermodynamic equilibrium. In this thesis, during the collapse phase, this threshold density ρ_{low} is set to $3 \cdot 10^8$ g/cm³ and changed to $1 \cdot 10^{11}$ g/cm³ at bounce. The applied low-density equation of state of Janka (1999) as implemented by Rampp & Janka (2002) treats the nuclei as classical Boltzmann gases, and electrons and positrons as Fermi gases with arbitrary degeneracy. Above a temperature of $T = 0.5$ MeV nuclear statistical equilibrium is assumed and the equation of state is replaced by a full NSE composition table as describe in Buras et al. (2006a).

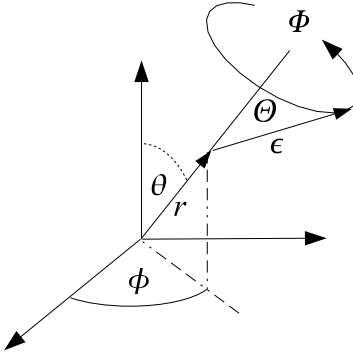


Figure 2.2: Illustration of the phase space coordinates (see the main text).

2.2 The Neutrino Radiation Part: the Vertex Code

2.2.1 Overview

The neutrino source terms for the energy, momentum, and electron fraction entering the hydrodynamic equations (2.1–2.5) are determined by the solution of the equations of neutrino transport in the VERTEX code. In order to describe neutrinos as a radiation field, the specific neutrino intensity \mathcal{I} is introduced, which is defined such that

$$\delta\mathcal{E} = \mathcal{I}(\mathbf{x}, \mathbf{n}, \epsilon, t) dA \cos \vartheta d\Omega d\epsilon dt \quad (2.8)$$

is the amount of neutrino radiation energy in the neutrino energy interval $(\epsilon, \epsilon + d\epsilon)$ streaming through a surface dA inclined with the angle ϑ relative to its direction of propagation $\mathbf{n}(\Theta, \Phi)$ during the time interval dt . The specific neutrino intensity is related to the neutrino distribution function $f(r, \vartheta, \phi, \epsilon, \Theta, \Phi, t)$ in phase space by

$$\mathcal{I} = \frac{\epsilon^3}{h^3 c^2} f. \quad (2.9)$$

The time evolution of the specific neutrino intensity \mathcal{I} is determined by the transfer equation of radiation transport, while the Boltzmann equation of statistical physics describes the evolution of the neutrino distribution function itself,

$$\left(\frac{1}{c} \frac{\partial}{\partial t} + \frac{\partial}{\partial s} \right) \mathcal{I} = \eta - \chi \mathcal{I}. \quad (2.10)$$

The transport equation describes the temporal changes of the radiation energy streaming through a fluid element of length ds caused by emission and absorption of neutrinos with the stellar fluid. These processes are expressed by the collision term on the right hand side $\eta - \chi \mathcal{I}$ with the emissivity η and the opacity χ . Since the collision term itself depends on the specific intensity, the Boltzmann equation has an integro-differential character. As depicted in Fig. 2.2, the time-dependent neutrino intensity, is defined in a six-dimensional phase space, since it describes in every point in real space (r, ϑ, ϕ) the propagation of neutrinos with energy ϵ into the direction $\mathbf{n} = \mathbf{n}(\Theta, \Phi)$ at time t .

Although there are now first efforts at a direct discretization of the full six-dimensional problem by a so-called S_N scheme (Kotake et al. 2012; Sumiyoshi & Yamada 2012), in practice the dimensionality of the problem has to be reduced to avoid the still unacceptable computational costs of full multi-dimensional transport.

For reasons of numerical efficiency, we solve the equations for the two moments of the neutrino intensity with a variable Eddington factor (see Section 2.2.3) instead of tackling the Boltzmann equation directly, which is a very accurate approach, since the neutrino source terms entering the hydrodynamic equations (2.1–2.5) just depend on integrals of \mathcal{I} over momentum space. Hereby, the 0th to 3rd order moments are defined as

$$\mathbf{J}, \mathbf{H}, \mathbf{K}, \mathbf{L}, \dots (r, \vartheta, \phi, \epsilon, t) = \frac{1}{4\pi} \int \mathcal{I}(r, \vartheta, \phi, \epsilon, \Theta, \Phi, t) \mathbf{n}^{0,1,2,3,\dots} d\Omega \quad (2.11)$$

where $d\Omega = \sin \Theta d\Theta d\Phi$, $\mathbf{n} = (\cos \Theta, \sin \Theta \cos \Phi, \sin \Theta \sin \Phi)$, and exponentiation represents repeated application of the dyadic product. If the variable Eddington factors are exact, this approach is equivalent to an exact solution of the Boltzmann equation.

2.2.2 The System of Equations

The multi-dimensional version of the VERTEX transport code employs the so-called “ray-by-ray-plus” approach to reduce the size of the problem even further. In this approach, one assumes that \mathcal{I} is independent of Φ , which amounts to the assumption that the lateral and azimuthal fluxes are zero and that the pressure tensor is diagonal. Then each of the angular momentums of the specific neutrino intensity is expressed by a scalar just depending on three spatial dimensions, and one dimension in momentum space: $J, H, K, L = J, H, K, L(r, \vartheta, \phi, \epsilon, t)$. Although not all terms with lateral or azimuthal gradients or components vanish, the neutrino moments equations are reduced to a spherically symmetric version of the moment equations at different angular coordinates ϑ and ϕ . Therefore, the moment equations almost decouple from each other, and for a fixed angle along a “radial ray” the moment equations can be solved independently as $N_\theta \times N_\phi$ identical spherically symmetric problems with $N_\theta \times N_\phi$ being the number of grid zones in angular direction. As pointed out by Buras et al. (2006a) the additional non-vanishing terms in our approximation associated to the lateral advection of neutrinos in the optical thick regime and the nonradial neutrino pressure gradients cannot be neglected if unphysical convective activity in the proto-neutron star is to be avoided. These terms yield the “ray-by-ray-plus scheme”, in which the evolution of the neutrino energy and flux is governed by the following transport equations in Newtonian $\mathcal{O}(v/c)$ approximation as

shown in (Buras et al. 2006a, Appendix B):

$$\begin{aligned}
& \left(\frac{1}{c} \frac{\partial}{\partial t} + \beta_r \frac{\partial}{\partial r} + \frac{\beta_\vartheta}{r} \frac{\partial}{\partial \vartheta} + \frac{\beta_\phi}{r \sin \vartheta} \frac{\partial}{\partial \phi} \right) J \\
& + J \left(\frac{1}{r^2} \frac{\partial(r^2 \beta_r)}{\partial r} + \frac{1}{r \sin \vartheta} \frac{\partial(\sin \vartheta \beta_\vartheta)}{\partial \vartheta} + \frac{1}{r \sin \vartheta} \frac{\partial \beta_\phi}{\partial \phi} \right) \\
& + \frac{1}{r^2} \frac{\partial(r^2 H)}{\partial r} + \frac{\beta_r}{c} \frac{\partial H}{\partial t} - \frac{\partial}{\partial \epsilon} \left\{ \frac{\epsilon}{c} \frac{\partial \beta_r}{\partial t} H \right\} \\
& - \frac{\partial}{\partial \epsilon} \left\{ \epsilon J \left(\frac{\beta_r}{r} + \frac{1}{2r \sin \vartheta} \frac{\partial(\sin \vartheta \beta_\vartheta)}{\partial \vartheta} + \frac{1}{2r \sin \vartheta} \frac{\partial \beta_\phi}{\partial \phi} \right) \right\} \\
& - \frac{\partial}{\partial \epsilon} \left\{ \epsilon K \left(\frac{\partial \beta_r}{\partial r} - \frac{\beta_r}{r} - \frac{1}{2r \sin \vartheta} \frac{\partial(\sin \vartheta \beta_\vartheta)}{\partial \vartheta} - \frac{1}{2r \sin \vartheta} \frac{\partial \beta_\phi}{\partial \phi} \right) \right\} \\
& + J \left(\frac{\beta_r}{r} + \frac{1}{2r \sin \vartheta} \frac{\partial(\sin \vartheta \beta_\vartheta)}{\partial \vartheta} + \frac{1}{2r \sin \vartheta} \frac{\partial \beta_\phi}{\partial \phi} \right) \\
& + K \left(\frac{\partial \beta_r}{\partial r} - \frac{\beta_r}{r} - \frac{1}{2r \sin \vartheta} \frac{\partial(\sin \vartheta \beta_\vartheta)}{\partial \vartheta} - \frac{1}{2r \sin \vartheta} \frac{\partial \beta_\phi}{\partial \phi} \right) \\
& + \frac{2}{c} \frac{\partial \beta_r}{\partial t} H = C^{(0)}, \quad (2.12)
\end{aligned}$$

$$\begin{aligned}
& \left(\frac{1}{c} \frac{\partial}{\partial t} + \beta_r \frac{\partial}{\partial r} + \frac{\beta_\vartheta}{r} \frac{\partial}{\partial \vartheta} + \frac{\beta_\phi}{r \sin \vartheta} \frac{\partial}{\partial \phi} \right) H \\
& + H \left(\frac{1}{r^2} \frac{\partial(r^2 \beta_r)}{\partial r} + \frac{1}{r \sin \vartheta} \frac{\partial(\sin \vartheta \beta_\vartheta)}{\partial \vartheta} + \frac{1}{r \sin \vartheta} \frac{\partial \beta_\phi}{\partial \phi} \right) \\
& + \frac{\partial K}{\partial r} + \frac{3K - J}{r} + H \left(\frac{\partial \beta_r}{\partial r} \right) + \frac{\beta_r}{c} \frac{\partial K}{\partial t} - \frac{\partial}{\partial \epsilon} \left\{ \frac{\epsilon}{c} \frac{\partial \beta_r}{\partial t} K \right\} \\
& - \frac{\partial}{\partial \epsilon} \left\{ \epsilon L \left(\frac{\partial \beta_r}{\partial r} - \frac{\beta_r}{r} - \frac{1}{2r \sin \vartheta} \frac{\partial(\sin \vartheta \beta_\vartheta)}{\partial \vartheta} - \frac{1}{2r \sin \vartheta} \frac{\partial \beta_\phi}{\partial \phi} \right) \right\} \\
& - \frac{\partial}{\partial \epsilon} \left\{ \epsilon H \left(\frac{\beta_r}{r} + \frac{1}{2r \sin \vartheta} \frac{\partial(\sin \vartheta \beta_\vartheta)}{\partial \vartheta} + \frac{1}{2r \sin \vartheta} \frac{\partial \beta_\phi}{\partial \phi} \right) \right\} \\
& + \frac{1}{c} \frac{\partial \beta_r}{\partial t} (J + K) = C^{(1)}. \quad (2.13)
\end{aligned}$$

Here $\beta_r = v_r/c$, $\beta_\vartheta = v_\vartheta/c$, and $\beta_\phi = v_\phi/c$, where v_r , v_ϑ , and v_ϕ are the components of the hydrodynamic velocity, and c is the speed of light. The functional dependencies $\beta_r = \beta_r(r, \vartheta, \phi, t)$, $J = J(r, \vartheta, \phi, \epsilon, t)$, etc. are suppressed in the notation. In these transport equations for the neutrino energy and flux the quantities $C^{(0)}$ and $C^{(1)}$ denote the zeroth and first moment of the collision term in the Boltzmann equation.

The system of equations (2.12–2.13) is closed by imposing two additional relations to express the higher moments K and L by $K = f_K \cdot J$ and $L = f_L \cdot J$, where f_K and f_L are variable Eddington factors computed from the formal solution of a model Boltzmann equation as described in Rampp & Janka (2002) (see below). The additional terms of the multi-dimensional code version which do not appear in the $\mathcal{O}(v/c)$ equations in spherical symmetry are set in boldface.

2.2.3 Method of Solution

In order to numerically integrate equations (2.12–2.13), three operator-split steps are carried out corresponding to a lateral, azimuthal, and a radial sweep. For this reason, the computational domain $[0, r_{\max}] \times [\vartheta_{\min}, \vartheta_{\max}] \times [\phi_{\min}, \phi_{\max}]$ is covered by N_r radial, N_ϑ latitudinal, and N_ϕ longitudinal zones, where $\vartheta_{\min} = 0$ and $\vartheta_{\max} = \pi$ correspond to the north and south polar axis of the spherical grid, and setting $\phi_{\min} = 0$ and $\phi_{\max} = 2\pi$ covers the full sphere.

In the first two steps the lateral and azimuthal advection of the neutrino with the stellar fluid is tackled treating the boldface terms in the first lines of Eqs. (2.12–2.13) and thus coupling the angular moments of the neutrino distribution of neighboring angular zones. For this purpose, the following two advection equations are considered one after the other.

$$\frac{1}{c} \frac{\partial \Xi}{\partial t} + \frac{1}{r \sin \vartheta} \frac{\partial (\sin \vartheta \beta_\vartheta \Xi)}{\partial \vartheta} = 0, \quad (2.14)$$

$$\frac{1}{c} \frac{\partial \Xi}{\partial t} + \frac{1}{r \sin \vartheta} \frac{\partial (\beta_\phi \Xi)}{\partial \phi} = 0, \quad (2.15)$$

where Ξ represents one of the moments J or H . Although the additional indices of Ξ are suppressed for clarity in Eqs. (2.14–2.15), both advection equations have to be solved for each radius, each energy bin, and for each type of neutrinos.

After integrating over the volume of a zone $(i + \frac{1}{2}, k + \frac{1}{2}, l + \frac{1}{2})$, where i , k , and l are the indices of the radial, lateral, and azimuthal zones, the finite-volume discretization of the equation for lateral advection (2.15) reads

$$\begin{aligned} & \frac{\Xi_{i+\frac{1}{2}, k+\frac{1}{2}, l+\frac{1}{2}}^{n+1} - \Xi_{i+\frac{1}{2}, k+\frac{1}{2}, l+\frac{1}{2}}^n}{ct^{n+1} - ct^n} \\ & + \frac{1}{\Delta V_{i+\frac{1}{2}, k+\frac{1}{2}, l+\frac{1}{2}}} \left(\Delta A_{i+\frac{1}{2}, k+1, l+\frac{1}{2}} \beta_{\vartheta i+\frac{1}{2}, k+1, l+\frac{1}{2}} \Xi_{i+\frac{1}{2}, \kappa_{i+1/2, l+1/2}(k+1), l+\frac{1}{2}}^n \right. \\ & \quad \left. - \Delta A_{i+\frac{1}{2}, k, l+\frac{1}{2}} \beta_{\vartheta i+\frac{1}{2}, k, l+\frac{1}{2}} \Xi_{i+\frac{1}{2}, \kappa_{i+1/2, l+1/2}(k), l+\frac{1}{2}}^n \right) \\ & = 0, \end{aligned} \quad (2.16)$$

with the volume element $\Delta V_{i+\frac{1}{2}, k+\frac{1}{2}, l+\frac{1}{2}} = \frac{2\pi}{3} (r_{i+1}^3 - r_i^3) (\cos \vartheta_k - \cos \vartheta_{k+1})$ and the surface element $\Delta A_{i+\frac{1}{2}, k, l+\frac{1}{2}} = \pi (r_{i+1}^2 - r_i^2) \sin \vartheta_k$. To guarantee monotonicity, upwind values of the moments $\Xi_{i+\frac{1}{2}, \kappa_{i+1/2, l+1/2}(k), l+\frac{1}{2}}^n$, with

$$\kappa_{i+1/2, l+1/2}(k) \equiv \begin{cases} k - \frac{1}{2} & \text{for } \beta_{\vartheta i+\frac{1}{2}, k, l+\frac{1}{2}} > 0, \\ k + \frac{1}{2} & \text{else,} \end{cases} \quad (2.17)$$

are used for computing the lateral fluxes across the interfaces of the angular zones. The time-step is restricted by the Courant-Friedrichs-Lowy (CFL) condition:

$$\Delta t_{\vartheta, \text{CFL}} = \min_{i, k, l} \frac{\Delta x_{\vartheta; i+\frac{1}{2}, k+\frac{1}{2}, l+\frac{1}{2}}}{|v_{\vartheta; i+\frac{1}{2}, k+\frac{1}{2}, l+\frac{1}{2}}|} = \min_{i, k, l} \frac{r_{i+\frac{1}{2}} (\vartheta_{k+1} - \vartheta_k)}{|v_{\vartheta; i+\frac{1}{2}, k+\frac{1}{2}, l+\frac{1}{2}}|}, \quad (2.18)$$

where Δx_ϑ is the zone width in lateral direction.

The finite-differenced version of the equation for azimuthal advection (2.15) reads again after integrating over the volume of a zone,

$$\begin{aligned} & \frac{\Xi_{i+\frac{1}{2},k+\frac{1}{2},l+\frac{1}{2}}^{n+1} - \Xi_{i+\frac{1}{2},k+\frac{1}{2},l+\frac{1}{2}}^n}{ct^{n+1} - ct^n} \\ & + \frac{1}{\Delta V_{i+\frac{1}{2},k+\frac{1}{2},l+\frac{1}{2}}} \left(\Delta A_{i+\frac{1}{2},k+\frac{1}{2},l+1} \beta_{\phi i+\frac{1}{2},k+\frac{1}{2},l+1} \Xi_{i+\frac{1}{2},k+\frac{1}{2},\lambda_{i+1/2,k+1/2}(l+1)}^n \right. \\ & \quad \left. - \Delta A_{i+\frac{1}{2},k+\frac{1}{2},l} \beta_{\phi i+\frac{1}{2},k+\frac{1}{2},l} \Xi_{i+\frac{1}{2},k+\frac{1}{2},\lambda_{i+1/2,k+1/2}(l)}^n \right) \\ & = 0, \end{aligned} \quad (2.19)$$

with the volume element $\Delta V_{i+\frac{1}{2},k+\frac{1}{2},l+\frac{1}{2}} = \frac{1}{3} (r_{i+1}^3 - r_i^3) (\cos \vartheta_k - \cos \vartheta_{k+1}) (\phi_{l+1} - \phi_l)$ and the surface element $\Delta A_{i+\frac{1}{2},k+\frac{1}{2},l} = (r_{i+1}^2 - r_i^2)(\vartheta_{k+1} - \vartheta_k)/2$. Similar to the lateral step, the integration procedure employs upwind values of the moments $\Xi_{i+\frac{1}{2},k+\frac{1}{2},\lambda_{i+1/2,k+1/2}(l)}^n$, with

$$\lambda_{i+1/2,k+1/2}(k) \equiv \begin{cases} l - \frac{1}{2} & \text{for } \beta_{\phi i+\frac{1}{2},k+\frac{1}{2},l} > 0 \\ l + \frac{1}{2} & \text{else} \end{cases} \quad (2.20)$$

and the time-step is limited by:

$$\Delta t_{\phi,\text{CFL}} = \min_{i,k,l} \frac{\Delta x_{\phi;i+\frac{1}{2},k+\frac{1}{2},l+\frac{1}{2}}}{|v_{\phi;i+\frac{1}{2},k+\frac{1}{2},l+\frac{1}{2}}|} = \min_{i,k,l} \frac{r_{i+\frac{1}{2}} \sin \vartheta_k (\phi_{l+1} - \phi_l)}{|v_{\vartheta;i+\frac{1}{2},k+\frac{1}{2},l+\frac{1}{2}}|}. \quad (2.21)$$

One can estimate that for typical zone widths and velocities in the convective region of the neutron star at least for axisymmetric simulations the time-step limitation is not restrictive. It is always limited by other constraints. However, due to the small zone widths at the polar axis in three-dimensional setups, the time step constraints of the azimuthal step $t_{\phi,\text{CFL}}$ can become similar to the constraints given by the radial discretization of the moment equations.

In the third and computationally most intensive step all remaining terms of Eqs. (2.12–2.13) are solved by performing the radial sweep. The terms in boldface not yet taken into account in the first two steps have to be included into the discretization scheme for the radial sweep. These additional terms only depend on the hydrodynamic velocities v_ϑ and v_ϕ , which are a constant input value for the transport solver. Thus they do not couple the neutrino moments of neighbouring angular zones and can be added in a straightforward way. For each fixed pair of angles $(\vartheta_{k+\frac{1}{2}}, \phi_{l+\frac{1}{2}})$ along a radial ray, we employ exactly the same solution method as described in depth in Rampp & Janka (2002) to discretize the moment equations.

In order to solve Eqs. (2.12–2.13) the so-called variable Eddington factor technique is employed: The variable Eddington factors $f_K = K/J$ and $f_L = L/J$ closing the moment equations (2.12–2.13) are extracted from the solution of a model Boltzmann equation. For this purpose, it is sufficient to consider a simplified Boltzmann equation omitting some velocity dependent terms since the model Boltzmann equation is only used to compute normalized moments of the neutrino intensity. Thereby, the variable Eddington factors are calculated by an iteration procedure between the zeroth and first neutrino moment and the formal solution

of the Boltzmann equation. During the iteration, estimates of the moments J and H are obtained by a solution of the moment equations (2.12–2.13) to compute the source terms in the Boltzmann equation. With the right-hand side known, a formal solution of the model Boltzmann equation is computed by means of the so-called tangent ray method (Mihalas & Mihalas 1984; Rampp & Janka 2002). Once the Eddington factors are determined, the moment equations are solved to get an improved estimate for the neutrino moments. This procedure is iterated until the Eddington factors converge, and finally the moment equations are again numerically integrated to update the energy and electron fraction of the fluid. Since typically only a few iteration steps are required for numerical convergence, the entire procedure is computationally efficient.

The hyperbolic system of moment equations is discretized with fully backward, first-order accurate time differencing, and second-order accurate in space. This requires the solution of a linear system by means of a Newton-Raphson iteration with explicit construction and direct inversion of the corresponding Jacobian matrix.

The finite-volume discretization of the moment equations (2.12–2.13) guarantees conservation of the total neutrino energy up to order $\mathcal{O}(v^2/c^2)$. However, Rampp & Janka (2002) solve two additional moment equations for the neutrino number density $\mathcal{J} = J/\epsilon$ and number flux density $\mathcal{H} = H/\epsilon$ to guarantee also exact conservation of the neutrino number. In order to avoid this additional computational load, we use a special second-order finite difference representation for the terms governing advection in energy space developed by Müller et al. (2010).

In contrast to the multi-dimensional generalization of the variable Eddington factor method suggested by Rampp & Janka (2002), we determine the variable Eddington factors on each radial ray separately instead of determining the variable Eddington factors only once for an “angular averaged” radial ray, as done e.g. by Buras et al. (2006a). Although this procedure is computationally more intensive, it allows the code to be parallelized very efficiently.

The VERTEX code solves the fully coupled moment equations for the transport of electron neutrinos ν_e and anti-neutrinos $\bar{\nu}_e$, and, separately, the moment equations for one additional single neutrino species ν_x representing all other “heavy lepton neutrinos”. Treating muon and tauon neutrinos and their antiparticles as a single species is justified since in the inner core of a proto-neutronstar the fluid contains only few muons and tauons implying almost vanishing chemical potentials. Furthermore, the opacities are nearly equal for all “heavy lepton neutrinos”, although weak magnetism introduces an asymmetry between neutrinos and anti-neutrinos of all flavors (Horowitz 2002).

The moments of the collision integrals $C^{(n)}$ on the right-hand side of the moment equations are determined by various neutrino-matter and neutrino-neutrino interaction rates during the iteration procedure. An overview of the neutrino interactions is given in Table 2.1.

Reaction		References
νe^\pm	\rightleftharpoons	νe^\pm Mezzacappa & Bruenn (1993a) Cernohorsky (1994)
νA	\rightleftharpoons	νA Horowitz (1997) Langanke et al. (2008)
νN	\rightleftharpoons	νN Burrows & Sawyer (1998)
$\nu_e n$	\rightleftharpoons	$e^- p$ Burrows & Sawyer (1998)
$\bar{\nu}_e p$	\rightleftharpoons	$e^+ n$ Burrows & Sawyer (1998)
$\nu_e A'$	\rightleftharpoons	$e^- A$ Bruenn (1985), Mezzacappa & Bruenn (1993b) Langanke et al. (2003)
$\nu \bar{\nu}$	\rightleftharpoons	$e^- e^+$ Bruenn (1985), Pons et al. (1998)
$\nu \bar{\nu} NN$	\rightleftharpoons	NN Hannestad & Raffelt (1998)
$\nu_{\mu,\tau} \bar{\nu}_{\mu,\tau}$	\rightleftharpoons	$\nu_e \bar{\nu}_e$ Buras et al. (2003a)
$\nu_{\mu,\tau} \nu_e$	\rightleftharpoons	$\nu_{\mu,\tau} \nu_e$ Buras et al. (2003a)

Table 2.1: Overview of the neutrino-matter and neutrino-neutrino interactions included in the VERTEX code. The actual physical treatment of the specific rate calculations can be found in the corresponding references. The numerical implementation is given in Rampp & Janka (2002), Buras et al. (2003a), and Buras et al. (2006a). The symbol ν represents any neutrino or anti-neutrino, the symbols e^- , e^+ , n , p , denote electrons, positrons, free neutrons and protons, respectively, whereas A , and N are nuclei and nucleons.

2.2.4 Coupling to the Hydrodynamics

The neutrino transport equations (2.12–2.13) are coupled to the hydrodynamical part by the source terms

$$Q_N = -4\pi m_B \int_0^\infty d\epsilon \epsilon^{-1} \left(C_\nu^{(0)}(\epsilon) - C_{\bar{\nu}}^{(0)}(\epsilon) \right), \quad (2.22)$$

$$Q_E = -4\pi \int_0^\infty d\epsilon \sum_\nu C_\nu^{(0)}(\epsilon), \quad (2.23)$$

$$Q_{Mr} = -\frac{4\pi}{c} \int_0^\infty d\epsilon \sum_\nu C_{r,\nu}^{(1)}(\epsilon), \quad (2.24)$$

$$Q_{M\vartheta} = -\frac{4\pi}{c} \int_0^\infty d\epsilon \sum_\nu C_{\vartheta,\nu}^{(1)}(\epsilon), \quad (2.25)$$

$$Q_{M\phi} = -\frac{4\pi}{c} \int_0^\infty d\epsilon \sum_\nu C_{\phi,\nu}^{(1)}(\epsilon), \quad (2.26)$$

where m_B denotes the baryon mass, $C_\nu^{(0)}$ the zeroth and $C_{r,\nu}^{(1)}, C_{\vartheta,\nu}^{(1)}, C_{\phi,\nu}^{(1)}$ the r -, ϑ -, and ϕ -component of the first moment of the collision integral. The source terms depend on the sum of the moments of the collision integral over all neutrino types $\nu \in \{\nu_e, \bar{\nu}_e, \nu_\mu, \bar{\nu}_\mu, \nu_\tau, \bar{\nu}_\tau\}$. In the following the index ν is suppressed for the sake of simplicity.

The “ray-by-ray-plus” approach to multi-dimensional neutrino transport assumes the lateral and azimuthal fluxes in the co-moving frame to be zero, enforcing a radial flux. However, Buras et al. (2006a) pointed out that the angular components of the momentum transfer from

neutrinos to the hydrodynamic fluid, described by the source terms $Q_{M\vartheta}$ and $Q_{M\phi}$ have to be included in the Euler equation of hydrodynamics when the neutrinos are tightly coupled to the medium in the optical thick regime. Therefore, one should solve the moment equations for both non-radial fluxes to get the lateral and azimuthal transport of neutrino momentum. Under the assumption of a purely radial neutrino flux and a diagonal neutrino pressure tensor, these equations read

$$\begin{aligned} C_\vartheta^{(1)}(\epsilon) &= \left(\frac{\partial \beta_\vartheta}{\partial r} - \frac{\beta_\vartheta}{r} \right) H + \frac{1}{2r} \frac{\partial(J-K)}{\partial \vartheta} + \frac{1}{2c} \frac{\partial \beta_\vartheta}{\partial t} (3J-K) \\ &\quad + \frac{\beta_\vartheta}{2c} \frac{\partial(J-K)}{\partial t} - \frac{\partial}{\partial \epsilon} \left\{ \epsilon \left[\frac{1}{2c} \frac{\partial \beta_\vartheta}{\partial t} (J-K) \right. \right. \\ &\quad \left. \left. + \frac{1}{2} \left(\frac{1}{r} \frac{\partial \beta_r}{\partial \vartheta} - \frac{\beta_\vartheta}{r} \right) (H-L) \right] \right\}, \end{aligned} \quad (2.27)$$

$$\begin{aligned} C_\phi^{(1)}(\epsilon) &= \left(\frac{\partial \beta_\phi}{\partial r} - \frac{\beta_\phi}{r} \right) H + \frac{1}{2r \sin \vartheta} \frac{\partial(J-K)}{\partial \phi} + \frac{1}{2c} \frac{\partial \beta_\phi}{\partial t} (3J-K) \\ &\quad + \frac{\beta_\phi}{2c} \frac{\partial(J-K)}{\partial t} - \frac{\partial}{\partial \epsilon} \left\{ \epsilon \left[\frac{1}{2c} \frac{\partial \beta_\phi}{\partial t} (J-K) \right. \right. \\ &\quad \left. \left. + \frac{1}{2} \left(\frac{1}{r \sin \vartheta} \frac{\partial \beta_r}{\partial \phi} - \frac{\beta_\phi}{r} \right) (H-L) \right] \right\}. \end{aligned} \quad (2.28)$$

Since we want to describe the lateral moment transfer of neutrinos in the optically thick regime, one can assume neutrino diffusion and thus an isotropic neutrino distribution (i.e. $J \equiv 3K$). Following Buras et al. (2006a), this approximation implies that the first term on the right-hand side vanishes in Eqs. (2.27–2.28) if we ignore neutrino viscosity. One can also assume stationary conditions, i.e. $\partial/\partial t \equiv 0$. When integrating over the neutrino energy, the terms with the energy derivative in Eqs. (2.27–2.28) cancel and thus the two moment equations simplify significantly:

$$\int_0^\infty d\epsilon C_\vartheta^{(1)}(\epsilon) = \int_0^\infty d\epsilon \frac{1}{2r} \frac{\partial(J-K)}{\partial \vartheta} = \int_0^\infty d\epsilon \frac{1}{3r} \frac{\partial J}{\partial \vartheta}, \quad (2.29)$$

$$\int_0^\infty d\epsilon C_\phi^{(1)}(\epsilon) = \int_0^\infty d\epsilon \frac{1}{2r \sin \vartheta} \frac{\partial(J-K)}{\partial \phi} = \int_0^\infty d\epsilon \frac{1}{3r \sin \vartheta} \frac{\partial J}{\partial \phi}. \quad (2.30)$$

The numerical discretization of Eqs. (2.29–2.30) reads

$$C_\vartheta^{(1)}_{i+\frac{1}{2}, k+\frac{1}{2}, l+\frac{1}{2}} = \frac{J_{i+\frac{1}{2}, k+\frac{3}{2}, l+\frac{1}{2}} - J_{i+\frac{1}{2}, k-\frac{1}{2}, l+\frac{1}{2}}}{3 r_{i+\frac{1}{2}} (\vartheta_{k+\frac{3}{2}} - \vartheta_{k-\frac{1}{2}})}. \quad (2.31)$$

$$C_\phi^{(1)}_{i+\frac{1}{2}, k+\frac{1}{2}, l+\frac{1}{2}} = \frac{J_{i+\frac{1}{2}, k+\frac{1}{2}, l+\frac{3}{2}} - J_{i+\frac{1}{2}, k+\frac{1}{2}, l-\frac{1}{2}}}{3 r_{i+\frac{1}{2}} \sin \vartheta_{k+\frac{1}{2}} (\phi_{l+\frac{3}{2}} - \phi_{l-\frac{1}{2}})}. \quad (2.32)$$

With the help of the neutrino source terms $Q_{M\vartheta}$ and $Q_{M\phi}$ determined by Eqs. (2.25–2.26) together with Eqs. (2.29–2.30) we are able to compute the momentum transfer between neutrinos and the stellar fluid. Together with the neutrino advection terms appearing in the neutrino transport equations (2.12–2.13), we can properly describe neutrino convection in the proto-neutron star.

The aforementioned assumptions for Eqs. (2.29–2.30) are only valid in the optically thick core of the supernova and thus, $C_{\vartheta}^{(1)}_{i+\frac{1}{2}, k+\frac{1}{2}, l+\frac{1}{2}} = 0$ and $C_{\phi}^{(1)}_{i+\frac{1}{2}, k+\frac{1}{2}, l+\frac{1}{2}} = 0$ are just evaluated if the density $\rho_{i+\frac{1}{2}, k+\frac{1}{2}, l+\frac{1}{2}}$ in a zone is higher than 10^{12} g cm $^{-3}$. This threshold value is specifically chosen for the core-collapse supernova environment, since matter becomes optically thin to neutrinos around this density and momentum transfer and the advection of neutrinos ceases.

3 The Progenitor Structure Dependence of the Explosion Mechanism in Axisymmetry

Multi-dimensional simulations of core-collapse supernova explosions with detailed neutrino transport have long been restricted to a handful of numerical models. Thus, until now just a rather small number of progenitors could be evolved into the explosion phase by the means of multi-dimensional simulations with spectral neutrino transport. (Buras et al. 2006b; Marek & Janka 2009; Müller et al. 2012b,a; Bruenn et al. 2013; Suwa et al. 2010). These simulations focused on a few selected progenitor stars. Although still restricted to axisymmetry, we present a broad study of the progenitor structure dependence of the explosion mechanism for the first time. To do so, we employ the fully self-consistent radiation hydrodynamics code VERTEX-PROMETHEUS described in the previous chapter.

Recently, O'Connor & Ott (2011) performed a systematic study of failing core-collapse supernovae and investigated how the zero-age main sequence (ZAMS) mass of the progenitor stars determines black hole formation. Employing a neutrino leakage scheme instead of full transport and restricting their simulation set to spherical symmetry (i.e. 1D), they identified a single parameter, the compactness of the stellar core at bounce, to estimate the outcome of a core-collapse supernova, i.e. whether the star explodes or a black hole is formed. Ugliano et al. (2012) performed a large set of supernova simulations in spherical symmetry with a more elaborate treatment of the neutrino transport focusing on the progenitor-explosion and progenitor-remnant connection. Applying the grey approximation of neutrino transport of Scheck et al. (2006) they calibrate their method such that the explosion properties of progenitors around 20 solar masses are compatible with SN 1987A. They found that all stars below $\sim 15 M_{\odot}$ yield neutron stars, whereas more massive progenitors can produce either black holes or neutron stars. For the purpose of the study presented here, we choose progenitor models which are promising candidates for successful explosions according to the results of Ugliano et al. (2012). Here, we overcome two significant restrictions of the mentioned studies, although our model set is not as large as the simplified ones of O'Connor & Ott (2011) or Ugliano et al. (2012) due to the tremendous requirement of computing resources of our simulations with full neutrino transport: On the one hand the models presented here are performed in multi dimensions allowing the development of non-radial instabilities, such as convection, and, on the other hand the simulations are fully self-consistent without any parametrization.

With the set of self-consistent, multi-dimensional simulations presented in this chapter we aim to address the following questions:

- Does the neutrino-driven explosion mechanism of core-collapse supernovae work for a wide range of progenitors?
- What is the progenitor-explosion connection in the context of self-consistent core-collapse supernova simulations? How is the onset of the explosion determined by the

progenitor structure?

- Is the threshold criterion for successful and failing core-collapse supernovae determined by O'Connor & Ott (2011) and Ugliano et al. (2012) valid?
- Can the critical condition identified by Burrows & Goshy (1993), which can be considered to separate exploding from nonexploding models, applied to our model set?
- What is driving the explosion? Which kind of instability is responsible for triggering a runaway condition of the hydrodynamic flow behind the supernova shock?

We will complete this chapter by comparing our results obtained with the VERTEX-PROMETHEUS code with the axisymmetric simulations of Bruenn et al. (2013) and a summarize of our findings.

3.1 Overview of the investigated Set of axisymmetric Simulations

The simulations presented in this chapter were performed assuming axisymmetry (i.e. 2D) with the VERTEX-PROMETHEUS simulation code discussed in Chapter 2. From the onset of gravitational collapse until 10 ms after shock formation, all models are simulated in spherical symmetry. At this point, the multidimensional simulations are started from the 1D models by imposing random seed perturbations of the density with an amplitude of 0.1 % to allow for the growth of aspherical instabilities. As demonstrated by Buras et al. (2006b), it makes hardly any difference whether a non-rotating model is computed in multi dimensions from the onset of gravitational collapse or whether the described method is used, since hydrodynamic instabilities do not develop before shock formation.

The axisymmetric simulations are computed on a spherical polar grid with initially 400 non-equidistant radial and 128 angular zones. The radial zones are distributed from the center to an outer boundary of 10000 km, which is sufficiently far out to ensure that the gas there remains at rest until the simulations are stopped several hundred milliseconds after core-bounce. The altitudinal grid runs from the north to the south pole of the 2D grid, which corresponds to an angular resolution of 1.41°. During the simulations the number of radial grid zones is increased to ensure adequate resolution in the proto-neutron-star surface region, where the density gradient steepens with time due to the shrinking of the neutron star. The innermost 1.6 km of the inner core of the star (corresponding to the innermost 6 radial zones) are computed in spherical symmetry to avoid excessive time step limitations imposed by the CFL condition. Here, the Courant-Friedrichs-Lowy condition (Courant et al. 1928) is a necessary condition for the numerical stability of the explicit hydrodynamics solver. It requires that the time step of the explicit algorithm has to be sufficiently small so that no information can travel more than one zone. Thus, the CFL time step is minimal at the center of the employed spherical grid, because the lateral width of a zone becomes very small.

For the first time, it is possible to perform a large set of multi-dimensional simulations with fully self-consistent elaborate neutrino treatment until very late after bounce. A single model requires continuous computing on 128 strong individual computing cores for several months. In Table 3.1 we summarize the investigated models. Fourteen runs are based on the presupernova models of Woosley et al. (2002) and four on the models of Woosley & Heger (2007).

Model	M_{ZAMS} [M_{\odot}]	$\xi_{1.75}$	$\xi_{2.5}$	t_{exp} [ms]	L_{exp} $[10^{52} \text{ erg/s}]$	\dot{M}_{exp} [M_{\odot}/s]	M_{NS} [M_{\odot}]
s11.2	11.2	0.073	0.005	332	1.90	0.117	1.33
s12.4	12.4	0.265	0.028	634	2.14	0.142	1.61
s13.2	13.2	0.335	0.049	610	2.42	0.152	1.66
s14.4	14.4	0.514	0.124	733	2.61	0.195	1.79
s16.8	16.8	0.353	0.158	480	2.52	0.244	1.59
s17.2	17.2	0.368	0.168	402	2.62	0.259	1.59
s18.4	18.4	0.653	0.188	520	4.25	0.342	1.85
s19.6	19.6	0.296	0.119	361	2.68	0.144	1.61
s20.2	20.2	0.250	0.105	355	2.21	0.120	1.59
s21.6	21.6	0.464	0.181	505	2.86	0.266	1.70
s22.4	22.4	0.531	0.200	395	3.09	0.291	1.71
s26.6	26.6	0.561	0.227	325	2.89	0.251	1.71
s27.0	27.0	0.523	0.232	395	2.78	0.264	1.71
s28.0	28.0	0.516	0.235	414	2.89	0.257	1.71
s12-2007	12	0.232	0.023	750	2.02	0.142	1.58
s15-2007	15	0.545	0.181	549	3.42	0.398	1.77
s20-2007	20	0.770	0.285	295	3.77	0.385	1.83
s25-2007	25	0.813	0.329	342	3.71	0.373	1.92

Table 3.1: Summary of the investigated axisymmetric models based on the presupernova models of Woosley et al. (2002) and Woosley & Heger (2007), where the latter models are labelled with “-2007”. For each model the ZAMS mass is given, followed by the compactness parameters $\xi_{1.75}$ and $\xi_{2.5}$ determined from the presupernova model data. Next, the time t_{exp} is specified, when the onset of explosion takes place. For the explosion time t_{exp} we give the electron neutrino luminosity L_{exp} , the mass accretion rate \dot{M}_{exp} , and the neutron star mass M_{NS} .

In the following, we focus on the first large set of models, while we discuss the simulations based on the progenitor profiles of Woosley & Heger (2007) separately in Section 3.7.

In Table 3.1, we list the compactness parameters $\xi_{1.75}$ and $\xi_{2.5}$ for each model together with its zero-age main-sequence (ZAMS) mass. According to Equation (10) of O’Connor & Ott (2011) it is defined as

$$\xi_M = \frac{M/M_{\odot}}{R(M_{\text{bary}}=M)/1000 \text{ km}}, \quad (3.1)$$

where we set either $M = 1.75 M_{\odot}$ or $M = 2.5 M_{\odot}$. The radius $R(M_{\text{bary}})$ is the radial coordinate that encloses this mass. Although O’Connor & Ott (2011) insisted that it is crucial to compute ξ_M at core bounce as the only physical and unambiguous point to determine the initial conditions for the postbounce dynamics, there is no perceivable difference whether ξ_M is evaluated at the onset of gravitational collapse or at the time of bounce for the investigated solar-metallicity progenitors (Uglio et al. 2012). The mass shells enclosing $M = 1.75 M_{\odot}$ or $M = 2.5 M_{\odot}$ are hardly affected by gravitational collapse until core bounce. We directly evaluate the compactness parameters from the presupernova data, since our simulation grid does not cover the mass shells enclosing $M = 2.5 M_{\odot}$ of models with a low compactness

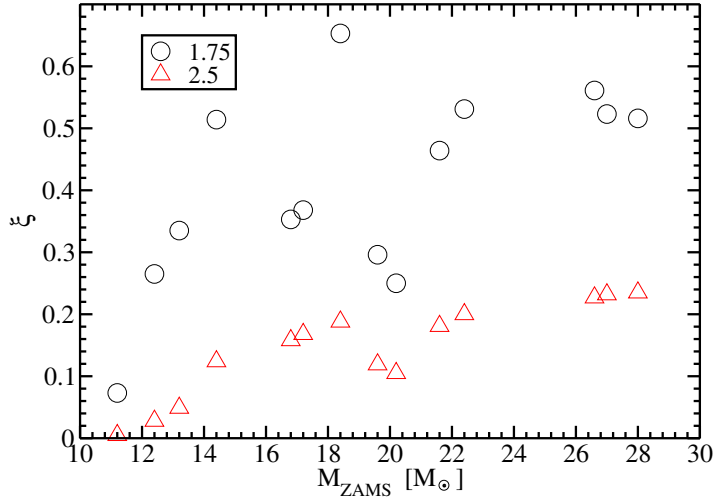


Figure 3.1: Compactness parameter for the fourteen investigated presupernova models of Woosley et al. (2002) versus ZAMS mass as evaluated from the presupernova data. Both investigated parameters $\xi_{1.75}$ and $\xi_{2.5}$ are shown. The precollapse structure and the ZAMS mass are completely uncorrelated.

parameter.

Performing spherically symmetric simulations, O'Connor & Ott (2011) found that neutrino-driven explosions can be launched up to a compactness parameter $\xi_{2.5} \leq 0.45$, while above this threshold black holes are formed. However, Ugliano et al. (2012) determined in their study a significantly lower limit for black hole formation. While not specifying a sharp dividing line, they saw a wide range of $\xi_{2.5}$ values between around 0.15 and 0.35 where explosions can both occur and fail. Although our simulation set is limited, we aim to investigate how the self-consistent and the multi-dimensional character of our study affects or shifts the limit of $\xi_{2.5}$ for driving explosions. As shown in Figure 3.1 the computed models are chosen such that all progenitors experience a progenitor compactness below $\xi_{2.5} \sim 0.235$. All of the corresponding models of Ugliano et al. (2012) explode according to their chosen calibration making this progenitors promising candidates for successful explosions. While O'Connor & Ott (2011) chose $M = 2.5 M_{\odot}$ for the compactness parameter of the progenitor as the relevant mass scale for black hole formation, focusing on the preexplosion phase as we are doing, O'Connor & Ott (2013) use $\xi_{1.75}$. Because of the much smaller relevant mass scale, this parameter might be better suited for the investigation of the postbounce preexplosion phase and is displayed in Figure 3.1. Both values differ. While the parameter $\xi_{2.5}$ exhibits a clear trend with a small spread of the individual value, $\xi_{1.75}$ reflects the lower mass range of the progenitor structure more individually. Note also that we do not investigate any model in the mass range of $22 - 25 M_{\odot}$ with high compactness as these models do not explode in the parametric study of Ugliano et al. (2012).

Besides the progenitor-dependent compactness parameter, the precise density structure of the individual presupernova models is an important factor for the development of an explosion. For each model, the density structure versus radius and versus enclosed mass is displayed in Figure 3.2. Remarkably, for all heavier investigated models between 19 and 28 solar masses the interface between the silicon shell and the oxygen-enriched silicon shell is located at the

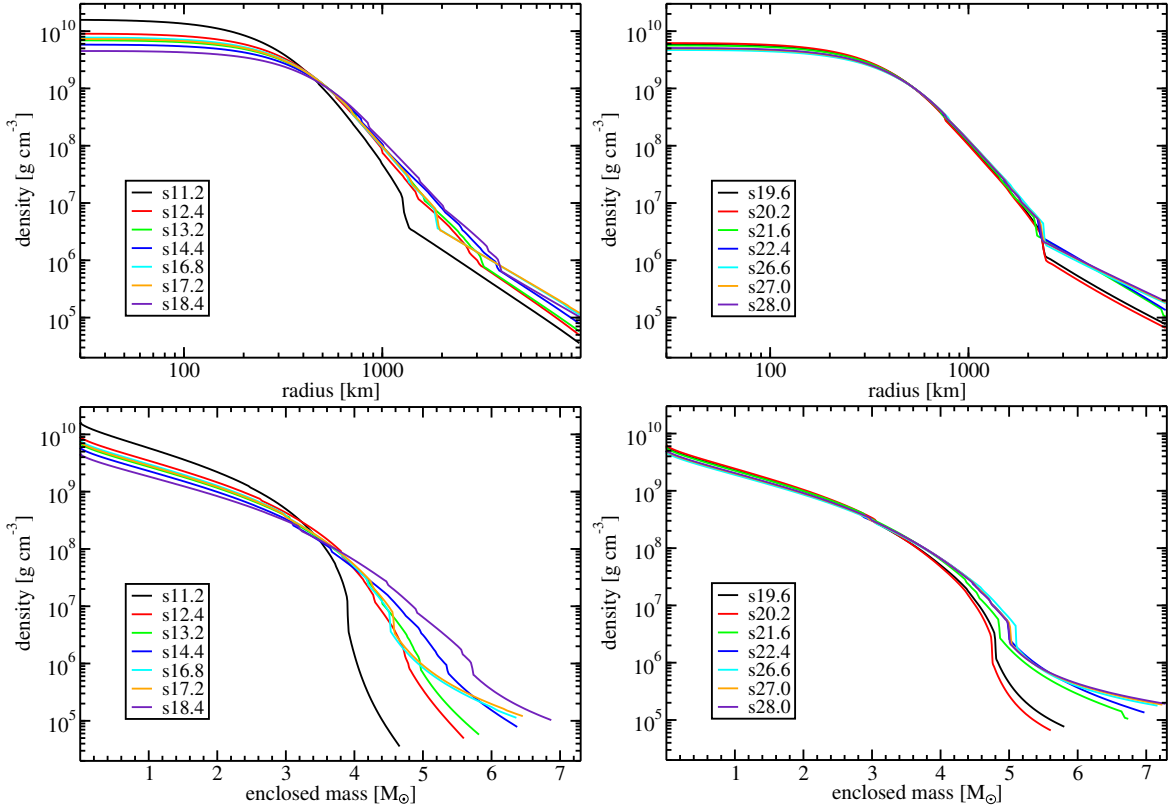


Figure 3.2: Density profiles vs. radius (top) and vs. enclosed mass (bottom) for progenitors of Woosley et al. (2002) covering the inner 10000 km (i.e. the computational domain) at the onset of core collapse. The left panels show models with lower ZAMS mass and the right panels model with higher ZAMS mass.

same position, for example at around 2500 km for the $19.6 M_{\odot}$ star model. This boundary layer is very pronounced and connected to a steep decline of the density at this position. However, lower mass models vary in the position of the weaker Si/SiO interface. Especially, the models with a ZAMS mass of 12.4, 13.2, 14.4, and 18.4 solar masses encounter almost no noticeable jump in the density profile.

3.2 Dependence of the Postbounce Evolution on the Precollapse Structure

Trajectories of the average shock radius are depicted in Figure 3.3. All of the investigated models explode as predicted by Ugliano et al. (2012). However, the overall postbounce evolution depends significantly on the individual model with a wide variation of the onset of the explosion in time. Models shown in the right panel of Figure 3.3 with higher ZAMS mass evolve in a similar manner. The shock retreats until around 220 ms after bounce when the Si/SiO composition-shell interface reaches the accretion shock. This point of time is connected to a steep decrease of the mass accretion rate (Figure 3.4). Shortly afterward the shock starts to expand, and after some time the runaway condition for an explosion is reached.

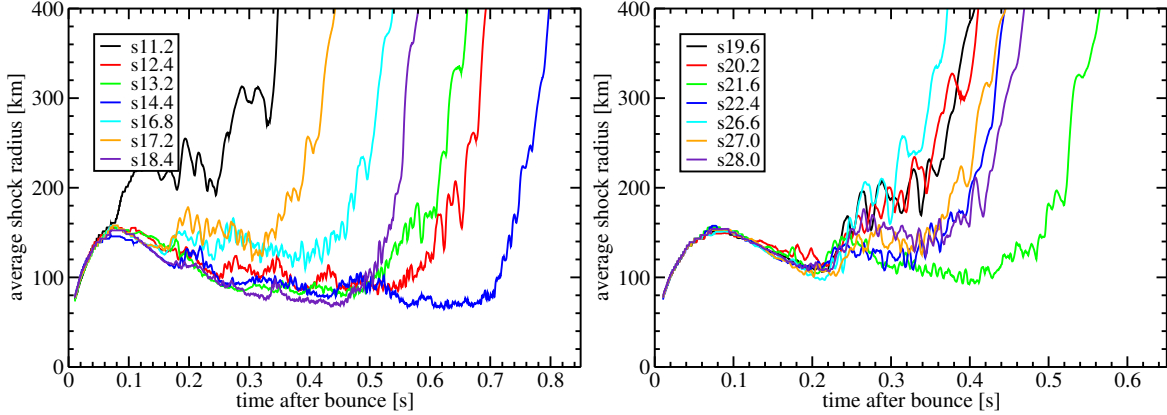


Figure 3.3: Time evolution of the average shock radius for models with lower ZAMS mass (left panel) and with higher ZAMS mass (right panel). The shock position is defined as the surface average over all angular directions. The models with lower ZAMS mass show a fully uncorrelated onset of the explosion, whereas the heavier models mainly start to explode shortly after the boundary between the silicon shell and the oxygen-enriched silicon shell is reached.

Most outstanding examples are models “s19.6” and “s20.2” with a very strong interface. The shock of these models expands almost continuously outward after the arrival of the interface. The time delay between the arrival of the interface and the development of an explosion is largest for model “s21.6”, since for this case the steep decrease of the mass accretion rate is smallest compared to the other cases. Mainly, for the low mass progenitors (12.4, 13.2, 14.4 and also 18.4 solar mass cases) the situation changes. Connected to a much weaker Si/SiO composition-shell interface (see Figure 3.2), the mass accretion rate depicted in the left panel of Figure 3.4 decreases smoother and there is no steep drop of the mass accretion rate. These models have in common that they explode relatively late although at different points of time when the mass accretion rate has decreased sufficiently. As the most extreme model, the 14.4 solar mass case even explodes as late as 733 ms after shock formation. It is astonishing that an explosion can still be triggered at such a late time after bounce. For the sake of completeness, we also included the 11.2 solar mass case in our study, which has been studied intensively in previous works (Buras et al. 2006b; Marek & Janka 2009; Müller et al. 2012b). Here, the Si/SiO composition-shell interface arrives already at around 80 ms after bounce at the shock surface and at this point of time the mass accretion rate drops steeply to a much lower value of $0.19 M_{\odot}/s$ than the other models. Thus, contrary to the other models with a higher ZAMS mass, the shock of this particular model is pushed out very early (see left panel of Figure 3.3 and the explosion model of Buras et al. 2006b; Marek & Janka 2009). Due to the peculiar character of this model, it does not fit to the rest of the model set, and we consider it as a special case.

Why does our model set split into two subsets with on the one hand heavier models with the tendency to earlier explosions and on the other hand lighter models experiencing late explosions? This question can be understood in the context of a critical value of the neutrino luminosity acting against the mass accretion rate onto the stalled supernova shock that is required to drive a neutrino-driven explosion (e.g., Burrows & Goshy 1993; Janka 2001; Fernández 2012). In the framework of this concept, the supernova shock can be revived when

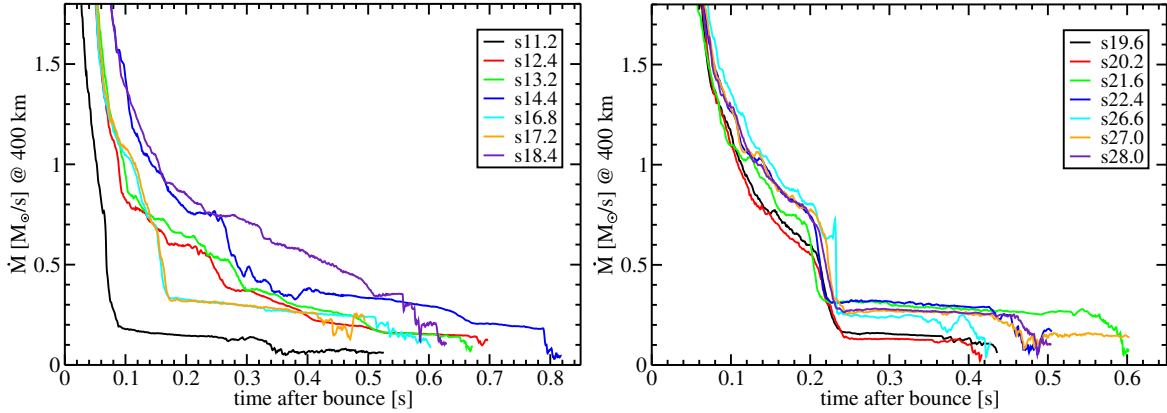


Figure 3.4: Time evolution of the mass accretion rate, $\dot{M}(r) = 4\pi r^2 \rho(r) |v(r)|$, evaluated at 400 km for models with lower ZAMS mass (left panel) and with higher ZAMS mass (right panel). Models with a steep decrease of the mass accretion rate connected to the arrival of the boundary between the silicon shell and the oxygen-enriched silicon shell tend to explode easily and relatively fast. After the strongly aspherical shock surface passes a distance of 400 km from the center, the evaluation of the mass accretion rate is influenced by strong mass motions behind the supernova shock front.

either the neutrino luminosity and thus the neutrino-heating rate in the gain layer is sufficient high or the mass accretion rate is low enough. Later, we will focus in more detail on the concept of a critical condition that separates exploding from non-exploding models (Burrows & Goshy 1993). Models, which tend to explode earlier, have, in general, a higher ZAMS mass of at least 16 solar masses. The luminosities of electron- and electron-antineutrinos of these models depicted in Figure 3.5 are relatively high in the first two hundred milliseconds of the postbounce evolution, because the high mass accretion rate at this time period (see Figure 3.4) induces a high accretion luminosity. Thus, lots of neutrinos deposit energy in the gain layer and heat the region behind the stalled shock. A higher mass accretion rate and thus more neutrino heating before the arrival of the interface is supportive for a faster explosion. For example, compared to the similar case “s22.4”, the mass accretion rate of model “s21.6” is lower before the earlier drop of the mass accretion rate. Thus, the gain region of this model is less heated in the early postbounce evolution and explodes later. When the Si/SiO composition-shell interface arrives at the shock, which is also reflected in a drop of the neutrino luminosities and mean energies (Figures 3.5, 3.6), the ram pressure of the material falling on the stalled supernova shock is reduced, although there is still a lot of energy stored in the gain layer due to the high accretion luminosity. This combination is very supportive for the revival of the shock. Furthermore, it is necessary that then the mass accretion rate is sufficiently low enough that the neutrino heating of the gain layer can overcome the ram pressure of the material falling on the shock. Empirically, the mass accretion rate of the investigated models has to drop below a value of somewhat below $0.3 M_{\odot}/s$ to reach hydrodynamic conditions favorable for an explosion (see Table 3.1 for the exact values of the mass accretion rate at the point of explosion and the discussion in the next section). Since compared to other heavier models the mass accretion rate of the two models “s19.6” and “s20.2” is significantly lower after the Si/SiO interface passed the shock, these models can explode earlier. The explosion of the light models with 12.4, 13.2, and 14.4 solar masses is delayed for several hundred milliseconds. The Si/SiO interface of these models is relatively weak and thus it takes a long

3. The Progenitor Structure Dependence of the Explosion Mechanism in Axisymmetry

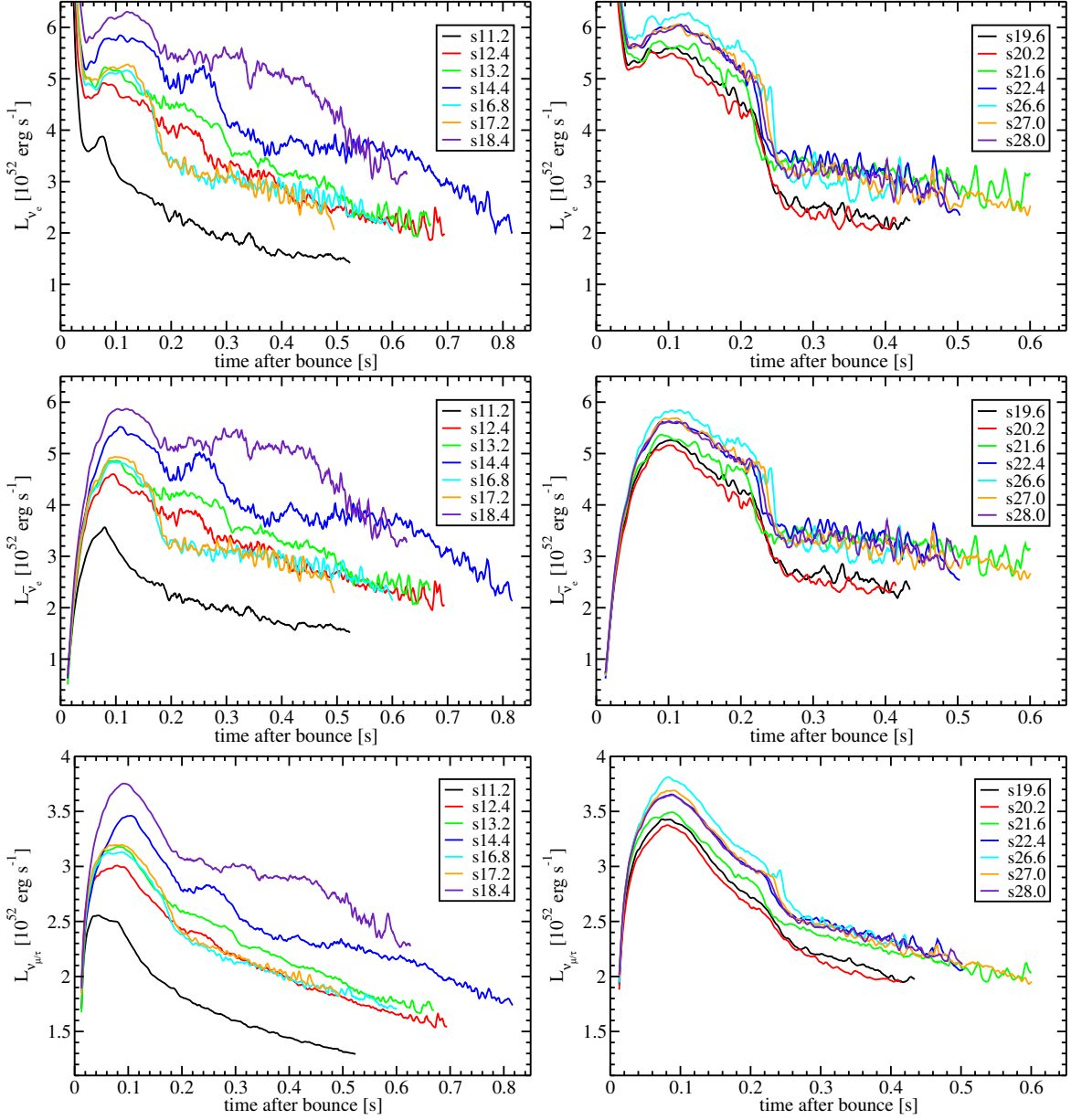


Figure 3.5: Time evolution of neutrino luminosities for models with lower ZAMS mass (left panel) and with higher ZAMS mass (right panel). The upper, middle, and lower panels indicate the luminosities for ν_e , $\bar{\nu}_e$, and $\nu_{\mu/\tau}$, respectively. Angular averaged quantities are extracted at a fiducial observer radius of 400 km. Note that the curves have been smoothed using a running average over 5 ms.

time until the mass accretion rate decreased so far that neutrino heating can overcome the ram pressure. Model “s18.4” is an interesting case. Here, shock revival happens after 520 ms at a still high mass accretion rate of $0.342 M_{\odot}/\text{s}$. The continuously decreasing mass accretion rate is still such high, that a lot of hot matter accreted on the neutron star induces a high neutrino luminosity (Figure 3.5) and neutrino heating to push the shock outwards against the still huge amount of accreted matter. In total, our model set fully confirms the concept of a

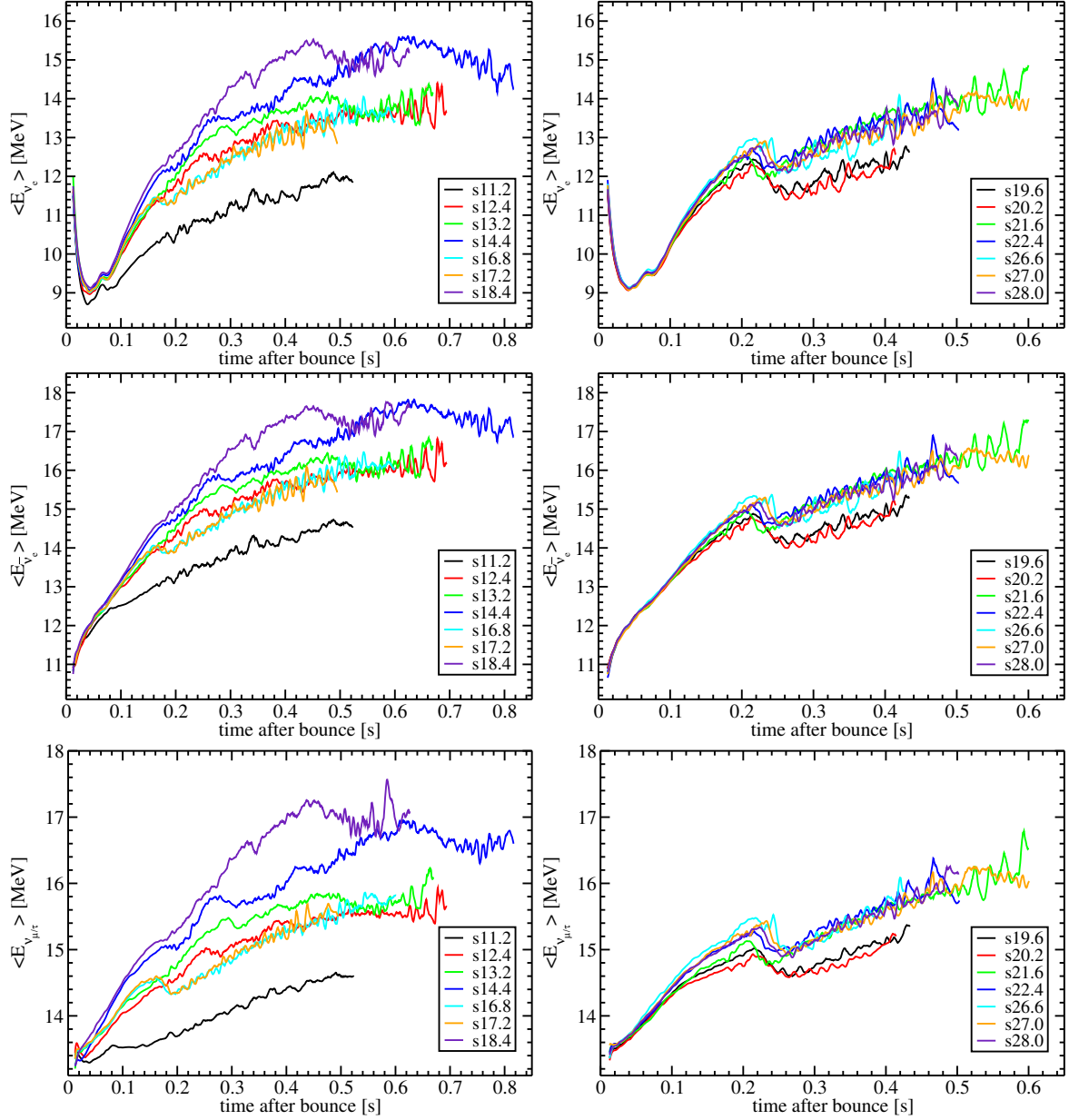


Figure 3.6: Time evolution of neutrino mean energies for models with lower ZAMS mass (left panel) and with higher ZAMS mass (right panel). The upper, middle, and lower panels indicate the mean energies for ν_e , $\bar{\nu}_e$, and $\nu_{\mu/\tau}$, respectively. Angular averaged quantities are extracted at a fiducial observer radius of 400 km. Note that the curves have been smoothed using a running average over 5 ms.

favorable interplay of the neutrino luminosity and the mass accretion rate and demonstrates a strong dependence on the specific progenitor structure.

What are the implications of our simulations so far? Most importantly, all models explode, although their detailed progenitor structure is very different. Thus, according to Table 3.1 (see also Fig 3.1) self-consistent explosions are possible up to a compactness parameter of at

least $\xi_{2.5} = 0.235$. This value fits into the range of compactness parameter between $\xi_{2.5} = 0.15$ and $\xi_{2.5} = 0.35$ of Ugliano et al. (2012), where successful and failing supernova explosions are possible. However, in this study our aim is to demonstrate that the neutrino-driven supernova mechanism works for a wider range of progenitors self-consistently and we have chosen optimistic cases of the study of Ugliano et al. (2012). Scanning a further sequence of self-consistent and multi-dimensional models, one could determine the final threshold value of the compactness parameter for an explosion. Remarkably, the compactness parameter of the exploding model “s25-2007” based on a 25 solar mass progenitor of Woosley & Heger (2007), which will be discussed later in Section 3.7, amounts to $\xi_{2.5} = 0.329$. That is almost the upper threshold value of Ugliano et al. (2012). It is still an interesting question to determine the exact location of islands of black hole formation in the mass range between 15 and 30 solar masses investigating failing cases of Ugliano et al. (2012). We have shown that the onset of the explosion strongly depends on the detailed progenitors structure. Presupernova models of Woosley et al. (2002) with a higher compactness parameter explode easier and faster than models with a lower compactness parameter. Thus, there is no direct correlation between the explosion time (see Table 3.1) and the compactness parameter.

Although we have already discussed the principal evolution of our models, the detailed investigation of the driving explosion mechanism is still missing. We will continue the discussion with an analysis of the conditions in the gain region behind the supernova shock front.

3.3 Conditions in the Gain Layer

As already mentioned, the stalled accretion shock can be revived if neutrino heating behind the shock is sufficient strong to compete with the downward advection of gas in the gain layer (e.g., Burrows & Goshy 1993; Janka 2001). In other words, the conditions in the gain layer become favorable for an explosion if the “advection timescale” measuring the time the accreted gas requires to pass the gain layer becomes longer than the “heating timescale” needed for neutrino heating to deposit an energy equivalent to the binding energy of the matter. Thus, the shock can expand sufficiently to create a runaway situation eventually leading to an explosion when $\tau_{\text{adv}}/\tau_{\text{heat}} \gtrsim 1$ holds for a sufficiently long time (Janka 2001; Thompson et al. 2005; Fernández 2012). Indeed, in 2D simulations (Buras et al. 2006b; Scheck et al. 2008; Murphy & Burrows 2008; Marek & Janka 2009) it has been shown that the timescales τ_{adv} and τ_{heat} are useful diagnostic quantities for understanding the specific outcome of the simulation runs.

In principle, we follow the analysis framework of Müller et al. (2012b) for properties of the gain layer, which is mainly based on the definitions proposed in Buras et al. (2006b) and Marek & Janka (2009). For spherically symmetric setups, one can simply define the advection timescale τ_{adv} as a measure how long accreted matter with an average postshock velocity $\langle v_r \rangle$ needs to fall from the shock R_s to the gain radius R_g ,

$$\tau_{\text{adv}} = \int_{R_g < r < R_s} \frac{1}{|\langle v_r \rangle|} dr . \quad (3.2)$$

To generalize this definition to a multi-dimensional situation, when nonradial instabilities influence significantly the postshock flow, several possibilites have been proposed in the liter-

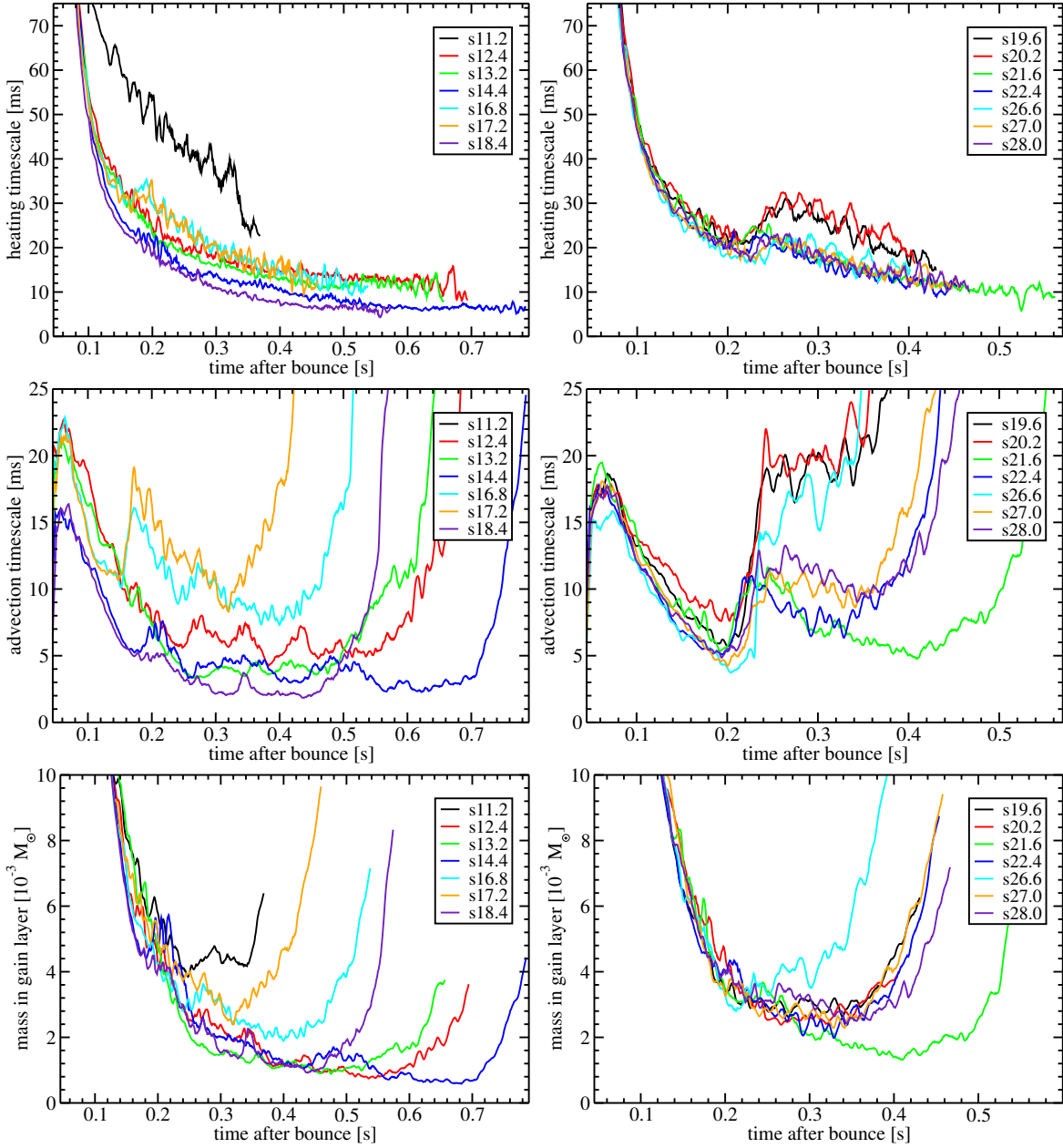


Figure 3.7: Time evolution of diagnostic quantities for the conditions in the gain layer for models with lower ZAMS mass (left panel) and with higher ZAMS mass (right panel). The heating timescale (top), the advection timescale (middle), and the mass in the gain layer (bottom) are shown. The definitions of these diagnostic quantities are given in the text. Note that the curves have been smoothed using a running average over 5 ms.

ature (Buras et al. 2006b; Marek & Janka 2009; Scheck et al. 2008; Murphy & Burrows 2008; Pejcha & Thompson 2012). Following Müller et al. (2012b) and Janka (2012) we choose a measure of the of the advection timescale, which can be evaluated readily, the dwelling time

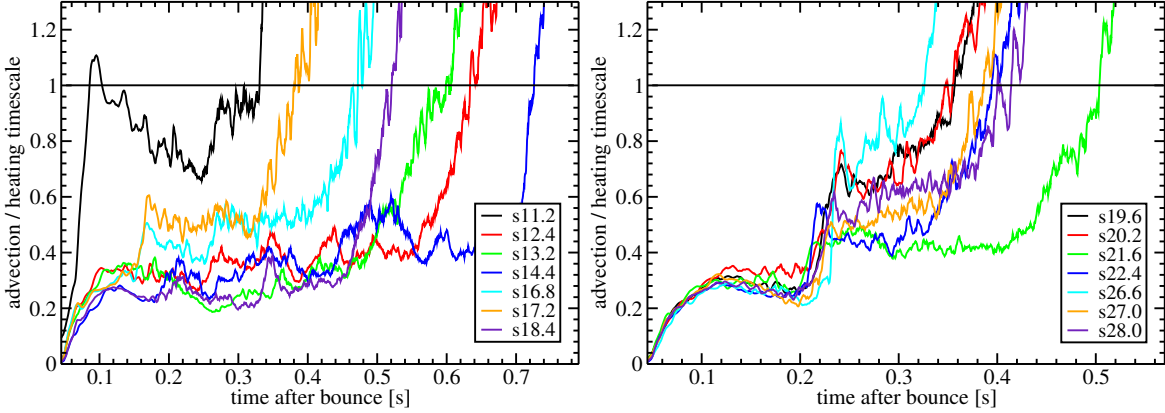


Figure 3.8: Time evolution of the ratio of the advection timescale to the heating timescale in the gain layer for models with lower ZAMS mass (left panel) and with higher ZAMS mass (right panel). Note that the curves have been smoothed using a running average over 5 ms.

of matter in the gain layer (Buras et al. 2006b; Marek & Janka 2009):

$$\tau_{\text{dwell}} \approx \frac{M_{\text{gain}}}{\dot{M}}, \quad (3.3)$$

where \dot{M} is the mass accretion rate of the gas through the shock and M_{gain} is given by the mass enclosed in the gain layer between the gain radius R_g and the shock radius R_s ,

$$M_{\text{gain}} = \int_{R_g < r < R_s} \rho dV. \quad (3.4)$$

Thus, the dwelling timescale can be expressed by two readily available quantities, which allows for a straightforward evaluation of this quantity.

The second timescale, the heating timescale, is computed as the ratio of the binding energy E_{bind} of the material in the gain layer and the volume-integrated neutrino heating rate \dot{Q}_{heat} in that region,

$$\tau_{\text{heat}} = \frac{E_{\text{bind}}}{\dot{Q}_{\text{heat}}}. \quad (3.5)$$

Here, the binding energy E_{bind} is the volume integral over the sum of the specific kinetic, internal, and gravitational binding energy in the gain layer,

$$E_{\text{bind}} = \int_{R_g < r < R_s} \left[\rho \left(\frac{v^2}{2} + \epsilon \right) + \rho \Phi \right] dV, \quad (3.6)$$

and the neutrino heating rate \dot{Q}_{heat} is the integrated neutrino energy deposition rate per volume q_e in the gain layer,

$$\dot{Q}_{\text{heat}} = \int_{R_g < r < R_s} q_e dV. \quad (3.7)$$

In Figure 3.7 we summarize the heating and the advection timescale as well as the mass in the gain layer for all investigated models. The general trends discussed in the previous section are

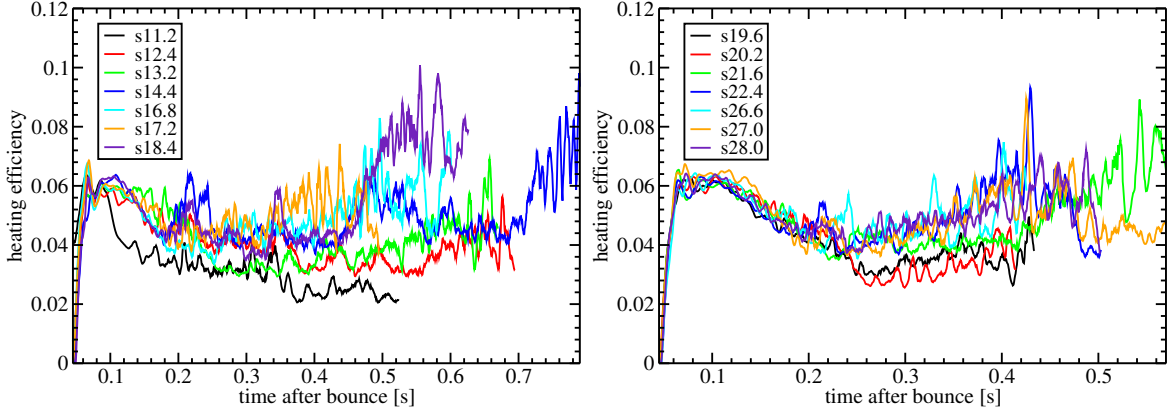


Figure 3.9: Time evolution of the heating efficiency $\dot{Q}_{\text{heat}}/(L_{\nu_e} + L_{\bar{\nu}_e})$ computed as the ratio of the neutrino heating rate and the sum of the electron-neutrino and electron-antineutrino luminosities for models with lower ZAMS mass (left panel) and with higher ZAMS mass (right panel). Note that the curves have been smoothed using a running average over 5 ms.

reflected in these diagnostic quantities. While the heating timescale continuously decreases with time, the advection timescale increases significantly at the arrival of the boundary between the silicon shell and the oxygen-enriched silicon shell, especially for heavier models. At this point, they experience a strong decrease of the mass accretion rate and thus, the longer advection timescale allows matter to stay much longer in the gain layer as before the arrival of the interface. The postshock flow is much longer heated to gain enough power to drive the shock outwards. This effect is strongest for models with a very strong interface (“s19.6”, “s20.2”, and “s26.6”), which start to explode relatively shortly after the arrival of the interface. Having a much weaker interface, models “s21.6” and “s28.0”, experience a very long delay until the onset of the explosion displayed by a strong rise of the advection timescale and thus, the ratio of advection to heating timescale (Figure 3.8). This fact suggests that it is not the reduction of the mass accretion rate at the infall of the Si/SiO interface that triggers directly the explosion, but that instead growing hydrodynamic instabilities discussed later in Section 3.5 must be responsible to trigger the late-time rise of $\tau_{\text{adv}}/\tau_{\text{heat}}$ along neutrino heating.

The advection timescale of low mass models (“s12.4”, “s13.2”, “s14.4”, and also “s18.4”) decreases continuously until it stabilizes at a level of about 5 ms. This decrease is connected to the shrinking mass contained in the gain layer. Nevertheless, these models still explode at very late times after bounce. One reason is the increasing neutrino heating rate \dot{Q}_{heat} and the corresponding increase in the neutrino heating efficiency (Figure 3.9) defined as the ratio of the total energy deposition rate to the sum of the radiated ν_e and $\bar{\nu}_e$ luminosities:

$$\eta = \dot{Q}_{\text{heat}} / (L_{\nu_e} + L_{\bar{\nu}_e}) . \quad (3.8)$$

According to Janka (2001, 2012) the neutrino energy deposition in the gain layer can be estimated as

$$\dot{Q}_{\text{heat}} \sim \frac{L_{\nu_e} \langle E_{\nu_e} \rangle^2}{r_{\text{gain}}^2} M_{\text{gain}} , \quad (3.9)$$

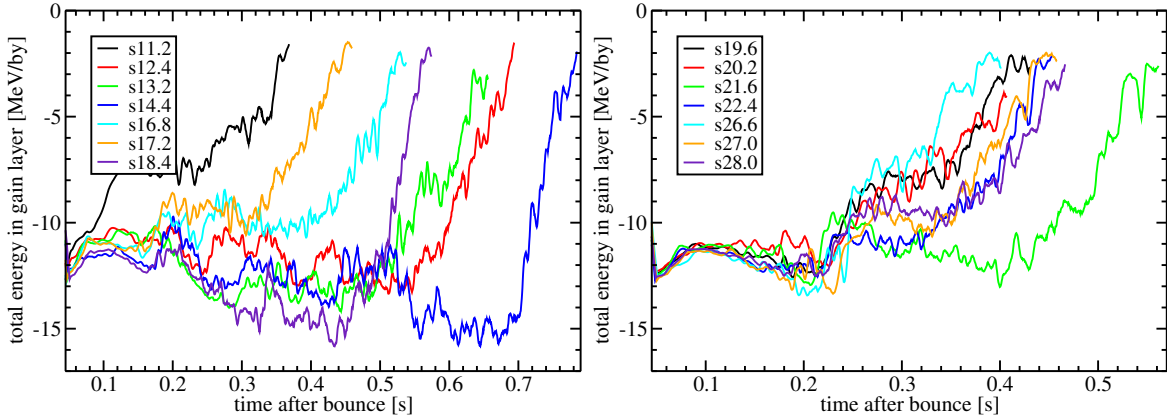


Figure 3.10: Time evolution of the total energy in the gain layer for models with lower ZAMS mass (left panel) and with higher ZAMS mass (right panel). Note that the curves have been smoothed using a running average over 5 ms.

and thus the heating efficiency η is proportional to

$$\eta \sim \frac{\langle E_{\nu_e} \rangle^2}{r_{\text{gain}}^2} M_{\text{gain}} . \quad (3.10)$$

The heating efficiency is the only quantity that increases systematically even before the explosion because of the slowly growing mass of the gain layer and the continuously increasing mean energies of the neutrinos radiated away (Figure 3.6) overcompensating the slow decline of the accretion luminosity (Figure 3.5) according to Equation 3.10 (Marek & Janka 2009; Müller et al. 2012b). For example, the heating efficiency of the late exploding models “s13.2” and “s21.6” rises already significantly before the shock expansion starts from about 3% and 4% at 300 ms to final values of 4% and 7%, respectively, at around 500 ms. Thus, at late times, a larger fraction of the energy radiated by neutrinos can be deposited in the gain layer and consequently heat the postshock flow more efficiently.

Around the onset of the explosion the advection timescale increases steeply. Higher pressures in the gain layer are responsible to transport more and more mass from deeper layer of the gain region outwards until a dominant fraction of the mass in the gain layer begins to move outward (Figure 3.7). The shock can expand sufficiently to create a positive feedback loop by further increasing τ_{adv} . Once the critical condition of $\tau_{\text{adv}}/\tau_{\text{heat}} \gtrsim 1$ is reached (Figure 3.8), a runaway situation is established with continuous shock expansion. The total energy in the gain layer depicted in Figure 3.10 is lifted towards positive values with the growing accumulation of mass in the gain layer indicating that the postshock material gets unbound. Note that Fernández (2012) demonstrated that transition finally occurs when the fluid in the gain region reaches positive specific energy. The timescale ratio criteria $\tau_{\text{adv}}/\tau_{\text{heat}} \gtrsim 1$ is already reached when the total energy in the gain layer just starts to rise towards positive while it is still negative (compare Figure 3.8 and Figure 3.10). At the beginning of the runaway shock expansion, only a small fraction of the fluid in the gain layer is rising, while the most part of the gain layer is following behind afterwards (see also Section 3.5). The binding energy is only positive, when the whole gain layer is expanding. For our models, the concept of the $\tau_{\text{adv}}/\tau_{\text{heat}}$ ratio is a viable criterion for the evolution of the exploding models.

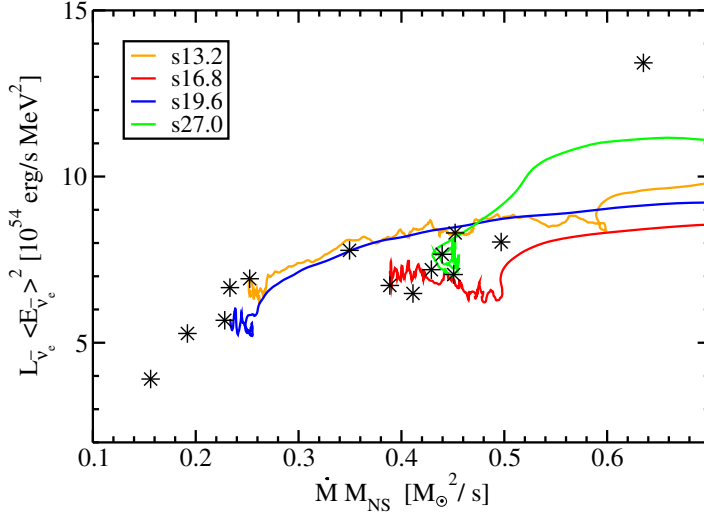


Figure 3.11: Critical curve for the electron-antineutrino luminosity times the squared mean energy ($L_{\bar{\nu}_e} \times \langle E_{\bar{\nu}_e} \rangle^2$) versus mass accretion rate times neutron star mass ($\dot{M} \times M_{\text{NS}}$) based on the explosion parameters (depicted by stars) of the fourteen investigated presupernova models of Woosley et al. (2002). For each model the the exact quantities are extracted at the onset of explosion. Additionally, the time-dependent relation between $L_{\bar{\nu}_e} \times \langle E_{\bar{\nu}_e} \rangle^2$ and $\dot{M} \times M_{\text{NS}}$ is shown for four selected simulations. The trajectories of $L_{\bar{\nu}_e} \times \langle E_{\bar{\nu}_e} \rangle^2$ are evolving from left to right towards the critical curve depicted by the stars.

3.4 The Concept of a Critical Curve

We have already mentioned that for a certain mass infall rate onto the accretion shock steady-state solutions cannot exist, once the neutrino luminosity exceeds a critical threshold value and thus neutrino heating is sufficiently strong. Such a critical condition separates exploding from nonexploding models and has been identified by Burrows & Goshy (1993) based on steady-state solutions of neutrino-heated and cooled accretion flows between the stalled shock and the proto-neutron star surface. In terms of this condition, either the driving neutrino luminosity must be sufficiently high to overcome the infalling mass on the stalled shock or the damping mass accretion rate must be low enough to launch a successful explosion. Thus, according to Burrows & Goshy (1993) the critical condition $L_{\nu}(\dot{M})$ defines a curve separating the region above, where neutrino heating is strong enough to push the stalled shock outward and trigger an explosion, from the region below, where steady-state accretion solutions can exist.

Performing an extensive parameter study, Murphy & Burrows (2008) investigated the concept of a critical condition with time-dependent hydrodynamic simulations. Applying parametrized, local neutrino heating and cooling terms, they followed the postbounce evolution for different, fixed values of the driving neutrino luminosity. Since the mass accretion rate decreases with time according to the characteristic density profile of the initial structure of the investigated progenitor (see Figure 3.2 for the model set presented here), in this parametrized approach each simulation determines the critical value of the mass accretion rate \dot{M}_{exp} at which the explosion becomes possible for the specific employed value of the neutrino luminosity L_{ν} . By systematically varying the driving neutrino luminosity L_{ν} , one samples pairs of the critical

values $(\dot{M}_{\text{exp}}, L_{\nu})$ defining a critical curve $L_{\nu}(\dot{M})$. By the means of their simulations set, Murphy & Burrows (2008) confirmed the existence of a critical condition separating explosion from accretion. Their 1D results verified the critical curve of Burrows & Goshy (1993) obtained by steady state solutions, while the corresponding 2D results showed that the critical luminosity is generally lowered $\sim 30\%$ in 2D compared to 1D in their considered highly idealized setup. Nordhaus et al. (2010) extended the investigations of Murphy & Burrows (2008) by including 3D runs and found a further reduction of the critical luminosity by 15–25% compared to the 2D case. Following the approach of Murphy & Burrows (2008) and Nordhaus et al. (2010) and thus applying parametrized, local neutrino heating and cooling terms, in Hanke et al. (2012) we performed hydrodynamic simulations in one, two, and three dimensions to prove the results of the previous investigations. While we observe a similar reduction of the threshold luminosity value of the 2D simulations in Hanke et al. (2012), we do not find any further decrease in our 3D models in the framework of this simple, parametrized neutrino description. Further studies (Burrows et al. 2012; Dolence et al. 2013; Couch 2013) have investigated the concept of a critical condition for shock revival to determine the effect of three-dimensional fluid dynamics on the postbounce dynamics. Although details are different, these works confirmed the results of our simplified 3D study of Hanke et al. (2012).

However, one has to be cautious to interpret the outcome of these investigations, since it has not been finally shown that the simple concept of a critical threshold condition separating explosions from continuous shock stagnation is applicable beyond the highly idealized setups applied in the aforementioned studies. None of them has properly taken into account the complex feedback between hydrodynamics and neutrino transport effects. By adopting a fixed driving neutrino luminosity and assuming a constant neutrino mean energy, feedback effects of the hydrodynamics on the neutrino emission are ignored, for example the proper time evolution of the neutrino luminosities and mean energies and the lack of the appropriate contraction of the neutron star due to lasting neutrino emission.

In this subsection, we aim to investigate if the concept of a critical condition can be applied to our fully self-consistent 2D model set, thus overcoming the limitation of a simplified, parametrized setup. However, to answer this question, a simple relation of the mass accretion rate at which the explosion becomes possible to the driving neutrino luminosity is not sufficient to take into account properly the hydrodynamic postbounce evolution of the supernova core. In contrast to the simplified studies, instead of assuming a fixed neutrino temperature, the neutrino mean energies are increasing by time (Figure 3.6) making neutrino heating more efficient (see Section 3.3), while the neutrino luminosities are decreasing by time (Figure 3.5).

Although we give in Table 3.1 the critical values of the electron neutrino luminosity L_{exp} and the mass accretion rate \dot{M}_{exp} at the time of the explosion sets in (measured as the point of time, when the ratio of the advection to heating timescale exceeds one), we derive now a more suitable relation between the critical neutrino luminosity and the corresponding mass accretion rate. Applying scaling relations to the advection and heating timescale introduced in the previous section, we will estimate the critical luminosity.

At first, according to Janka (2012), we apply the following scaling relation for the advection

timescale (Equation 3.2):

$$\tau_{\text{adv}} = \int_{R_g < r < R_s} \frac{1}{|\langle v_r \rangle|} dr \sim \frac{R_s}{v_{\text{pre-shock}}} \sim \frac{R_s^{3/2}}{\sqrt{M_{\text{NS}}}}. \quad (3.11)$$

Here, the average postshock velocity $|\langle v_r \rangle|$ is estimated as a large fraction of the pre-shock velocity $v_{\text{pre-shock}}$ just in front of the shock, which states (Janka 2001):

$$v_{\text{pre-shock}} = -\alpha \sqrt{\frac{2GM_{\text{NS}}}{R_s}}, \quad (3.12)$$

with $\alpha \sim 1/\sqrt{2}$ (Bethe 1990, 1993; Bruenn 1993). In Equation 3.11, the shock radius R_s itself can be expressed in terms of the electron antineutrino luminosity $L_{\bar{\nu}_e}$ and mean energy $\langle E_{\bar{\nu}_e} \rangle$ (Janka 2012):

$$R_s \sim \frac{\left(L_{\bar{\nu}_e} \langle E_{\bar{\nu}_e} \rangle^2 \right)^{4/9} R_g^{16/9}}{\dot{M}^{2/3} M_{\text{NS}}^{1/3}}. \quad (3.13)$$

On the other hand, applying the scaling relation Equation 3.9 and assuming a time-independent specific binding energy in the gain layer, the heating timescale (Equation 3.2) fulfills the following dependencies:

$$\tau_{\text{heat}} = \frac{E_{\text{bind}}}{\dot{Q}_{\text{heat}}} \sim \frac{R_g^2}{L_{\bar{\nu}_e} \langle E_{\bar{\nu}_e} \rangle^2}. \quad (3.14)$$

The critical condition for the runaway of the shock can then be formulated by setting both timescales equal and thus, applying the scaling relations (3.11) and (3.14) together with Equation 3.13 leads to:

$$L_{\bar{\nu}_e} \langle E_{\bar{\nu}_e} \rangle^2 \sim \left(\dot{M} M_{\text{NS}} \right)^{3/5} R_g^{-2/5}. \quad (3.15)$$

This relation defines a critical curve for $L_{\bar{\nu}_e} \langle E_{\bar{\nu}_e} \rangle^2$ as function of the product of the mass accretion rate and the mass of the neutron star $\dot{M} M_{\text{NS}}$. Equation 3.15 displays properly the dependence of the critical curve on the time-dependent neutrino luminosity and mean energy and the feedback effects of the hydrodynamics on the neutrino evolution.

Figure 3.11 depicts for each single model run the respective value pair $(L_{\bar{\nu}_e} \times \langle E_{\bar{\nu}_e} \rangle^2, \dot{M} \times M_{\text{NS}})$ at the time of the onset of the explosion indicating the specific critical condition for runaway. At first glance these stars can be collected to a critical curve $L_{\bar{\nu}_e} \times \langle E_{\bar{\nu}_e} \rangle^2$ ($\dot{M} \times M_{\text{NS}}$) although each individual model run depends on a specific density profile of the respective progenitor star and thus cannot be compared to each other in principle. Indeed, Figure 3.11 demonstrates that a critical condition for explosion can be formulated for our self-consistent model set. In the context of a critical curve, model “s18.4” is a particular case as mentioned in Section 3.2. It fulfills the criteria for runaway already at a very high mass accretion rate of $0.342 M_{\odot}/\text{s}$ (Table 3.1) since a high accretion part of the neutrino luminosity is induced and thus neutrino heating is sufficient strong to overcome the relative high damping mass infall on the shock. This model represents the outlier on the top right side of Figure 3.11 and demonstrates that there is a steep rise of the critical curve depicted by the critical pairs of each model below $0.342 M_{\odot} \text{s}^{-1}$ (to compare to the values depicted in Figure 3.11 multiply with the corresponding neutron star masses denoted in Table 3.1). This is a noticeable difference to

the principal results of a simple power-law of Burrows & Goshy (1993), who assumed steady-state conditions of the hydrodynamic postshock flow and neglected an accretion contribution to the neutrino luminosity. Applying realistic progenitor structure profiles, we found in Hanke et al. (2012) analogously to Couch (2013) a similar steep rise of the critical curve, although we argued that this feature is linked to the specific employed analytic description of neutrino effects.

The critical curve depicted by the stars in Figure 3.11 separates the region above for explosions and the region below, where still steady-state accretion solutions can be maintained by the hydrodynamics conditions in the postshock layer. Performing our hydrodynamic simulations we track the post-bounce evolution of each individual collapsing star and depict four trajectories of representative models in the $(L_{\bar{\nu}_e} \times \langle E_{\bar{\nu}_e} \rangle^2) - (\dot{M} \times M_{\text{NS}})$ plane of Figure 3.11. Since the mass accretion rate decreases with time according to the density profile that is characteristic of the initial progenitor structure (Figure 3.4, although M_{NS} is slowly increasing by time), a trajectory evolves from right to left on the horizontal axis of Figure 3.11 until $(M \times M_{\text{NS}})$ reaches the critical value depicted by a star and the model develops an explosion. Indeed, such a trajectory of our models is always below or right of the critical curve and thus, there is a steady-state solution for the hydrostatic configuration of a model prior to the explosion sets in. The illustration of such time-dependent trajectories that are representing the hydrodynamic evolution of a simulation run fully confirms the concept of a critical condition and a critical curve that is separating explosion from ongoing accretion even for self-consistent models with proper neutrino transport and feedback of the hydrodynamics on the neutrino evolution.

3.5 Driver of the Explosion, the Growth of Instabilities

After discussing the critical condition we aim to answer the question what is actually making the postshock layer unstable and allows a runaway situation to be established. Non-radial fluid mass motions are crucial to push the shock farther out increasing the time matter can stay in the gain layer. Both, convection and the SASI, increase the energy deposition of neutrinos sufficiently to finally revive the stalled shock. In this section, we investigate the growth conditions of both hydrodynamic instabilities in dependence of the respective progenitor model.

Typically, the high mass-accretion rate of individual supernova models (Figure 3.4) leads to very small shock radii, which stabilizes at very small radii of up to ~ 80 km (Figure 3.3). In consequence, the advection timescale is reduced significantly (Figure 3.7, middle panel), since it scales with the shock radius roughly with $\tau_{\text{adv}} \equiv R_s^{3/2}$ (see Equation 3.11 and cf. Scheck et al. 2008). As shown by Foglizzo et al. (2006), the linear growth rate ω_{SASI} of the advective-acoustic cycle amplifying the SASI growth is given in terms of the cycle efficiency Q and the duration τ_{cyc} of the cycle by

$$\omega_{\text{SASI}} = \frac{\ln |Q|}{\tau_{\text{cyc}}}. \quad (3.16)$$

Consequently, as argued by Müller et al. (2012a), the duration of an advective-acoustic cycle τ_{cyc} is short for a small shock stagnation radius and thus short advection timescale. Hence,

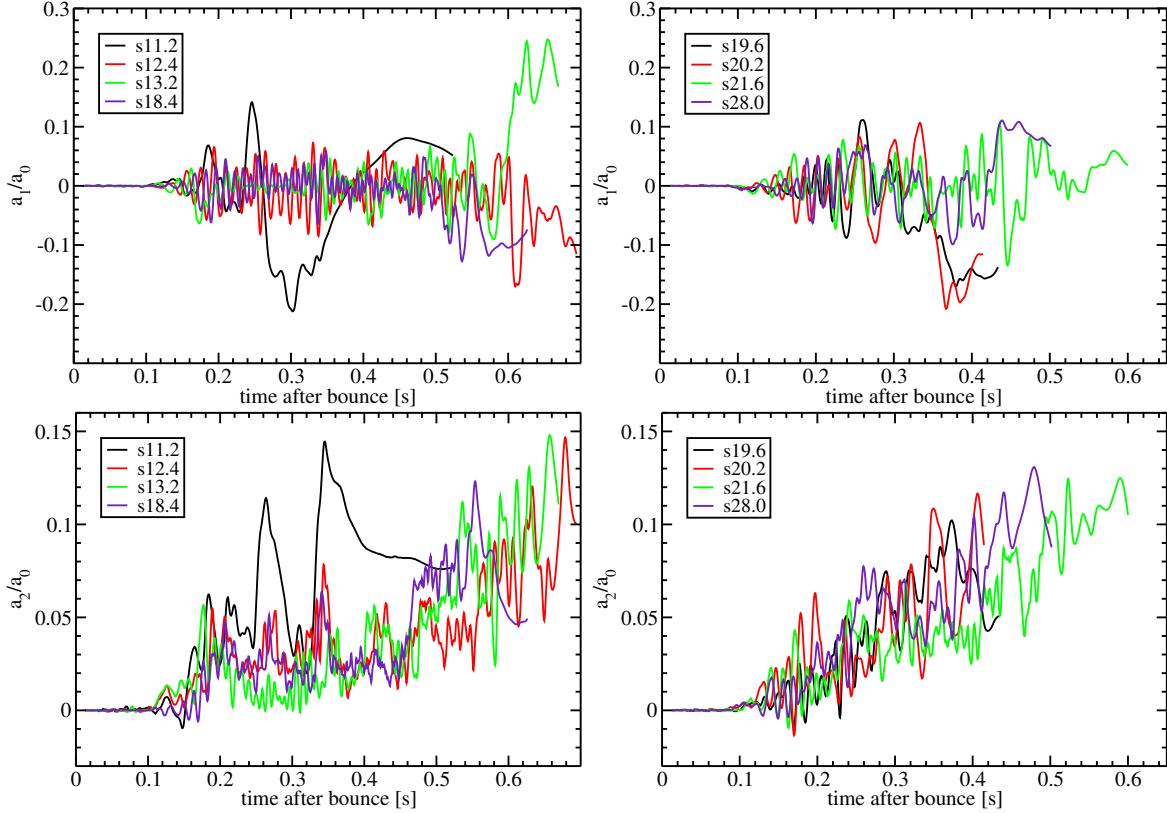


Figure 3.12: Time evolution of the coefficients of the spherical harmonics expansion of the shock surface for selected models with lower ZAMS mass (left panel) and with higher ZAMS mass (right panel). The top panels show the coefficient of the dipole a_1 and the bottom panels the coefficient of the quadrupole a_2 normalized to the amplitude of the $\ell = 0$ mode (i.e. the shock radius). Note that the curves have been smoothed using a running average over 5 ms.

for our set of simulation runs with a typical short advection timescale we can expect favorable conditions for an effective SASI growth.

For quantifying this more verbal argumentation by a detailed analysis, we perform a decomposition of the angular-dependent shock surface $R_s(\theta)$ into Legendre polynomials $P_l(\cos \theta)$. The expansion coefficients a_l are given by (see e.g. Müller et al. 2012b,a)

$$a_l = \frac{1}{2} \int_0^\pi R_s(\theta) P_l(\cos \theta) d(\cos \theta). \quad (3.17)$$

The coefficients a_l are the 2D counterpart of the corresponding 3D formulas applied in Section 5.2.

The time evolution of the a_1 coefficient of the dipole mode is depicted in Figure 3.12 (upper panels) for several selected models and indicates that at $t \sim 120$ ms sloshing motions of the shock surface start to grow with a relative small growth rate, when the postshock flow becomes aspherical as indicated by the increase of the lateral kinetic energies in Figure 3.13

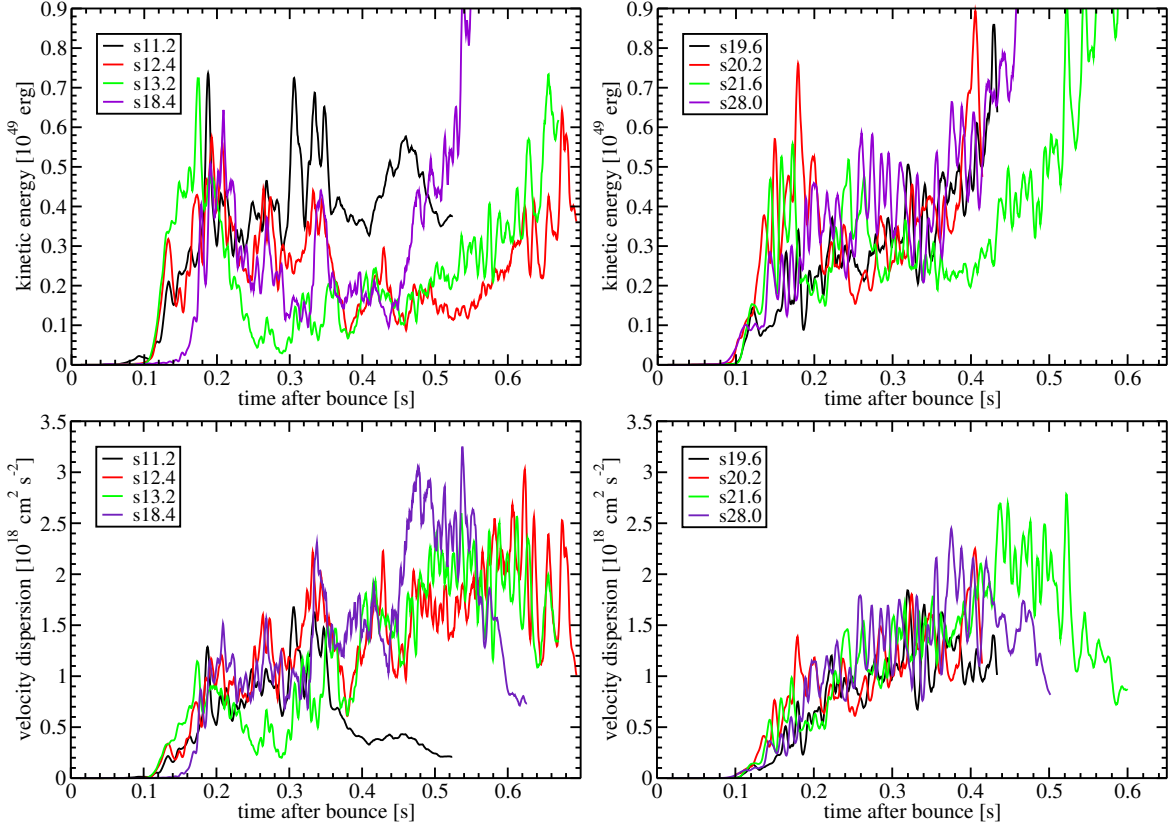


Figure 3.13: Kinetic energy of lateral mass motions $E_{\text{kin},\theta}$ (top) and the velocity dispersion $\langle v_\theta^2 \rangle$ (bottom) in the gain layer as function of time after bounce for selected models with lower ZAMS mass (left panel) and with higher ZAMS mass (right panel). Both quantities are a possible measure for the combined activity of convection and SASI. The velocity dispersion $\langle v_\theta^2 \rangle$ in the gain region, which is related to the lateral kinetic energy $E_{\text{kin},\theta}$ by the relation $\langle v_\theta^2 \rangle = 2E_{\text{kin},\theta}/M_{\text{gain}}$, provides a direct measure for the typical measure for the typical velocities of convective and SASI motions, while the lateral kinetic energy depends also on the mass contained in the gain region. Note that the curves have been smoothed using a running average over 5 ms.

(upper panels). All models experience strong quasi-periodic shock oscillations with a short oscillation period. At around $t \sim 220$ ms, i.e. when the Si/Si₀ shell interface has reached the shock and the accretion shock has dropped considerably for models with higher ZAMS mass, the SASI oscillation period increases with the longer advection timescale while the advective-acoustic cycle operates (Foglizzo et al. 2007; Scheck et al. 2008; Guilet & Foglizzo 2012). The models maintain large shock oscillations although they are less regular when the shock expands. Similar behavior can be observed for the other lighter progenitor models, which can maintain short shock oscillations over several hundred of milliseconds until the shock motion reaches the nonlinear regime with its non-oscillatory behavior and larger SASI amplitudes, when the shock expansion sets in.

The time evolution of the quadrupole mode depicted by the a_2 SASI coefficient in Figure 3.12 (bottom panels) is noticeable. Shortly before shock revival all models develop a strong (prolate) quadrupole deformation of the shock. For the more massive models with faster explosions

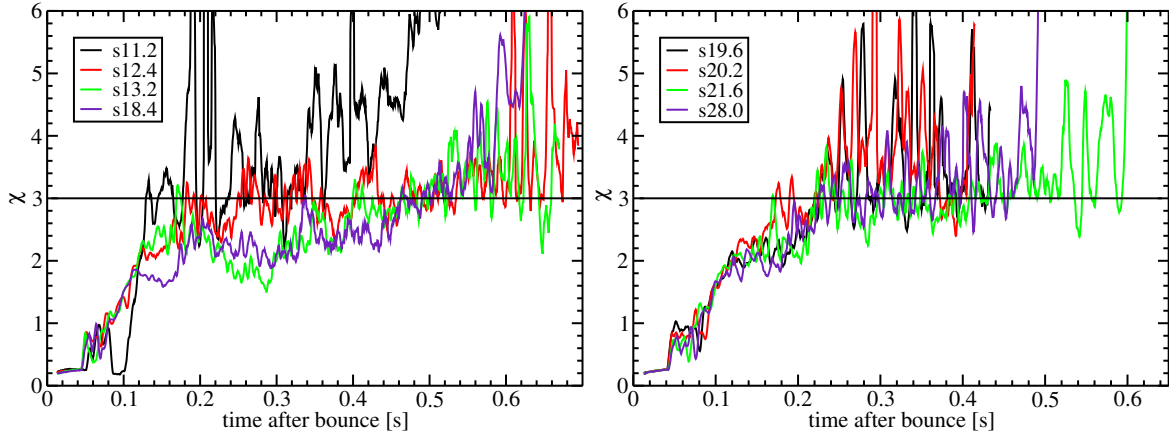


Figure 3.14: Time evolution of the growth parameter χ for selected models with lower ZAMS mass (left panel) and with higher ZAMS mass (right panel). The threshold value of $\chi \approx 3$ is reached at first for the 11.2 solar-mass progenitor at about 120 ms after bounce, while all heavier stars reach the criteria for convective instability at around 220 ms. Note that the curves have been smoothed using a running average over 5 ms.

the a_2 SASI coefficient continuously grows to larger and larger positive values directly from the onset of SASI growth at $t \sim 120$ ms, while the strong increase of the quadrupole mode sets in at around $t \sim 450$ ms after bounce for the very late exploding lighter simulation runs. The development of a strong quadrupole mode for all exploding models is a strong hint that the runaway expansion of the shock is obviously facilitated by the artificial symmetry axis. Thus, the strong quadrupole deformation of the shock surface enables the postshock layer to be pushed more and more outwards along the symmetry axis towards one direction periodically, while most of the matter behind the shock is still at rest.

The SASI instability with its high growth rates for the dipole and quadrupole modes (Figure 3.12) lead to large-amplitude bipolar shock oscillations pushing the shock outwards to larger radii step by step. In consequence, the dwelling time of the hydrodynamic fluid behind the shock grows, since it scales with the shock radius roughly with $\tau_{\text{adv}} \equiv R_s^{3/2}$ (see Equation 3.11 and cf. Scheck et al. 2008) and thus, the accreted material is exposed longer to neutrino heating in the gain layer. Finally, by continuous SASI shock oscillations the shock can be driven outwards sufficiently to create a positive feedback loop by further increasing the advection timescale of the matter in the gain layer until an explosion with continuous shock expansion is induced (see the discussion in Section 3.3 and in Marek & Janka 2009; Müller et al. 2012b).

Moreover, the supportive role of the SASI for reviving the stalled shock manifests in large supersonic lateral velocities in the postshock flow induced by continuous phases of large-amplitude shock expansion and contraction. Depicted in Figure 3.13 (top panels) the kinetic energy of non-radial mass motions $E_{\text{kin},\theta}$ shows quasi-periodic variations with spiky maxima and minima, which are typical for the presence of low-order SASI modes as pointed out by Hanke et al. (2012). In their parametric study a successful explosion is triggered, especially for models at the explosion threshold, by large-scale mass flows as associated with strong SASI activity. Here, as reflected by growing fluctuations of the angular kinetic energies the onset of explosion in our self-consistent models is facilitated in a similar manner.

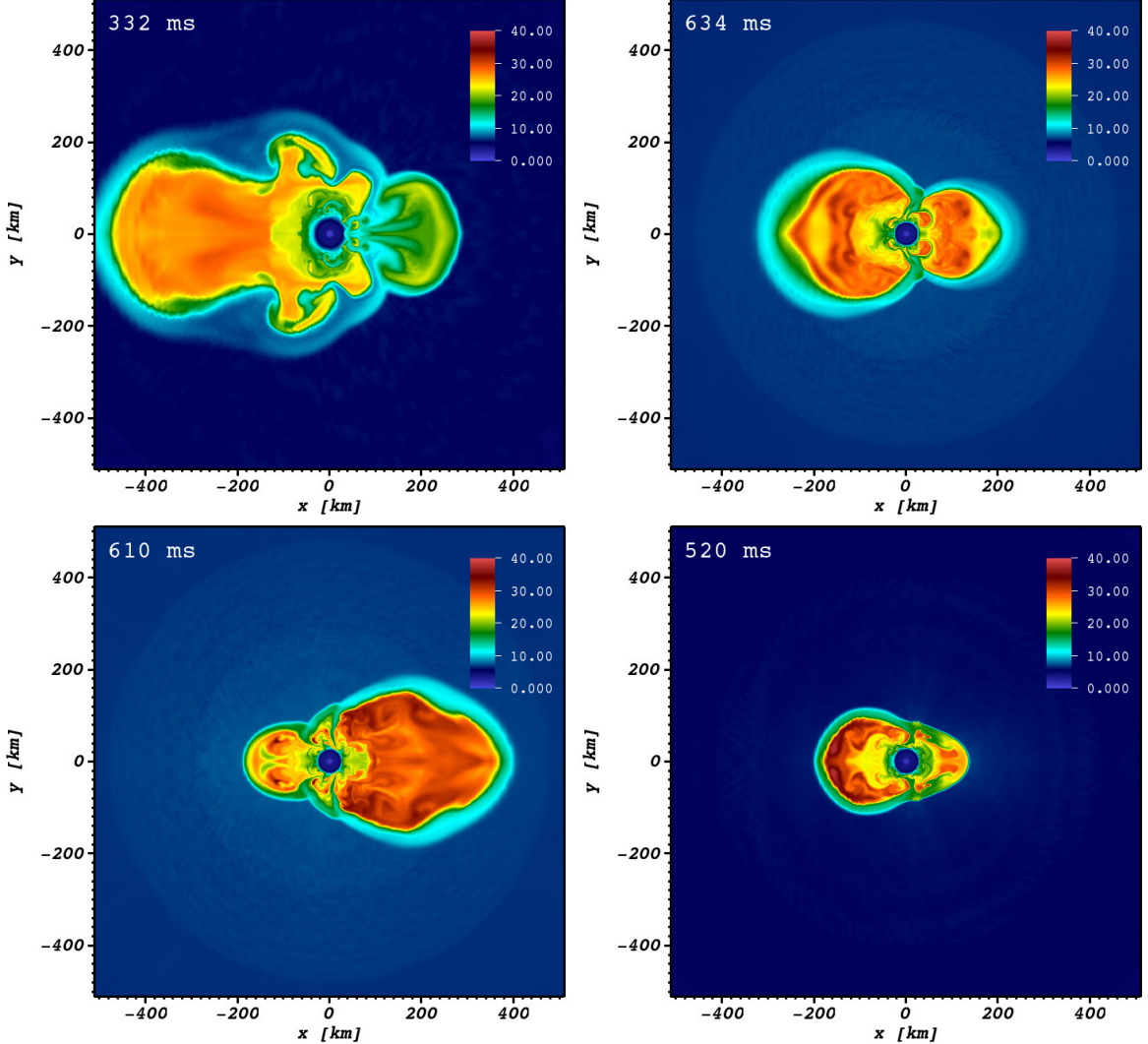


Figure 3.15: Snapshots of selected models with lower ZAMS mass (s11.2, s12.4, s13.2, and s18.4, from top left to bottom right) depicting the entropy per baryon s at the respective time of explosion.

The velocity dispersion $\langle v_\theta^2 \rangle$ in the gain region, which is related to the lateral kinetic energy $E_{\text{kin},\theta}$ by the relation $\langle v_\theta^2 \rangle = 2E_{\text{kin},\theta}/M_{\text{gain}}$, provides a direct measure for the typical measure for the typical velocities of convective and SASI motions, while the lateral kinetic energy depends also on the mass contained in the gain region. This quantity is continuously increasing by time for all models (Figure 3.13, bottom panels) indicating a growth of SASI and convective motions by time. Mainly, for the lighter models (left panel), the ongoing increase of the strength of non-radial mass motions is very supportive for the developing an explosion even several hundreds of milliseconds after bounce. According to Müller & Janka (2014) the lateral kinetic energy scales with

$$\frac{E_{\text{kin},\theta}}{M_{\text{gain}}} \sim \left(\frac{\dot{Q}_{\text{heat}}}{M_{\text{gain}}} \right)^{2/3}. \quad (3.18)$$

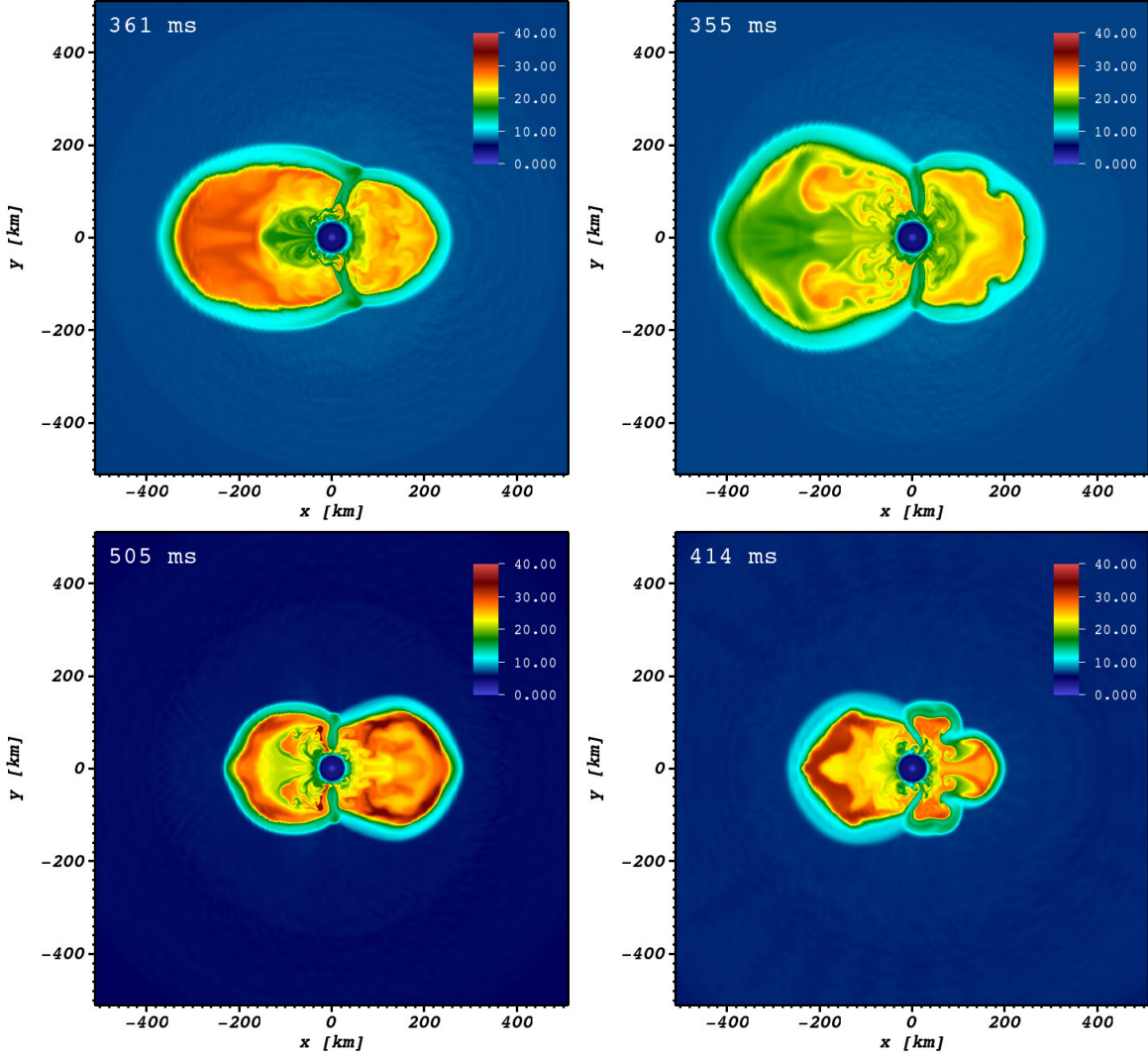


Figure 3.16: Snapshots of selected models with higher ZAMS mass (s19.6, s20.2, s21.6, and s28.0, from top left to bottom right) depicting the entropy per baryon s at the respective time of explosion.

As already argued in the discussion of the neutrino heating efficiency in Section 3.3 the ratio $\dot{Q}_{\text{heat}}/M_{\text{gain}}$ scales with $L_{\nu_e} \langle E_{\nu_e} \rangle^2$ (see Equation 3.9). Similar to the late time increase of the neutrino heating efficiency (Figure 3.9) the continuous increase of the neutrino mean energies depicted in Figure 3.6 is responsible for the increase of the velocity dispersion and thus, is fostering the growth of large-scale aspherical mass motions inducing the onset of the explosion. This trend may also be responsible for the late-time explosion reported in Marek & Janka (2009).

By trend, the situation of the hydrodynamic postshock flow in our simulation runs is favorable for the growth of the standing accretion-shock instability, since the other generic hydrodynamic instability in the supernova core, convection is suppressed in our models as observed in the full neutrino-hydrodynamic simulations by Marek & Janka (2009) and as pointed out by Scheck et al. (2008) performing parametric hydrodynamic studies of the post-bounce dynam-

ics. On the one hand the neutrino energy deposition in the gain layer of our simulations is too weak to generate a steep negative entropy gradient necessary for developing convection as can be seen by comparing the driving neutrino luminosities of our models (Figure 3.5) with the ones of exploding parametric models of Scheck et al. (2008) (see e.g. their Figure 18). On the other hand, the nuclear equation of state of Lattimer & Swesty (1991) with a nuclear incompressibility of 220 MeV employed in our simulations generates rather compact neutron stars (Steiner et al. 2010; Hebeler et al. 2010). Thus, the forming neutron star contracts rapidly from ~ 75 km to ~ 40 km in our sophisticated supernova model (for a recent comparison of different high-density nuclear equation of state in spherical supernova simulations see Steiner et al. 2013) and enforces the retraction of the shock radius, which scales directly with the radius of the neutron star according to Janka (2012). In consequence, the gas in the post-shock region is rapidly advected towards the gain region suppressing the growth of convective motions.

To quantify this argumentation and to determine the importance of convection in our models, Figure 3.14 displays the critical parameter χ for the growth of convection as evaluated from spherically averaged stellar quantities in the gain layer of selected, axisymmetric models with different preexplosion masses according to Equation (3) in Müller et al. (2012a),

$$\chi = \int_{\langle R_g \rangle}^{\langle R_s \rangle} \frac{\text{Im } \omega_{\text{BV}}}{|\langle v_r \rangle|} dr, \quad (3.19)$$

where ω_{BV} is the Brunt-Väisälä frequency. The integration is performed between the average gain radius $\langle R_g \rangle$ and the average shock radius $\langle R_s \rangle$. Note that only regions contribute to the integral where $\omega_{\text{BV}}^2 < 0$ indicates local instability. The parameter χ roughly measures the ratio between the advection timescale of the flow through the gain layer and the growth timescale of convection. Since perturbations are advected out of the gain layer with the accretion flow in a finite time, convection can develop only when perturbations are amplified sufficiently strongly within this time. For the linear regime (i.e., for small initial perturbations) Foglizzo et al. (2006) found the threshold condition of $\chi \gtrsim 3$ for convective activity to develop in the accretion flow of the gain layer. This result of mathematical analysis is supported by numerical studies in 2D by Buras et al. (2006b); Scheck et al. (2008); Fernández & Thompson (2009b,a).

While the SASI becomes active when aspherical mass motions start to develop at around $t \sim 120$ ms as indicated in Figure 3.13, the condition for convective instability remain sub-critical. Convection is damped because of the low neutrino-heating rate in our self-consistent models with the VERTEX-PROMETHEUS code and the short advection timescale as already discussed previously. The absence of convection may be supportive for the early development of SASI activity as argued by Müller et al. (2012a) for their $27M_\odot$ progenitor. Indicated by the critical parameter χ in Figure 3.14 (right panel) the threshold condition of $\chi \gtrsim 3$ for convective activity is reached for more massive models at around $t \sim 220$ ms, i.e. when the Si/Si0 shell interface has reached the shock and the accretion shock has dropped considerably for models with higher ZAMS mass. Because of the significant reduced mass accretion rate the shock expands to large radii and thus, the higher advection timescale increases the value of χ . For example, the relatively fast exploding models “s19.6” and “s20.2” show convective activity with a critical parameter well above $\chi \gtrsim 3$. On the other hand, we observe a very interesting trend of the critical parameter especially of the light models with 13.2, and

18.4 solar masses. While χ remains sub-critical for a long time, from around $t \sim 250$ ms the condition for convection becomes more and more favorable until at around $t \sim 500$ ms convective activity is fully established, when the timescale ratio $\tau_{\text{adv}}/\tau_{\text{heat}}$ exceeds unity (Figure 3.8) and shock expansion sets in (Figure 3.3). We can identify two reasons for the continuous development of convective activity for this models. The large-amplitude sloshing motions of the stalled shock induce lateral flow activity in the postshock region (Figure 3.13) and the development of fluid elements with very steep unstable entropy gradients (Marek & Janka 2009). Hence, the ongoing strong SASI shock motions can trigger secondary convective activity (Buras et al. 2006b; Scheck et al. 2008). Moreover, the continuous increase of the velocity dispersion depicted in Figure 3.13 (bottom panels) due to the more efficient neutrino energy deposition (Figure 3.9) is directly reflected in the increase of the critical parameter for convective activity.

While our models evolve similar to the model s27.0 of Müller et al. (2012a) classified as “SASI-dominated”, the interplay between convection and SASI around shock revival seems to be more complicated. In this fully nonlinear phase, it is hard to distinguish which hydrodynamic instability is primarily responsible for the postshock dynamics and ultimately powers the explosion. The dependence of the growth conditions of convection and SASI on the shock radius is opposite. Although the shock is pushed to large radii by large SASI sloshing motions, strong shock oscillations are maintained with a larger amplitude in our models and secondary convective activity supports the further shock expansion. To illustrate the hydrodynamic situation of the postshock flow around shock revival, in Figures 3.15 and 3.16 entropy color coded snapshots of the supernova core are depicted at the onset of the explosion determined as the moment the timescale ratio exceeds unity. The shock surface of all models develops clearly a prolate deformation by a large-amplitude bipolar SASI oscillation. Besides small buoyant bubbles growing behind the sloshing SASI motions of the shock surface large-scale, high-entropy bubbles are visible, which are triggered by the SASI shock expansion phases. As founded by Fernández et al. (2013) SASI-dominated models are characterized by the interplay of shock sloshing motions and the formation of large-scale, high-entropy structures. They conclude that once these bubbles are able to survive for several SASI oscillation periods a SASI-driven explosion develops. The dominance of a large-scale bubble seeded by the SASI shock sloshing over smaller-scale bubbles in our entropy color coded snapshots in Figures 3.15 and 3.16 let us suggest that our simulation runs are indeed SASI-dominated, while convection has a more supportive role.

3.6 Shock Expansion and Explosion Energy

After the driving hydrodynamic instabilities discussed in the previous section are creating a runaway situation, a continuous shock expansion sets in as indicated by the maximum shock radius in Figure 3.17. However, the simulation are stopped already shortly after the onset of the explosion because of the extremely computationally expensive neutrino transport. For most models we follow the maximum shock expansion up to ~ 1200 km and for models “s11.2” and “s27.0” up to ~ 2500 km.

The explosion energy is calculated by integrating over the gain region where the local binding energy E_{bind} as defined in Equation 3.6 is positive (see previous studies of Buras et al. 2006a;

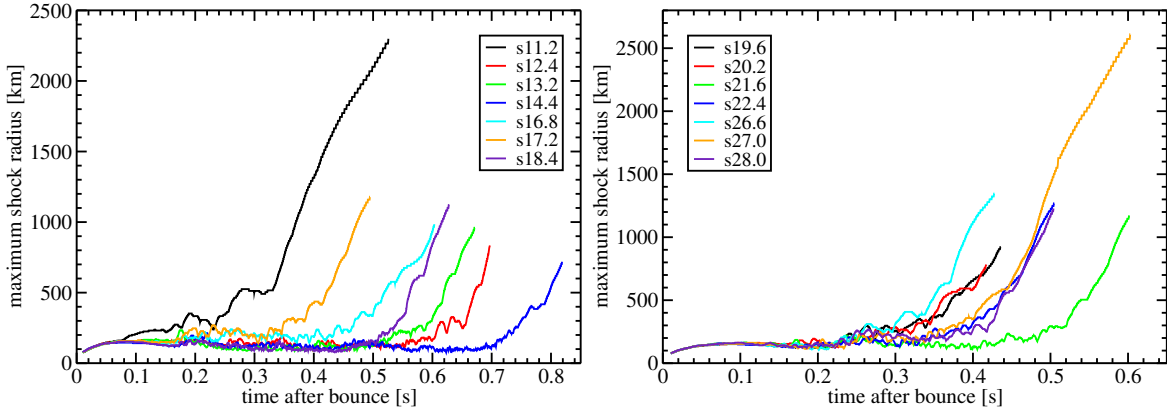


Figure 3.17: Trajectories of the maximum shock radius as function of time after bounce for models with lower ZAMS mass (left panel) and with higher ZAMS mass (right panel). The simulations have been stopped already shortly after the onset of explosion due to numerical difficulties.

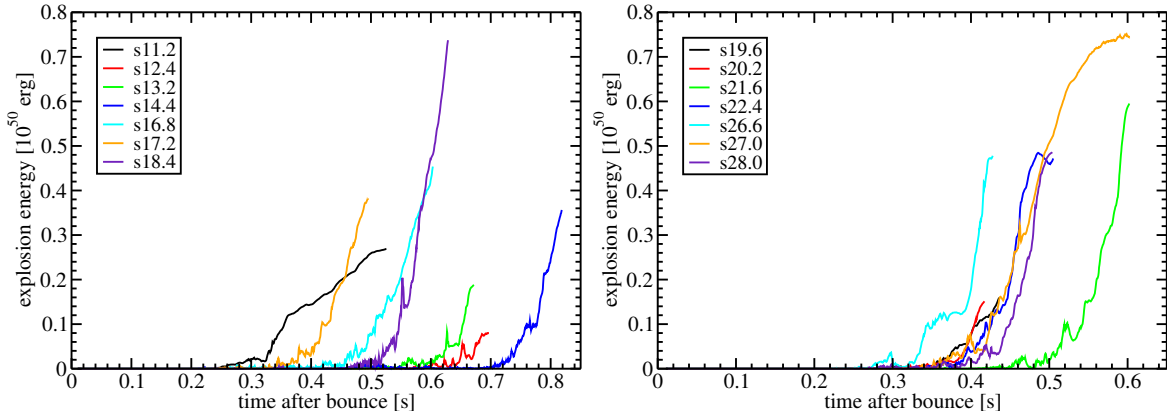


Figure 3.18: Diagnostic explosion energies for models with lower ZAMS mass (left panel) and with higher ZAMS mass (right panel). See the text for exact definition.

Marek & Janka 2009; Suwa et al. 2010; Müller et al. 2012b; Bruenn et al. 2013):

$$E_{\text{expl}} = \int_{E_{\text{bind}} > 0} E_{\text{bind}} dV. \quad (3.20)$$

The time evolution of the explosion energies of our models is depicted in Figure 3.18. First matter junks behind the shock become unbound typically at the onset of the explosion when the timescale ratio exceeds unity (Table 3.1). After the shock expands beyond ~ 400 km the temperature behind the shock front drop sufficiently for the recombination of nucleons to α -particles and consequently, the explosion energy starts to rise with a very steep gradient for most of our models. At the final post-bounce time our models reached, we observe explosion energies of up to $E_{\text{expl}} \sim 0.7 \times 10^{50}$ erg still increasing significantly e.g. with a rate of $\sim 11 \times 10^{50}$ erg s $^{-1}$ for model “s18.4”.

At this stage, therefore, a reliable determination of the final explosion energies is not possible. The simulations would have to be continued for several hundreds milliseconds more as demon-

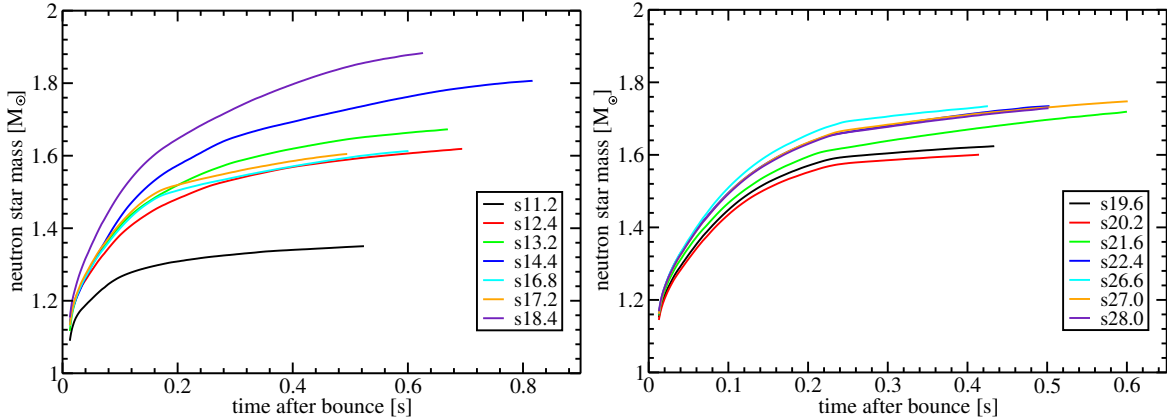


Figure 3.19: Time evolution of neutron star masses for models with lower ZAMS mass (left panel) and with higher ZAMS mass (right panel). Note that the curves have been smoothed using a running average over 5 ms.

strated by the neutrino-driven explosion models investigated by Scheck et al. (2006, 2008). Our sophisticated and self-consistent neutrino transport is such computationally challenging that it is still impossible to follow the postbounce dynamics into the postexplosion phase. Ongoing accreted matter is partially absorbing energy from neutrino in the gain layer and begins to rise again contributing to the budget of unbounded matter behind the outwards traveling shock. For this reason we expect that the final explosion energy of model “s18.4” is highest with its high rate of ongoing accretion of matter at the begin of the explosion (Figure 3.7). Furthermore, the continuous recombination of nucleons into α -particles (and further into heavy nuclei) behind the expanding shock front sets free energy for several hundred milliseconds. For a detailed discussion of possible final values of the explosion energies, which could finally be obtained with simulations employing the neutrino-hydrodynamics code VERTEX-PROMETHEUS, we refer to the respective arguments in Marek & Janka (2009) and Müller et al. (2012b). Although beyond this work, it is an interesting question, if as argued by Marek & Janka (2009) for their $15 M_{\odot}$ explosion model the explosion energies of our models can reach the canonical value of $E_{\text{expl}} \sim 1 \times 10^{51} \text{ erg} = 1\text{B}$ (e.g., Tanaka et al. 2009; Utrobin & Chugai 2011), for example the observed value of SN 1987A of $E_{87\text{A}} \sim 1.3 \times 10^{51} \text{ erg}$.

In the fast exploding models of Bruenn et al. (2013) (see next Section 3.7 for a comparisons of our models with this work) the explosion energies much stronger increasing energies compared to our models. Since their models are already starting to explode at 200 ms, there is much more matter in the gain layer, which can be heated by neutrinos and get unbound (see for comparison Figure 3.7 for our runs). For example, their simulation run of the 12 solar-mass case of Woosley & Heger (2007) converges at an explosion energy of 0.38B, which are consistent with observation for lower mass progenitors (Smartt 2009). This discrepancy between their models and ours remains to be investigated and is the most prominent difference.

The mass of the neutron star at the time the explosion sets in is given for each model in Table 3.1 and the time evolution of the neutron star mass for each simulation run is displayed in Figure 3.19. By trend, this quantity saturates faster than the diagnostic explosion energy and is thus more suitable for discussing general trends of the progenitor-explosion connection for our set of self-consistent simulations. Most of masses of the neutron star are converging in

the mass range between $1.6 M_{\odot}$ and $1.8 M_{\odot}$ for the employed equation of state of Lattimer & Swesty (1991) with a nuclear incompressibility of $K = 220$ MeV. However, the late exploding models “s14.4” and “s18.4” can maintain a high mass accretion rate (Figure 3.4) for a long time period resulting in a very heavy neutron star of $1.8 M_{\odot}$ and $1.9 M_{\odot}$ at the end of the simulation. There is no clear relationship between the mass of the neutron star M_{NS} and the ZAMS mass M_{ZAMS} of the respective preexplosion model. The final value M_{NS} is rather determined by the time matter can be accreted until the explosion sets in. In general, the distribution of our NS masses is comparable to one of Ugliano et al. (2012), which spans from $\sim 1.2 M_{\odot}$ and $\sim 2.0 M_{\odot}$. By trend, our values are somehow higher than typical values of comparable models by Ugliano et al. (2012) of $1.4\text{--}1.7 M_{\odot}$. That might be a consequence of the relative late onset of the explosions with its long duration of strong accretion of matter on the neutron star.

3.7 Investigation of Models based on the Presupernova Models of Woosley & Heger (2007)

Recently, Bruenn et al. (2013) have presented four selected axisymmetric self-consistent simulations based on the preexplosion models of Woosley & Heger (2007). Although their numerical treatment of neutrino transport within their CHIMERA code is almost as sophisticated as the VERTEX-PROMETHEUS code with differences in the exact neutrino solver and the specific implementation of neutrino rates, their models exhibit significant differences in the postbounce evolution and in shock revival. Thus, it is worth to perform these four additional models allowing a direct comparison of the outcome of simulation results obtained by different competing modeling groups. Most noticeable and surprisingly, all models of Bruenn et al. (2013) explode in a similar manner nearly independently of the specific progenitor structure exceeding the critical value for shock runaway at around 100 ms after core bounce. Based on these results one might hope that the presupernova models of Woosley & Heger (2007) enable faster explosions.

We have added these four additional models based on the progenitor models of Woosley & Heger (2007) spanning progenitors of $12\text{--}25$ solar masses in Table 3.1 summarizing important model parameters. As can be deduced by the given explosion times in Table 3.1 all of our models explode, although the runaway situation is established at completely different postbounce times and generally much later than the models of Bruenn et al. (2013). The exact shock trajectories of the four selected models of the Woosley & Heger (2007) presupernova series depicted in Figure 3.20 reflect the strong dependence on the according time evolution of the mass accretion rate (Figure 3.21). Confirming the observations in Section 3.2, both heavier models, “s20-2007” and “s25-2007”, with a steep drop of the mass accretion rate at $240 - 270$ ms, explode relatively quickly, while both other models, “s12-2007” and “s15-2007” with a continuous, but slow decrease of the mass accretion rate reach the conditions for shock runaway much later. The different time evolution of the models of Bruenn et al. (2013) and our runs might be a consequence of the different evolution of neutrino quantities, which we show in Figure 3.22, in the left column the different neutrino luminosities of the four simulation runs and in the right column the respective neutrino mean energies. However, the examination of the subtle differences in both neutrino transport solvers is difficult and

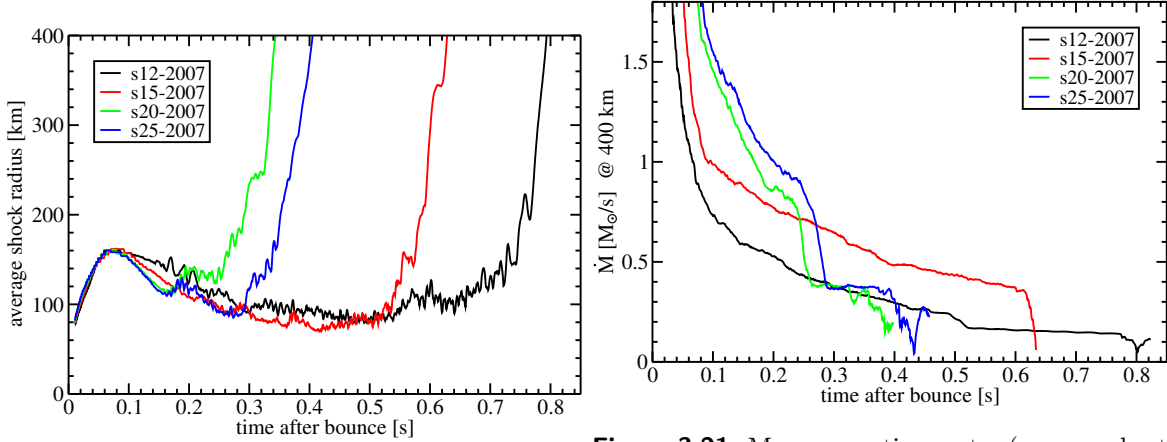


Figure 3.20: Average shock radius as function of time after bounce for the four investigated models based on the progenitors of Woosley & Heger (2007).

Figure 3.21: Mass accretion rate (measured at 400 km) as a function of time after bounce for the four investigated models based on the progenitors of Woosley & Heger (2007).

without a direct code comparison impossible.

The lightest investigated model “s12-2007” is ideally suited for a direct comparison between our results obtained with the VERTEX-PROMETHEUS code and the model “B12-WH07” of Bruenn et al. (2013) performed with their CHIMERA code, since Bruenn et al. (2013) provides several entropy color snapshots for this particular model. For this reason, we depict the time evolution of the entropy distribution in the supernova core in Figure 3.23 by several snapshots. At 90 ms (first panel) induced by neutrino heating first small convective structures are growing from the initially seed random perturbations. While in our model the strength of the convective plumes is relatively weak, the convective pattern in the model of Bruenn et al. (2013) is much more developed with a much more extended postshock region. At this point, the evolution of both models starts to diverge. While the shock retreats in our models due to the shrinking neutron star radius and insufficient neutrino heating (second 150 ms and third 200 ms panel), the shock surface of the Bruenn et al. (2013) model is now continuously expanding. Neutrino-driven convection and the SASI manifested in low-mode distortions of the shock is sufficient strong for fast shock revival. Instead, the postshock situation of our model turns into a several hundred milliseconds long-lasting period of strong sloshing motions of the shrinked, just ~ 100 km large shock surface characterized by low-mode asymmetries in the supernova core. These shock oscillations associated with the SASI are amplifying by time pushing the shock outwards and enlarging the gain region (compare the slightly growing shock radius in the fifth 400 ms and in sixth 600 ms panel) As discussed in Section 3.5 these SASI motions are responsible for shock revival in our models.

A detailed comparison both of the simulations results as well as the specific code setups is definitely needed to understand the exact differences of the outcome of the simulations performed with the CHIMERA code and with the VERTEX-PROMETHEUS code. Such a comparison would allow a better understanding of the missing ingredients in our models for a faster and more energetic shock revival as observed for the runs of Bruenn et al. (2013).

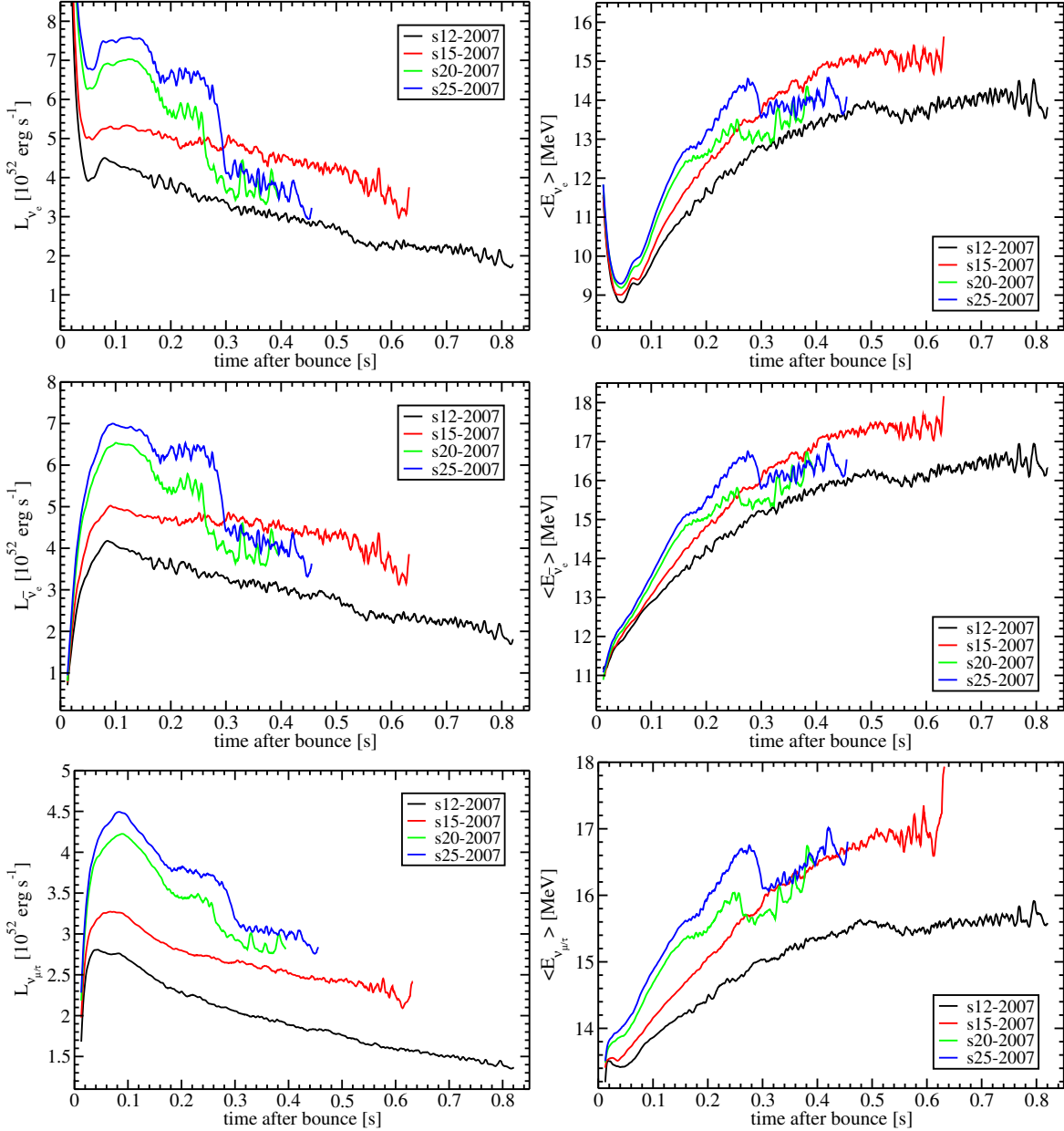


Figure 3.22: Neutrino luminosities (left panel) and neutrino mean energies (right panel) for the four investigated models based on the progenitors of Woosley & Heger (2007). The upper, middle, and lower panels indicate the luminosities for ν_e , $\bar{\nu}_e$, and $\nu_{\mu/\tau}$, respectively. Angular averaged quantities are extracted at a fiducial observer radius of 400 km. Note that the curves have been smoothed using a running average over 5 ms.

3.8 Summary of the Results based on our Axisymmetric Simulations

In this chapter, we have presented results of self-consistent axisymmetric core-collapse supernova simulations performed with the VERTEX-PROMETHEUS code for a wide range of massive

presupernova models in the mass range between 11 and 28 solar masses. For the first time, it has been possible to systematically investigate the progenitor dependence of the explosion mechanism by means of multi-dimensional simulations with full neutrino transport. To summarize, we can draw the following conclusions from our set of 2D simulations:

- We have obtained a large variety of successful core-collapse supernova explosions. Unexpectedly, all investigated models explode. These results are an important confirmation that the neutrino-driven supernova mechanism works at least in 2D along previous studies (Buras et al. 2006b; Marek & Janka 2009; Müller et al. 2012b,a; Bruenn et al. 2013; Suwa et al. 2010). We could significantly extend the set of progenitors which yield successful core-collapse supernova explosions.
- While systematically comparing our simulation runs, we have observed a strong dependence of the explosion characteristics on the specific progenitor structure. The investigated set of progenitors can be divided into two classes. One the one hand there are rather fast explosions, which start quickly after a steep drop of the mass accretion rate on the supernova shock connected to the arrival of a strong Si/SiO composition-shell interface and on the other hand models tend to explode late if their progenitor structure does not incorporate such a strong density jump.
- Our models yield rather weak and relatively late explosions such as the previous 2D studies with the VERTEX-PROMETHEUS (Buras et al. 2006b; Marek & Janka 2009) and the VERTEX-COCONUT (Müller et al. 2012b,a) simulation code. Although we could not run our simulations long enough to determine the exact final explosion energies, one can expect significantly lower values compared to observations and the results of Bruenn et al. (2013).
- As the neutron star shrinks quickly and thus, the stalled supernova shock front recedes by time, the advection timescale in our models is typically very small. Thus, the conditions for efficient SASI growth are favorable and the vivid SASI activity is observed in our models playing at least a supportive role for initial shock expansion.

However, the growth of large-scale motions of the supernova shock associated with the SASI could be an effect of the artificial symmetry axis. Will vigorous SASI activity develop in 3D as well? Could the development of low-order modes of the shock be inhibited because of the forward turbulent energy cascade in 3D (Hanke et al. 2012)? Will the $\ell = 1$ sloshing mode turn into a spiral mode when overcoming the artificial symmetry restriction (Blondin & Mezzacappa 2007; Fernández 2010)? Will the SASI amplitudes remain lower in 3D as suggested by Iwakami et al. (2009)? All these questions have to be answered for realistic conditions in self-consistent core-collapse supernova simulations in three dimensions. Urgently, the success of our simulation setup enforcing axisymmetry has to be confirmed by simulations without any symmetry restrictions.

Before moving onward to the discussion of our 3D neutrino-hydrodynamics simulations performed with the VERTEX-PROMETHEUS code, we turn now to a short intermediate chapter presenting further axisymmetric simulations. These models are intended to prove if and how the results of the simulations presented in this chapter are resolution independent. Furthermore, as a preparation for the 3D simulations, we will justify our slightly changed setup used for the 3D simulations presented later.

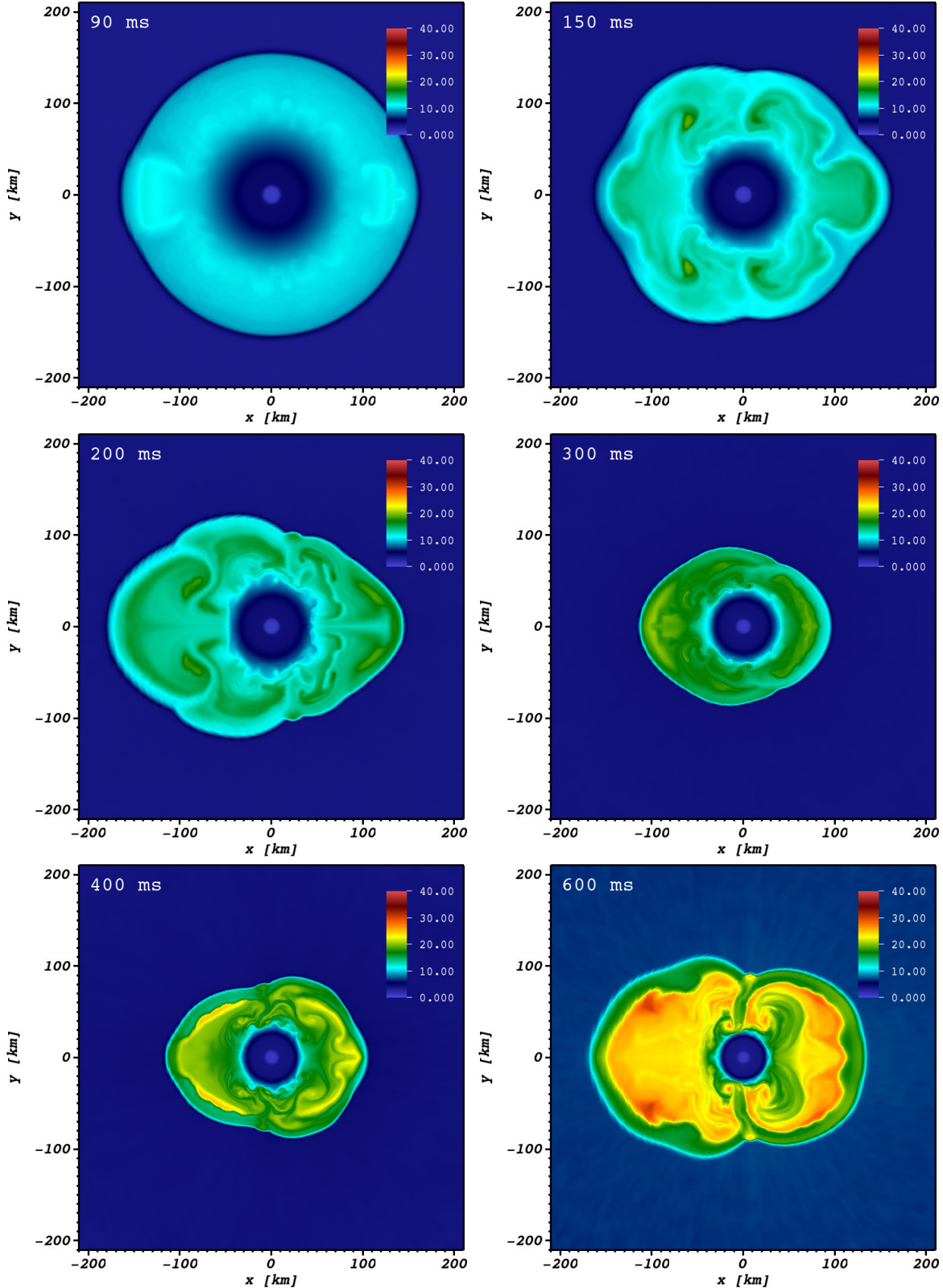


Figure 3.23: Snapshots of the evolution of model “s12-2007” depicting the entropy per baryon s at 90 ms, 150 ms, 200 ms, 300 ms, 400 ms, and 600 ms after bounce.

4 The Dependence of the Postbounce Evolution on the Grid Setup in Axisymmetry

In this chapter, we study how the numerical setup influences the postbounce evolution of our axisymmetric simulations presented so far. In doing so, we both complete the analysis of our 2D simulations and make the transition to our full 3D simulations, which will be discussed in the next chapters. Our numerical treatment of the explosion mechanism of core-collapse supernova has to be tested against resolution artifacts. While we have already performed such tests with simple neutrino source terms in Hanke et al. (2012), a small study with full neutrino transport is compulsive to determine the effect of changed grid resolution on our 2D models. Furthermore, we aim to justify the small changes of the numerical setup used for our 3D models, which were necessary to be able to perform the very first self-consistent three-dimensional simulations of core-collapse supernovae under the restrictions of currently available numerical and computational resources.

4.1 The Influence of Numerical Resolution

In Table 4.1, we summarize the different simulations used for our small resolution study. We employ three different angular resolutions of 2.05° (88 lateral zones), 1.41° (128 lateral zones, applied so far), and 0.70° (256 lateral zones), respectively. Additionally, the model with the best angular resolution is recomputed with an increased number of initially 600 instead of 400 radial zones. As mentioned in Section 3.1, the number of radial zones is increased from time to time by a numerical refine procedure to ensure a well resolved proto-neutronstar surface region, where the density gradient steepens with time. Other changed simulation parameters of model “s27 1dpot10km” will be discussed later in Section 4.2.

Although the same amplitude of perturbation of 0.1% in density is applied on the whole computational grid as explained in Section 3.1, a perturbation with different grids enforces arbitrary different wavenumbers of the initial perturbations structures zone by zone. Moreover, the time evolution of the postbounce dynamics for different simulations cannot be the same, since the hydrodynamic flow behind the supernova shock evolves highly non-linear and chaotic. However, it is very reassuring that the overall postbounce evolution of all three models with different angular resolution is very similar. The maximal as well as the average shock position depicted in Figure 4.1 lies more or less on top of each other for the differently angular resolved models. Even more promising, the runaway of the supernova shock at the onset of the explosion happens at exactly the same time. This nearly identical behaviour is reflected in the perfectly same evolution of the ratio of advection and heating timescale (Figure 4.3) indicating the readiness of an explosion. Furthermore, the similarity of the models

Model	1D Core	# Ang. zones	# Rad. zones	Grav. Pot.
s27 1dpot10km	10 km	88	400	1D
s27 normal128	1.7 km	128	400	2D
s27 normal256	1.7 km	256	400	2D
s27 normal256 600r	1.7 km	256	600	2D

Table 4.1: Summary of investigated axisymmetric models with different simulations setups based on the presupernova model with a ZAMS mass of 27.0 solar masses of Woosley et al. (2002). For each setup we give the employed size of the inner spherical core, the number of chosen latitudinal and radial zones, as well as the applied version of the gravitational potential solver.

is indicated by the time evolution of the expansion of the shock surface into spherical harmonics displayed in Figure 4.4. The growth of the SASI and the size of the amplitude of the oscillations evolve very similar, although the detailed oscillation pattern differs due to the differently imposed perturbations pattern for other resolved models. In the model with highest angular resolution “s27 normal256” the position of the shock is somewhat larger in the first two hundred milliseconds (Figure 4.1) also reflected in the slightly higher timescale ratio in Figure 4.3. Consequently, the total energy deposition in the gain layer by neutrinos is enlarged for this model as shown in Figure 4.5. Nevertheless, this model does not explode earlier.

The equivalent outcome of simulations with different angular resolutions strongly consolidates the conclusions made on the basis of the axisymmetric simulations presented in the previous Chapter 3.

Contrary, in the study of Hanke et al. (2012) better resolved models explode easier and faster because the turbulent energy cascade transports energy from small to larger scales. As argued in Hanke et al. (2012) on the basis of parametrized, simplified models, large-scale bubbles in the turbulent postshock flow are mainly responsible for shock expansion. However, in our simulations performed with the VERTEX-PROMETHEUS code large-scales mass motion are induced by strong SASI sloshing motions and rather by convection as discussed in Section 3.5. That could explain the missing angular resolution dependence opposite to the simplified models of Hanke et al. (2012).

Let us now turn to the discussion of the effect of an increased radial resolution comparing the models with 400 radial zones with the additional model “s27 normal 600r” employing an increased number of 600 radial zones. The shock radius of this model is typically roughly 10 km smaller than all other less resolved models (Figure 4.1). This is a consequence of the slightly slower shock expansion during the first ~ 80 ms after core bounce, because of the smaller neutron star radius of the better resolved model at the beginning of the simulation (Figure 4.2). Later on, the size of the neutron star equals for all models, while the gap of 10 km between the different radially resolved models maintains at least in the first two hundred milliseconds. Due to the somewhat smaller shock radius and thus the reduced size of the gain layer, the total energy deposition of neutrinos in the gain layer is reduced (Figure 4.5). Towards the development of a runaway situation the model evolution diverges. While models with the standard radial resolution are evolving in a similar way, shock expansion of model

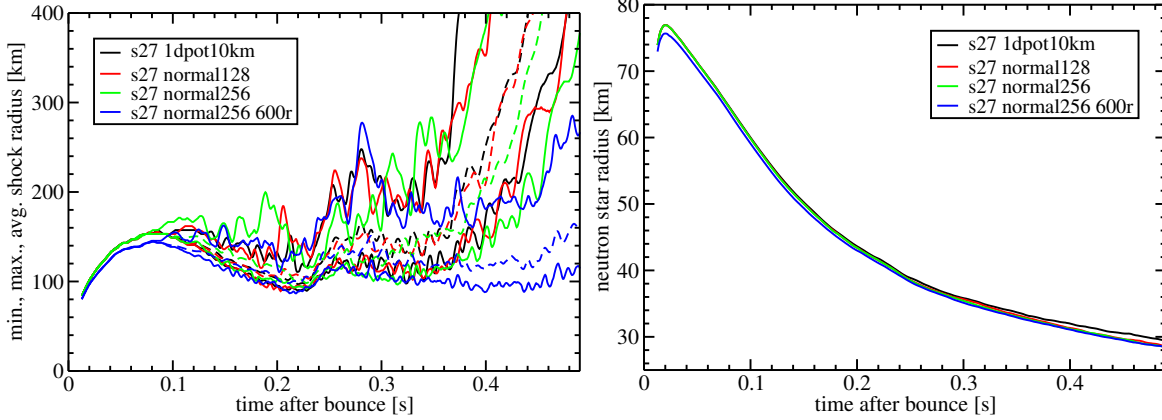


Figure 4.1: Minimum, maximum, and average shock radius as function of time after bounce for models with different angular and radial resolution. Note that the curves have been smoothed using a running average over 5ms.

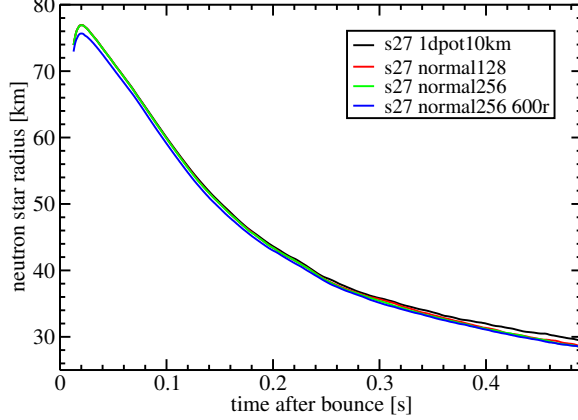


Figure 4.2: Neutron star radius as function of time after bounce for models with different angular and radial resolution. Note that the curves have been smoothed using a running average over 5ms.

“s27 normal 600r” with higher employed radial resolution is obviously delayed compared to the other models. Once a runaway situation is established, the shock radius of the standard models depicted in Figure 4.1 starts to rise steeply in contrast to the model “s27 normal 600r”. Similarly, for this model, the criteria for an explosive situation of the postshock region, the ratio of advection to heating timescale, is increasing continuously, but slowly towards the critical value of unity, while the timescale ratio of all other models is sharply rising at around ~ 330 ms (Figure 4.3). Because of the highly non-linear evolution of the hydrodynamic postshock flow, a detailed understanding of the delayed explosion with increased radial resolution seems to be difficult. Nevertheless, one might argue that due to the different initially imposed density perturbations grow somewhat slower in smaller grid cells. Another reason could be that the large sloshing SASI motions responsible for shock expansion in our models are slightly damped because of the reduced cell sizes. Displaying the amplitude of the first SASI coefficient, Figure 4.4 reflects a somehow smaller shock expansion in a SASI sloshing period, especially at later postbounce times. While the SASI motions of the models with 400 radial zones are getting larger and larger leading to the explosion, the SASI amplitude of model “s27 normal 600r” remains lower delaying shock expansion.

Our finding that improved radial resolution for a fixed angular grid has a negative influence on the development of an explosion is consistent with the results of Hanke et al. (2012) on the basis of their strongly simplified models, although they could not obtain fully convergence of the radial resolution in multi-dimensional because of an artificial dependence of their analytical neutrino terms on the radial zone number.

4.2 A slightly simplified setup

This section is intended to justify the slightly simplified setup used for the three-dimensional simulations with the VERTEX-PROMETHEUS code in the next chapters. To meet the extreme

4. The Dependence of the Postbounce Evolution on the Grid Setup in Axisymmetry

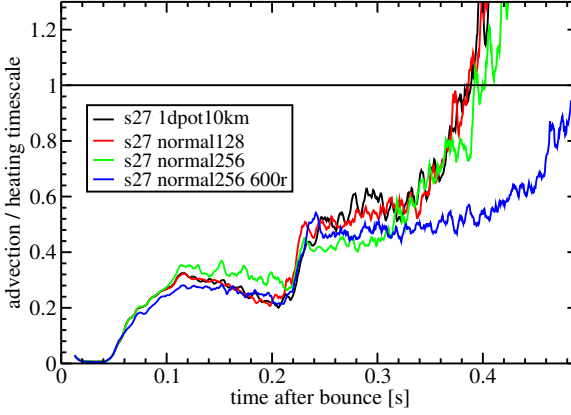


Figure 4.3: Time evolution of the ratio of the advection timescale to the heating timescale in the gain layer for models with different angular and radial resolution. Note that the curves have been smoothed using a running average over 5ms.

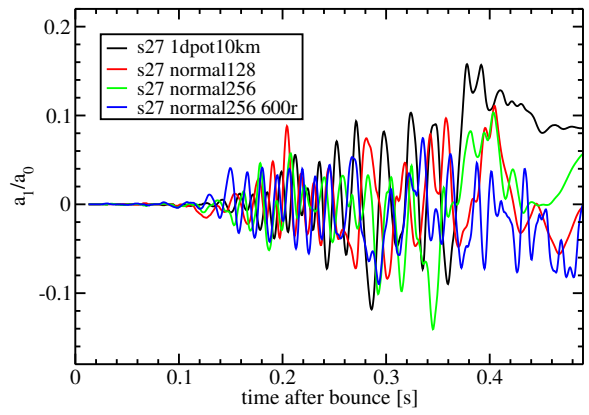


Figure 4.4: Time evolution of the first normalized coefficient a_1/a_0 of the spherical harmonics expansion of the shock surface for models with different angular and radial resolution. Note that the curves have been smoothed using a running average over 5ms.

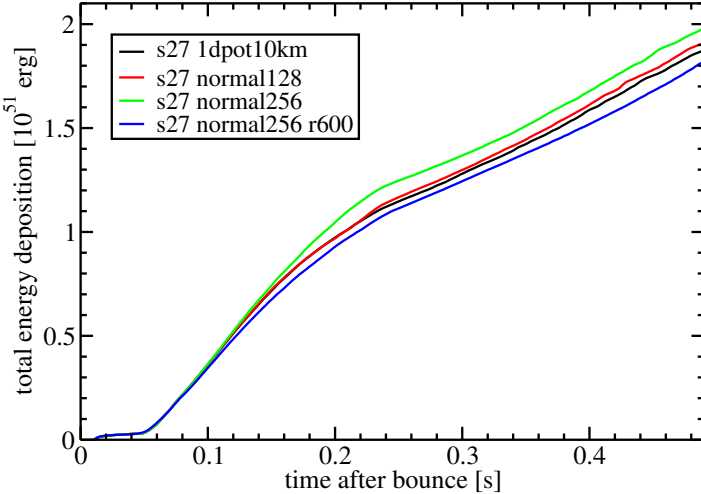


Figure 4.5: Time evolution of the total (time-integrated) energy deposited in the gain layer for models with different angular and radial resolution.

compute resource demands of a single self-consistent 3D neutrino-hydrodynamics supernova simulation the setup of the 2D simulations summarized in Section 3.1 is slightly changed. Here, the impact of differences in the numerical setup are shortly investigated on the basis of model “s27 1dpot10km” (see Table 4.1 for the specific changed parameters). In the previous section investigating the angular resolution dependence we have already checked that the reduced number of lateral zones does not impact the postbounce evolution (see the similar evolution of the shock radius in Figure 4.1 and of the runaway criteria in Figure 4.3). Next, the size of the spherical symmetric inner core of the grid is enlarged to 10 km and could influence and disturb convective activity in the interior of the neutron star. Numerical tests have shown that at around 10 km and deeper the neutron star becomes convective stable at least for the

first 400 ms. Indeed, the strength of convective activity is the same in model “s27 1dpot10km” and in models with the usually applied very narrow inner 1D core as the time evolution of the size of the neutron star is exactly the same (Figure 4.2). Thirdly, necessary for performing 3D simulations we assume only monopolar gravity assuming a spherical symmetric stellar background for calculating self-gravity. One could argue that the large-scale mass motions associated with the SASI are suffering from a repulsive force connected to the miscalculated gravitational potential at a certain angular position. Instead, the strength of the SASI sloshing motions is similar for this model as indicated by the first coefficient of the spherical harmonics expansion in Figure 4.4 and the overall similar shock oscillations and motions visible in Figure 4.1. The overall very similar evolution of the slightly simplified model “s27 1dpot10km” to the models employing the standard setup used so far is very reassuring for performing the very first 3D neutrino-hydrodynamics supernova simulations with this setup changes (see next chapter).

5 SASI Activity and Convective Overturn in Fully Self-consistent 3D Core-Collapse Supernova Simulations

Currently, the most urgent challenge and goal in core-collapse supernova research is to advance from 2D to 3D modeling with full neutrino transport and to overcome the artificial symmetry restrictions imposed so far in sophisticated models due to the tremendous compute time requirements of a single self-consistent simulation run. The large set of axisymmetric, self-consistent explosion models presented in the previous chapters is a great success and an important step forward in core-collapse supernova modeling. We have successfully shown that the neutrino-driven mechanism is able to launch explosion for a wide range of progenitor models as indicated by previous studies (Buras et al. 2006b; Marek & Janka 2009; Müller et al. 2012b,a; Bruenn et al. 2013; Suwa et al. 2010). However, let's move on in our efforts in supernova modeling!

Performing the step from 2D to 3D modeling of core-collapse supernovae several points should be noted and summarized:

- The 2D explosions obtained so far in self-consistent setups presented in the previous chapters seem to be somehow marginal and are exploding very late, typically several hundred milliseconds after core bounce.
- Therefore, 3D models are urgently needed to confirm the explosion mechanism suggested by 2D simulations! Is the driving engine of the current supernova models an artefact of the artificial imposed symmetry restriction? Can we even get easier and faster explosion in 3D as suggested for example by Nordhaus et al. (2010)?
- Of course, nature is three dimensional and the 2D models performed so far impose the constraint of axisymmetry. Thus, the hydrodynamic flow in the supernova core is forced to a toroidal structure. How will the postshock flow change when the artificial symmetry restriction is overcome?
- Mainly, as we have already discussed in Hanke et al. (2012) on the basis of simplified, parametrized supernova models, the turbulent cascade in 3D transports energy from large to small scales and thus, the turbulent cascade is inverse to 2D. How will the different energy redistribution in 2D and 3D affect the ability for an explosion?
- In this context, it is an very interesting, open question if the “standing-accretion shock instability” (SASI; Blondin et al. 2003) also occur in 3D as a supportive aid for the shock revival as identified in Section 3.5 and e.g. in Marek & Janka (2009).

Thus, we will focus in this chapter on the development of hydrodynamic instabilities in the supernova core, convection and the SASI, and then continue the overall question if we can obtain successful explosions without any symmetry restrictions in comparison to the exploding counterpart 2D models. Main parts of this chapter have been already presented in the publication of Hanke et al. (2013) focussing on the $27M_{\odot}$ progenitor of Woosley et al. (2002). In the discussion we will include a second 3D model investigating the $20M_{\odot}$ progenitor of Woosley & Heger (2007).

Up to now most investigations of convection and the SASI in core-collapse supernovae have relied on axisymmetric (2D) simulations. Three-dimensional (3D) models based on various approximations for treating neutrino heating and cooling in the supernova core have only recently become available, but have already sparked a controversy about the development and mutual interaction of the two instabilities in 3D. Burrows et al. (2012) and Dolence et al. (2013), who conducted simulations using a simple light-bulb neutrino scheme, were rather outspoken in classifying the SASI as a subdominant phenomenon in the presence of neutrino heating. They argued that the violent sloshing motions seen in 2D neutrino-hydrodynamics simulations may be an artifact of the artificial symmetry assumption and are actually nothing but 2D convection in disguise. Murphy et al. (2013) also noted that nonlinear convection theory appears to explain the 3D flow properties of their models without the need of invoking the SASI as an additional instability. At first glance, these findings seem to be in line with other 3D studies relying on a similar light-bulb methodology (Iwakami et al. 2008; Nordhaus et al. 2010; Hanke et al. 2012; Couch 2013) or on a gray neutrino transport approximation with chosen neutrino luminosities imposed at an inner grid boundary (Wongwathanarat et al. 2010, 2013; Müller et al. 2012c). In contrast, Müller et al. (2012a) demonstrated by self-consistent, 2D, general relativistic (GR) simulations with sophisticated transport that genuine SASI activity remains possible for sufficiently small shock stagnation radius (caused by high mass accretion rates in the particular case of a $27M_{\odot}$ progenitor of Woosley et al. 2002). This suggests that details of the conditions may decide about the growth of the SASI, and that these conditions may not only depend on the properties of the progenitor star but also on the exact behavior of the stalled shock, which again depends on a reliable treatment of the neutrino physics. The mentioned 3D models might simply have missed the sweet spot for SASI growth in parameter space.

Recent Newtonian simulations by Takiwaki et al. (2012, 2013) as well as Couch & O'Connor (2013); Couch & Ott (2013) and GR simulations by Kuroda et al. (2012) and Ott et al. (2013) are first, tentative steps to higher sophistication in 3D models, but these works were still focused on a few progenitors only and employed crude neutrino transport methods with various simplifications concerning the description of neutrino propagation, of neutrino interactions, and of the energy dependence of the transport. Ott et al. (2013), using a neutrino leakage scheme and studying the same $27M_{\odot}$ progenitor as Müller et al. (2012a), observed low-level SASI activity at early times, which was eventually suppressed in models which exploded because of artificially enhanced neutrino heating. Their neutrino treatment, however, is not on par with the multi-group ray-by-ray-plus transport of Müller et al. (2012a) and therefore comparisons with the more sophisticated 2D models of Müller et al. (2012a) should be made only with great caution and reservation. Applying the same neutrino leakage scheme as Ott et al. (2013), Couch & O'Connor (2013) are extending the previous work by examining the development of neutrino-driven convection and the SASI. They found that either stability

can dominate. In their exploding 3D models the SASI strength is reduced, while in failed explosions the SASI grows similarly to our 2D models at late times, when the shock radius has become sufficiently small. Moreover, Couch & Ott (2013) claim that precollapse asphericity perturbations in the progenitor may be crucial for models at the threshold for an explosion.

In view of the poor exploration of conditions in collapsing stellar cores in 3D so far and considering the substantial approximations that have been made in 3D supernova simulations until now, the strong opinions uttered about the dominance of neutrino-driven convection (Burrows et al. 2012; Murphy et al. 2013; Dolence et al. 2013) and the categorical rejection of an important role of the SASI in “realistic” 3D supernova models (Burrows 2013) are disturbing. Actually, it is not overly astonishing that the highly simplified setup investigated by these authors did not show signs of any pronounced SASI activity. The growth of SASI modes was clearly disfavored in their models by several aspects. Neglecting neutrino losses from the neutron star interior (above an optical depth of about unity) and using a relatively stiff nuclear equation of state the authors prevented the neutron star from shrinking below ~ 60 km. Correspondingly, the shock radius remained rather large, in which case the postshock velocities were relatively small and the advection timescale of the accretion flow through the gain layer was relatively long. This damped the development of the SASI, whose growth rate is roughly proportional to the inverse of the advection timescale (cf. Scheck et al. 2008). At the same time such conditions supported neutrino-driven convection, which preferably develops in the accretion flow for ratios χ of the advection time to the local buoyancy timescale above a critical value of $\chi \approx 3$ (Foglizzo et al. 2006).

Although the theoretical understanding of the growth conditions of the SASI and neutrino-driven convection is mostly based on linear theory (e.g., Foglizzo et al. 2007; Laming 2007; Yamasaki & Yamada 2007; Yamasaki & Foglizzo 2008; Guilet & Foglizzo 2012), the predictions were found to be consistent with the behavior seen in 2D hydrodynamic simulations of accretion shocks in collapsing stellar cores (Scheck et al. 2008) and in full-scale 2D supernova models (Müller et al. 2012a). Similarly, although it is *a priori* not clear whether the SASI sloshing motions (Blondin et al. 2003) and spiral modes (Blondin & Mezzacappa 2007; Fernández 2010) observed in adiabatic accretion flows in 2D and 3D, respectively, or in shallow-water experiments (Foglizzo et al. 2012), are conclusive for phenomena of relevance in the convectively unstable environment of the neutrino-heated layer, violent bipolar shock oscillations with SASI-typical characteristics were also identified to determine the evolution of the stalled supernova shock in some progenitors and preexplosion phases (e.g., Scheck et al. 2008; Müller et al. 2012a). While the phenomenon of the SASI as an advective-acoustic instability is not generically linked to 2D, strong SASI activity has so far not been detected in full-scale 3D supernova simulations and it was speculated that its amplitude could be reduced by the kinetic energy being shared between three instead of two dimensions (Iwakami et al. 2008), that the absence of a flow-constraining symmetry axis might disfavor coherent mass motions of low spherical harmonics modes (Burrows 2013), or that neutrino-driven buoyancy is generally the fastest growing nonspherical instability in supernova cores (Burrows et al. 2012).

In this chapter, we report about unambiguously identified SASI activity in the first 3D simulations with detailed neutrino transport of the $27 M_{\odot}$ progenitor model that was investigated by Müller et al. (2012a) and of the $20 M_{\odot}$ progenitor discussed in Bruenn et al. (2013). For these 3D simulations we employed the VERTEX-PROMETHEUS neutrino-hydrodynamics code

with detailed ray-by-ray-plus neutrino transport and the sophisticated treatment of energy-dependent neutrino interactions presented in Chapter 2 and also applied in previous 2D simulations with this code (e.g., Buras et al. 2006a; Marek & Janka 2009) and in the 2D GR models of Müller et al. (2012b,a, 2013). Furthermore, this code has been extensively employed to perform the large set of 2D simulations presented in Chapter 3. Contrary to the claims discussed above, our model shows that despite the presence of neutrino-driven convection, the SASI can grow no less vigorously in 3D (without any coordinate grid-imposed symmetry) than in 2D as long as small shock radii are maintained because of high mass accretion rates and guarantee favorable growth conditions. We also observe the development of a clear spiral mode. SASI shock motions appear to be diminished only when the accretion rate drops after the Si/SiO shell interface reaches the shock and the shock is able to expand to considerably larger radii. The variation of the relative strengths of neutrino-driven convection and SASI sloshing is consistent with experience and understanding based on previous 2D simulations.

5.1 Numerical Methods and Modeling Setup of our 3D Simulations

The calculations of the supernova models in 2D and 3D presented in this chapter were performed with the elaborate neutrino-hydrodynamics code VERTEX-PROMETHEUS presented in Chapter 2. We employ as close as possible the same setup as used for our 2D simulation set discussed in Chapter 3. Nevertheless, to meet the tremendous computer resource demands of a single self-consistent 3D neutrino-hydrodynamics supernova simulations the setup of the 2D summarized in Section 3.1 is slightly changed. Firstly, the angular resolution of 1.41° is reduced to 2.05° , which corresponds to a total number of angular zones of $88 \times 176 = 15488$. As discussed in Chapter 2 this number is equal to the number of compute cores used in parallel for a single model. Since a multi-dimensional simulation run needs several months of continuous computation, this number of compute cores is the upper value currently available to us on the newest supercomputers. Secondly, in 2D and 3D the size of the spherical symmetric inner core of the grid is enlarged to the innermost 10 km to avoid excessive time-step limitations due to the very small cell sizes at the poles of the 3D spherical polar grid (see e.g. Hanke 2010). Thirdly, contrary to the models discussed in Chapter 3, in the simulations presented here, we assume monopolar gravity, but include general relativistic corrections by means of an effective gravitational potential (Marek et al. 2006, see Section 2.1.2). In 2D setups we have proven that these small setup changes hardly affect the postbounce supernova dynamics as discussed in Section 4.2. The corresponding 2D models used for comparison are modeled exactly with the same setup as employed in the 3D models.

We simulate the evolution of the $27 M_\odot$ progenitor of Woosley et al. (2002), which was previously investigated by Müller et al. (2012a) and Ott et al. (2013) and of the $20 M_\odot$ progenitor of Woosley & Heger (2007) studied by Bruenn et al. (2013), both in 2D and in 3D, using the high-density equation of state (EoS) of Lattimer & Swesty (1991) with a nuclear incompressibility of $K = 220$ MeV. Both models have already been discussed in Chapter 3. The models are computed on a spherical polar coordinate grid with an initial resolution of $n_r \times n_\theta \times n_\varphi = 400 \times 88 \times 176$ (3D) and $n_r \times n_\theta = 400 \times 88$ (2D) zones. Later, refinements of the radial grid ensure adequate resolution in the PNS surface region. Seed perturbations for aspherical instabilities are imposed by hand 10 ms after bounce by introducing random perturbations of 0.1% in density on the whole computational grid.

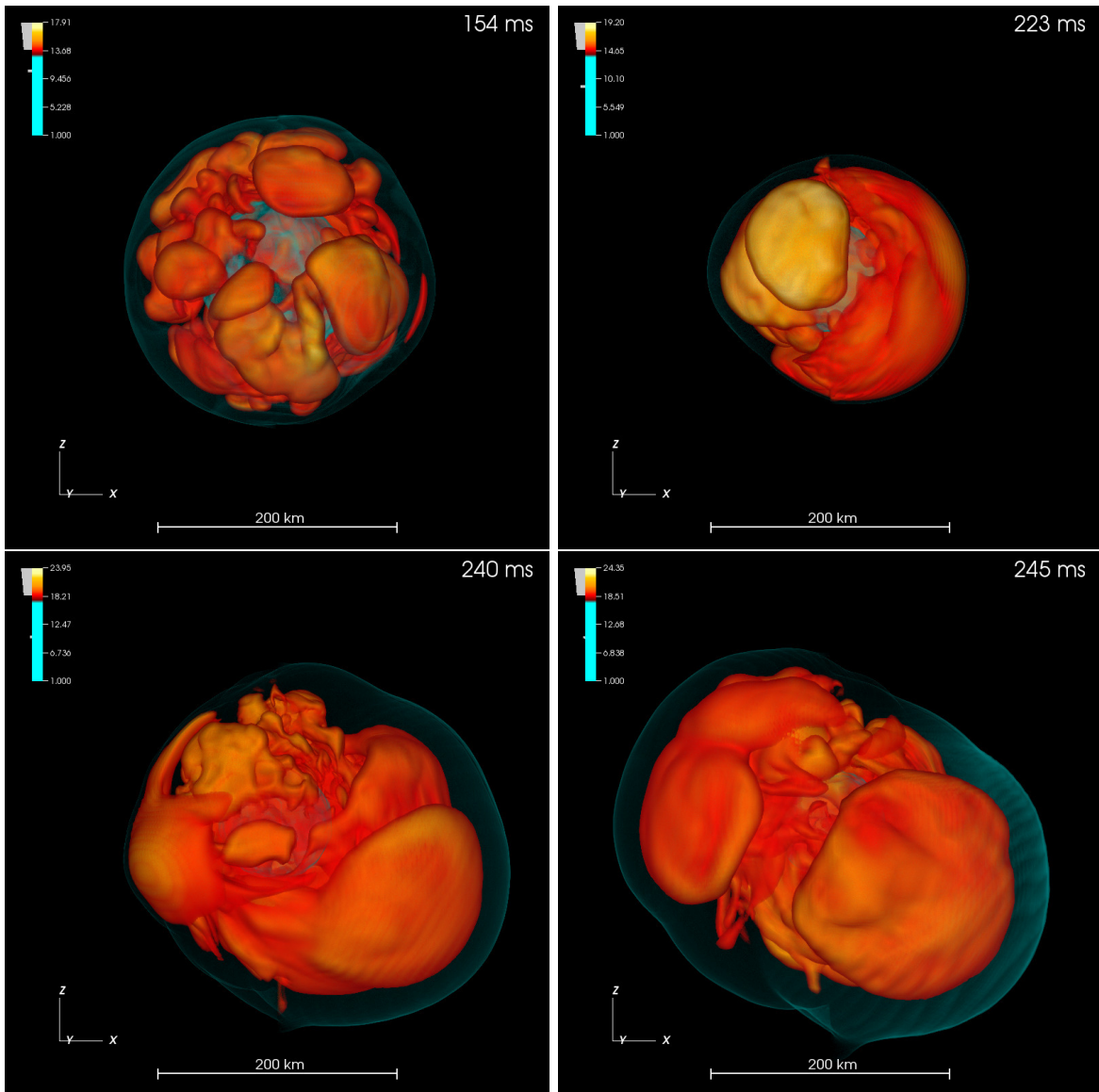


Figure 5.1: Snapshots of phases with convective and SASI activity in the evolution of the $27 M_{\odot}$ model at post-bounce times of 154 ms, 223 ms, 240 ms, and 245 ms. The volume rendering visualizes surfaces of constant entropy: The outer, bluish, semi-transparent surface is the supernova shock, the red surfaces are entropy structures in the postshock region. The upper left panel displays mushroom-like plumes of expanding, high-entropy matter that are typical of neutrino-driven buoyancy. The upper right and both lower panels show distinctly different entropy structures of dipolar (and quadrupolar) asymmetry, which engulf the still visible buoyant plumes with their higher-order spherical harmonics mode pattern. The entropy asymmetries of $\ell = 1, 2$ character are caused by global shock sloshing motions, which create hemispheric high-entropy shells in phases of shock expansion.

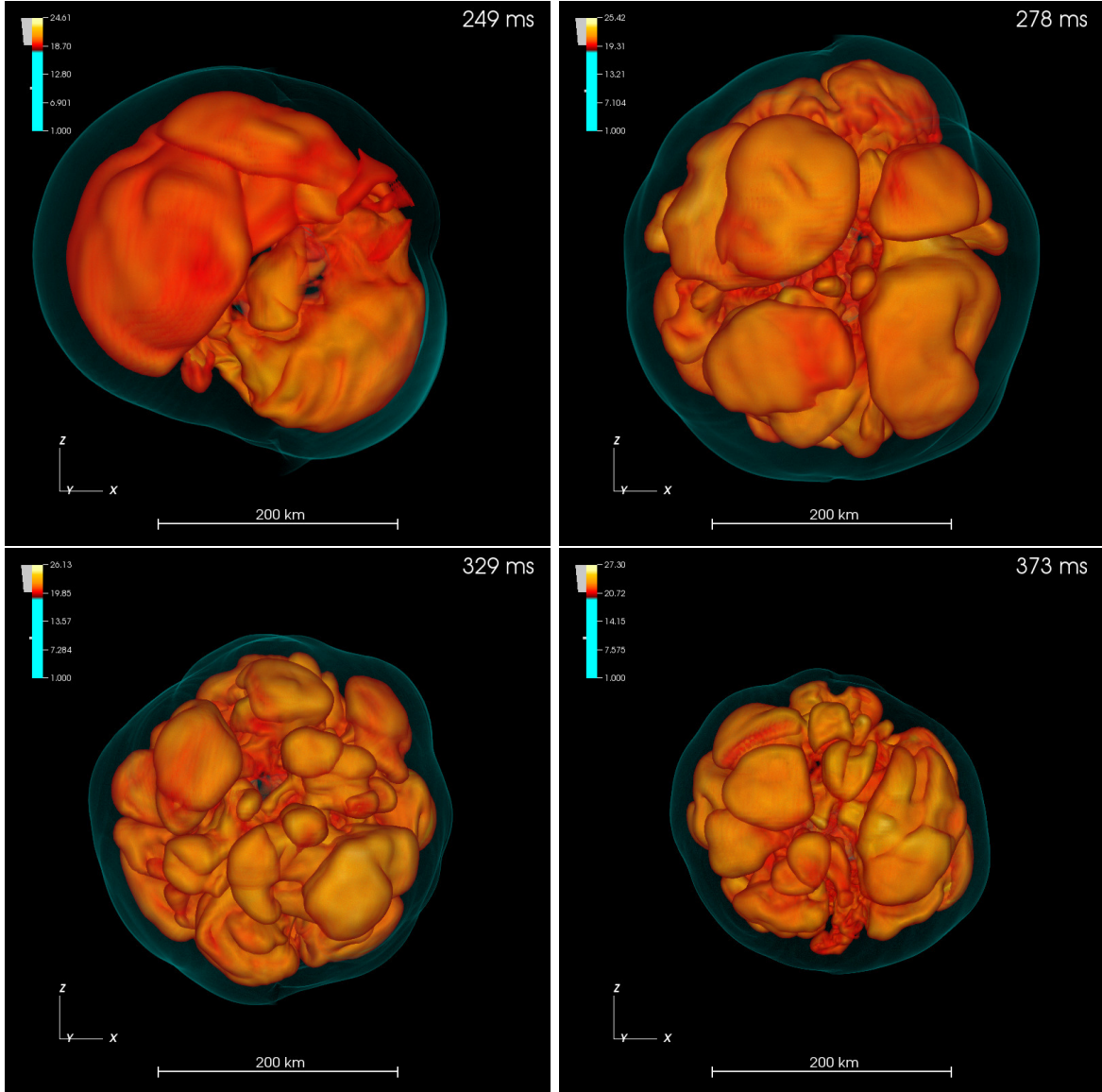


Figure 5.2: Further snapshots of phases with convective and SASI activity in the evolution of the $27 M_{\odot}$ model at post-bounce times of 249 ms, 278 ms, 329 ms, and 373 ms. The upper left panel displays a phase of violent expansion motion towards the upper left corner of the plot. In the upper right panel at 278 ms the vivid SASI phase is over, the shock is more spherical again, and the postshock entropy structures correspond to neutrino-driven plumes. The large high-entropy bubbles are decaying into small mushroom-like plumes typical of neutrino-driven convection. Both lower panels depict the shrinking surface of the supernova shock.

5.2 SASI Activity in 3D Models and its Comparison to 2D

While both the SASI and convection can lead to large-scale shock deformations, the SASI is distinguished by a characteristic oscillatory growth and in its nonlinear stage by the quasi-periodic, oscillatory nature of the shock motions. In 2D, the artificial symmetry constraint

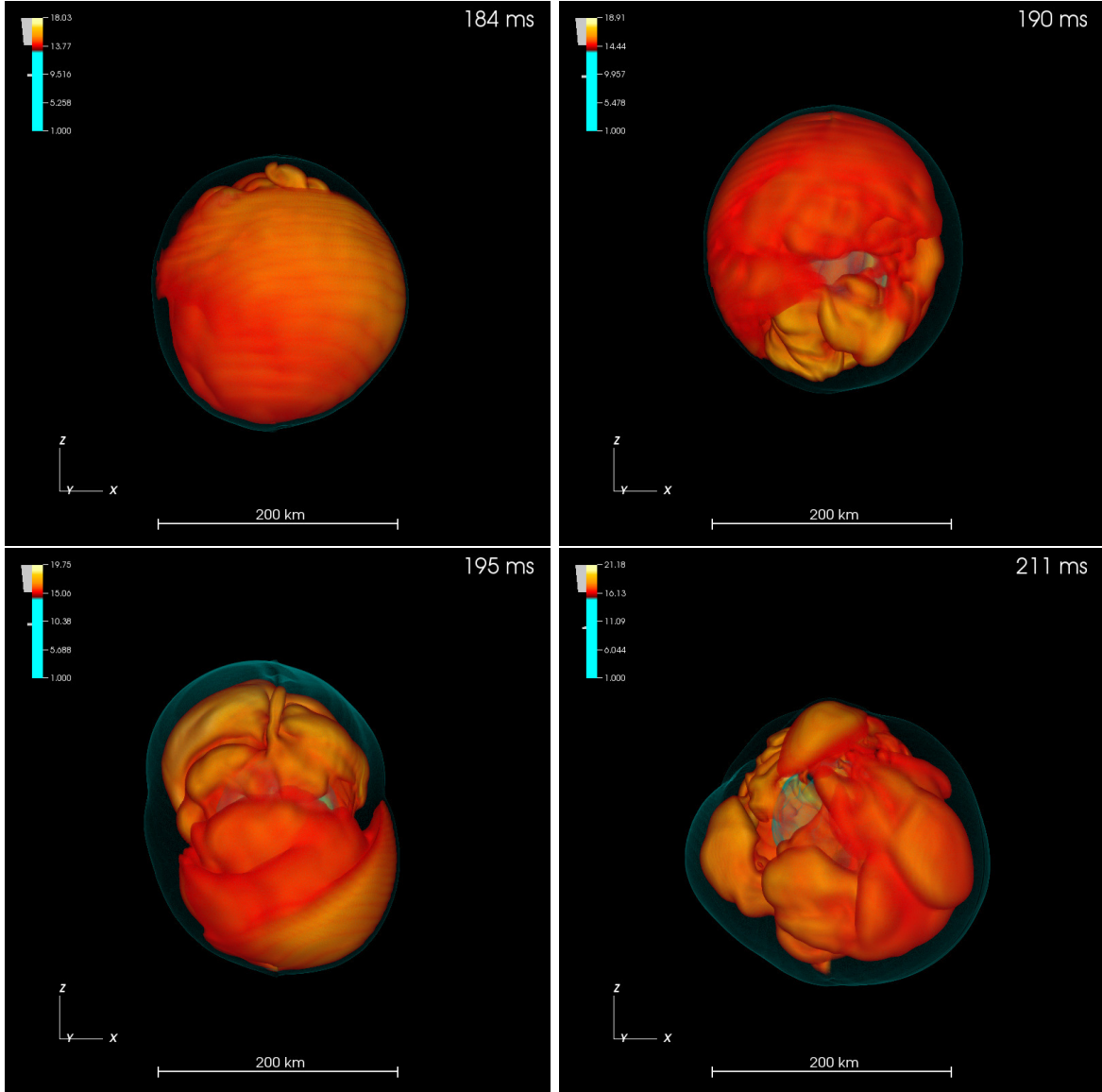


Figure 5.3: Snapshots of phases with convective and SASI activity in the evolution of the $20 M_{\odot}$ model at post-bounce times of 184 ms, 190 ms, 195 ms, and 211 ms. Analogously to the volume rendering of the $27 M_{\odot}$ model surfaces of constant entropy are displayed. The upper left panel shows the dominance of a large-scale structure of dipolar asymmetry. The upper right and both lower panels depict the violent sloshing motions of the shock surface, which is slightly expanding by time. The entropy asymmetries of $\ell = 1, 2$ character is experiencing a counterclockwise rotation.

and the excitation of large-scale modes by the inverse turbulent cascade could still produce a quasi-periodic sloshing motion even in convectively-dominated models (Burrows et al. 2012), and a more refined analysis is necessary to identify the SASI (Müller et al. 2012a). However, in 3D the distinction is much clearer, since large-scale shock deformations caused by buoyancy-driven convection initially evolve randomly without any identifiable periodicity and then grow monotonically once they reach a certain threshold amplitude (Burrows et al. 2012). Periodic

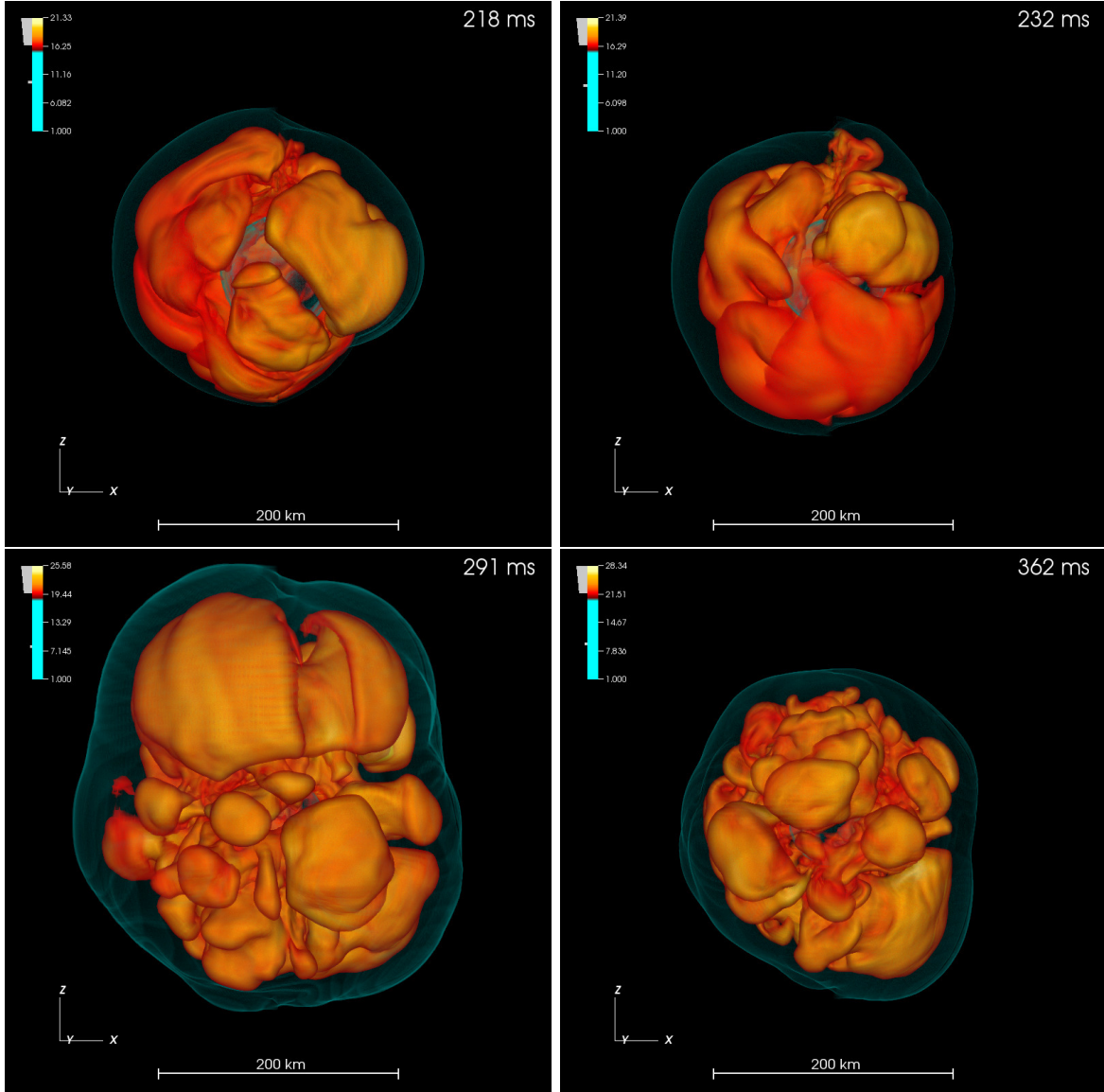


Figure 5.4: Further snapshots of phases with convective and SASI activity in the evolution of the $20 M_{\odot}$ model at post-bounce times of 218 ms, 232 ms, 291 ms, and 362 ms. The two upper panels show the continuous vivid SASI phase. At 291 ms displayed in the lower left panel the shock surface reaches its maximal prolongation pushed towards the top edge of the panel. Depicted in the lower right panel the extension of the shock surface is significantly smaller compared to its maximum. The deformation of the shock is reduced, while the postshock flow is dominated by small mushroom-like plumes typical for neutrino-driven convection bubbles.

SASI oscillations and large-scale shock deformations caused by convection can therefore hardly be mistaken for each other in 3D.

Images of the entropy distribution in the postshock layer of our 3D simulation of the $27 M_{\odot}$ progenitor (Figures 5.1 and 5.2) indeed provide a clear hint that both distinctly different instabilities are at work in the shocked accretion flow around the nascent neutron star. The

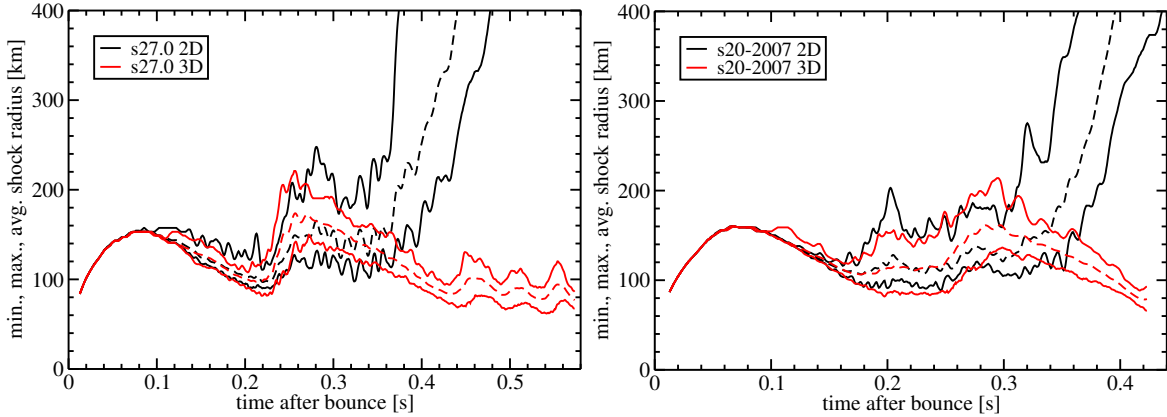


Figure 5.5: Time evolution of the minimum, maximum (solid line), and average (dashed line) shock radius as function of time after bounce for the $27 M_{\odot}$ SN progenitor (left panel) and the $20 M_{\odot}$ SN progenitor (right panel). The 3D results (red) are shown together with the corresponding 2D run (black). Note that the curves have been smoothed using a running average over 5 ms.

instabilities develop nearly at the same time and are present simultaneously for an extended period of the simulated postbounce evolution. The first small mushroom-like Rayleigh-Taylor fingers of neutrino-driven convection become visible around 80–100 ms after bounce to subsequently grow stronger and larger in angular size over a timescale of some ten milliseconds. At about 125 ms p.b. the rising plumes begin to cause shock deformation and a modest amount of global asphericity of the accretion layer. Until ~ 155 ms the activity in the postshock layer is clearly dominated by neutrino-driven buoyancy (Figure 5.1, upper left panel), but at $t \gtrsim 155$ ms, during a phase of accelerated shock recession, coherent entropy structures show up first. The corresponding low-mode spherical harmonics pattern clearly differs from the buoyant mushrooms on smaller angular scales. This phenomenon is associated with shock oscillations, which quickly amplify to bipolar shock sloshing motions and create characteristic, hemispheric high-entropy shells during phases of fast shock expansion. These half-shells of shock-heated matter engulf the buoyant bubbles of neutrino-driven convection in deeper regions (Figure 5.1, upper right and both lower left panels as well as Figure 5.2 upper left panel). While the sloshing axis initially wanders, it becomes more stable as the SASI sloshing of the shock further grows in amplitude and violence between ~ 195 ms and ~ 240 ms. As a consequence, an expansion of the average shock radius is driven even before the Si/SiO composition-shell interface arrives at the shock and the mass accretion rate starts to drop steeply at $t \sim 220$ ms (Figure 5.6). The decrease of the accretion rate supports the shock expansion, in course of which the bipolar, quasi-periodic shock pulsations gain even more power. At $t \sim 225$ ms a spiral mode seems to set in for several revolutions before the average shock radius reaches its maximum extension at ~ 250 ms and the SASI sloshing dies off at $t \gtrsim 260$ ms. The presence of large-amplitude spiral motions is reflected by considerable variations of the mean shock radius between 230 ms and 260 ms. These disappear when the SASI activity ceases at $t \sim 260$ ms (Figure 5.5). Later on, aspherical mass motions in the postshock layer are dominated again by the buoyant plumes typical of neutrino-driven convection (Figure 5.2, upper right panel and both lower panels). The radius of the shock surface (Figure 5.5) is now continuously shrinking because of insufficient neutrino heating. Possible

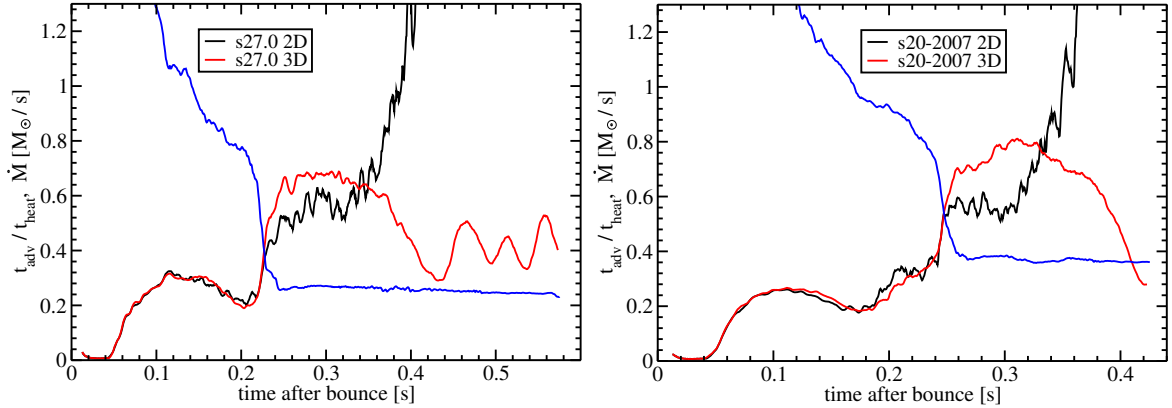


Figure 5.6: Time evolution of the runaway criterion $t_{\text{adv}}/t_{\text{heat}}$ for the 2D (black) and 3D (red) simulations and the mass accretion rate of the stellar core at 400 km (blue) as function of time after bounce. The $27 M_{\odot}$ SN progenitor (left panel) and the $20 M_{\odot}$ SN progenitor (right panel) are depicted. The runaway criterion is smoothed using a running average over 5 ms.

reasons for the failing onset of the explosion in 3D will be discussed later on in Section 5.6.

Let us now turn to the discussion of our second 3D simulation of the $20 M_{\odot}$ progenitor. Images of the entropy distribution in the postshock layer (Figures 5.3 and 5.4) further solidates the insight that both instabilities, the SASI and convection, can develop in the hydrodynamic postshock flow in a 3D setup. It is another example of a 3D model with strong, violent SASI activity. Please note that the corresponding 2D run performed with the same, although slightly changed setup of the 3D model is exploding about 55 ms later than the simulation of the $20 M_{\odot}$ progenitor of Woosley & Heger (2007) discussed in Section 3.7 (see also Table 3.1 for the exact parameters at the onset of the explosion). While changing the setup slightly has no effect for the simulation of the $27 M_{\odot}$ progenitor setup as proved in Section 4.2), the crucial growth of a sufficient large high-entropy bubble for triggering the explosion is delayed in the case of the $20 M_{\odot}$ progenitor. Similarly, to the simulation of the $27 M_{\odot}$ progenitor, first mushroom-like Rayleigh-Taylor finger of neutrino-driven convection develop around 80–100 ms after bounce. Because of the higher mass accretion rate of this model in the first two hundred milliseconds after bounce (Figure 5.6) the shock surface is shrinking more rapidly. Consequently, the subsequently growth of neutrino-driven buoyancy is suppressed, which is engulfed by a large coherent entropy structure. At $t \sim 170$ ms during the phase of fast shock recession, a low-mode spherical harmonics pattern starts to develop (Figure 5.3, upper left panel). Noticeable, the bipolar shock oscillations transit to a fast spiral motion of the shock surface with a counterclockwise rotation (Figure 5.3, upper right and lower left panel). The SASI sloshing of the shock continues and grows in amplitude by time between $t \sim 170$ ms and $t \sim 290$ ms (Figure 5.3, lower right panel and Figure 5.4, both upper panels). This time period of active SASI shock oscillations is significantly longer as in the simulation of the $27 M_{\odot}$ progenitor. While the shock radius of this model is significantly enlarged at the arrival of the Si/SiO composition-shell interface at the shock enabling the mass accretion rate to drop steeply, the shock surface of the $20 M_{\odot}$ progenitor model depicted in Figure 5.5 is expanding continuously independently of the arrival of the boundary between the silicon shell and the oxygen-enriched silicon shell at $t \sim 250$ ms (Figure 5.6). At around $t \sim 291$ ms (Figure 5.4,

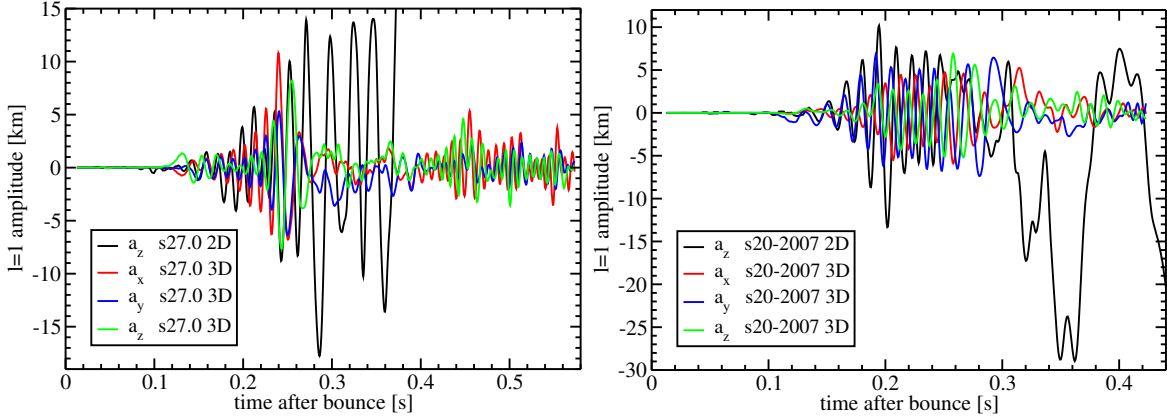


Figure 5.7: Time evolution of the first coefficient of the spherical harmonics expansion of the shock surface a_1 as function of time after bounce for the $27 M_\odot$ SN progenitor (left panel) and the $20 M_\odot$ SN progenitor (right panel). The 3D results (red) are shown together with the corresponding 2D run (black). Note that the curves have been smoothed using a running average over 5 ms.

lower left panel) a large high-entropy bubble pushes the shock surface to its maximal prolongation. At this point the SASI activity ceases similarly to $27 M_\odot$ progenitor model and later on buoyant mushrooms are dominating the convective flow behind the shrinking supernova shock surface (Figure 5.4, lower right panel).

This verbal description of the dynamical evolution of the postshock accretion layer is supported by a detailed analysis based on several time-dependent parameters that quantify the characteristic features of SASI activity. To this end we perform a time-dependent decomposition of the angle-dependent shock position $r_{\text{sh}}(\theta, \varphi)$ into spherical harmonics Y_ℓ^m :

$$a_\ell^m = \frac{(-1)^{|m|}}{\sqrt{4\pi(2\ell+1)}} \int_\Omega r_{\text{sh}}(\theta, \varphi) Y_\ell^m(\theta, \varphi) d\Omega. \quad (5.1)$$

Here the Y_ℓ^m are real spherical harmonics with the same normalization as used by Burrows et al. (2012) and Ott et al. (2013). The orthonormal harmonic basis functions are

$$Y_\ell^m(\theta, \phi) = \begin{cases} \sqrt{2} N_l^m P_l^m(\cos \theta) \cos m\phi & m > 0, \\ N_l^0 P_l^0(\cos \theta) & m = 0, \\ \sqrt{2} N_l^{|m|} P_l^{|m|}(\cos \theta) \sin |m|\phi & m < 0, \end{cases} \quad (5.2)$$

where

$$N_l^m = \sqrt{\frac{2l+1}{4\pi} \frac{(l-m)!}{(l+m)!}}, \quad (5.3)$$

$P_l^m(\cos \theta)$ are the associated Legendre polynomials, and θ and ϕ are the spherical coordinate angles. With this choice of basis functions, the coefficients with $\ell = 1$ give the angle-averaged Cartesian coordinates of the shock surface,

$$a_1^{-1} = \langle y_{\text{sh}} \rangle =: a_y, \quad a_1^0 = \langle z_{\text{sh}} \rangle =: a_z, \quad a_1^1 = \langle x_{\text{sh}} \rangle =: a_x, \quad (5.4)$$

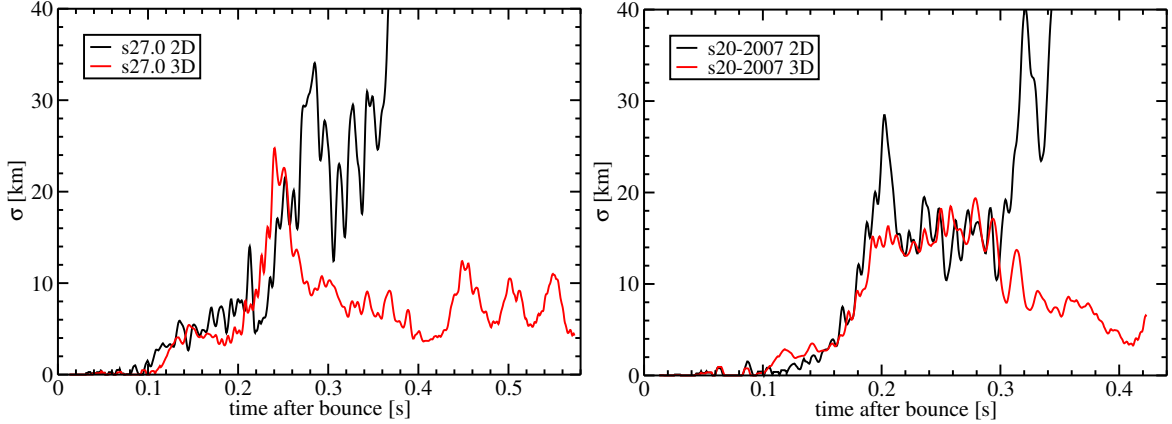


Figure 5.8: Time evolution of the rms shock deformation σ as function of time after bounce for the $27 M_{\odot}$ SN progenitor (left panel) and the $20 M_{\odot}$ SN progenitor (right panel). The 3D results (red) are shown together with the corresponding 2D run (black). Note that the curves have been smoothed using a running average over 5 ms.

and a_0^0 is just the average shock-radius $\langle r_{\text{sh}} \rangle$. For axisymmetric 2D setups, the coefficients a_{ℓ}^m for the decomposition of the shock surface into spherical harmonic components reduce to the ones given already in Eq. (3.17).

The time evolution of the coefficients a_x , a_y (3D), and a_z (3D and 2D) is shown in Figure 5.7 for the $27 M_{\odot}$ progenitor (left panel) and the $20 M_{\odot}$ progenitor (right panel). Discussing first the $27 M_{\odot}$ progenitor case, both in 2D and in 3D, the shock surface clearly oscillates in a quasi-periodic manner until ~ 260 ms after bounce, i.e. until shortly after the Si/SiO shell interface has reached the shock and the accretion rate has dropped considerably between ~ 220 ms and 240 ms p.b. The lower accretion rate results in a pronounced expansion of the average shock radius (Figure 5.5), which initially is stronger in 3D. However, the 2D model maintains large (albeit less regular) shock oscillations, with the average shock radius eventually overtaking the 3D model at ~ 300 ms when an explosion develops (i.e. somewhat later than in the GR simulation of Müller et al. 2012a). However, it is not clear whether this difference or how much of this difference is caused by GR effects, because the models in the present paper were simulated with a slightly different treatment of the low-density equation of state, which led to a significant delay (~ 35 ms) of the infall of the silicon layer and a correspondingly later arrival of the Si/SiO shell interface at the shock. By contrast, the shock continues to recede in the 3D run. The more optimistic evolution of the 2D model compared to the failing 3D model at late stages is consistent with the findings of Hanke et al. (2012), and could be due to the action of the inverse turbulent energy cascade, which continues to feed energy into large-scale modes in 2D.

Inspecting now the SASI activity of the $20 M_{\odot}$ progenitor model, Figure 5.7 displays at first glance the discussed differences in the postbounce evolution of both 3D models. The decomposition of the shock surface reflects the faster growth of SASI activity to its maximal strength until ~ 190 ms and later on the large shock surface oscillations in a quasi-periodic manner in the 3D simulation of the $20 M_{\odot}$ progenitor is maintained for a long time period. Similarly to the $27 M_{\odot}$ progenitor run, the shock expansion becomes even more favorable for the 3D run until ~ 290 ms after bounce. However, in the 2D case of this model shock

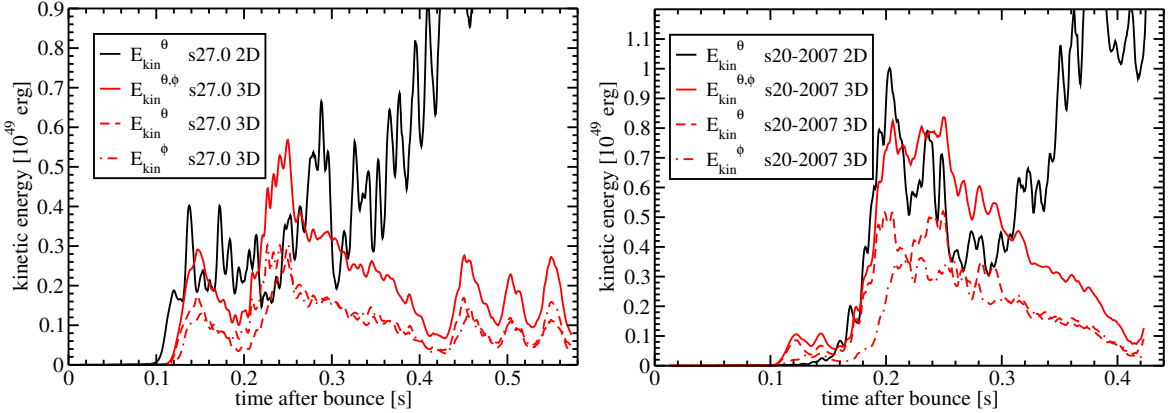


Figure 5.9: Kinetic energy of lateral mass motions in the gain layer as function of time after bounce for the $27 M_{\odot}$ SN progenitor (left panel) and the $20 M_{\odot}$ SN progenitor (right panel). The 3D results (red) are shown together with the corresponding 2D run (black). Note that the curves have been smoothed using a running average over 5 ms.

oscillations become also less regular, nonetheless maintain large to push the shock outwards driving the explosion. The SASI activity of the 3D model ceases resulting in a shrinking shock surface. Thus, although the specific time evolution of the SASI activity is different due to the respective progenitor structure, the 3D run of $20 M_{\odot}$ progenitor confirms the possibility of developing strong SASI activity in 3D environment.

However, the evolution of the two simulations of the $27 M_{\odot}$ progenitor prior to the infall of the Si/SiO interface is remarkable: While the amplitude of the $\ell = 1$ mode is initially larger in 2D, the individual components a_x , a_y , and a_z of the $\ell = 1$ amplitude vector in 3D become comparable to a_z in 2D around 200 ms, and a_x even reaches considerably bigger values. During this phase, the SASI is undoubtedly stronger in 3D than in 2D. A similar evolution of stronger SASI activity in 3D can be detected for the $20 M_{\odot}$ progenitor, although after the infall of the Si/SiO interface. Shortly before reaching the maximal expansion of the shock surface at ~ 290 ms after bounce the individual components of the $\ell = 1$ amplitude vector in 3D even larger as a_z in 2D. Especially, the amplitude of a_y is clearly larger at this phase in time evolution.

Further confirmation of this assessment is provided by the root-mean-square deviation $\sigma(r_{\text{sh}})$ of the shock radius from its average value (Figure 5.8):

$$\sigma = \sqrt{(4\pi)^{-1} \int (r_{\text{sh}}(\theta, \varphi) - \langle r_{\text{sh}} \rangle)^2 d\Omega} \quad (5.5)$$

For reasonably small amplitudes, σ is also a measure for the total power of SASI amplitudes with different ℓ :

$$\sigma \approx \sqrt{\sum_{\ell=1}^{\infty} \sum_{m=-\ell}^{\ell} |a_{\ell}^m|^2}. \quad (5.6)$$

Indeed, the size of shock deformation of both 3D models is larger compared to the 2D runs during the respective phases of stronger SASI activity, between 220 ms and 240 ms after

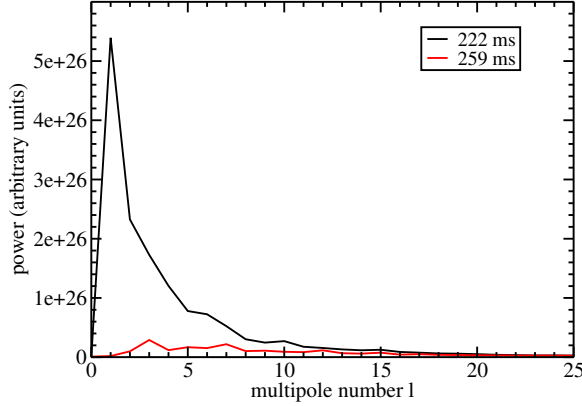


Figure 5.10: Power spectra of v_φ of the $27 M_\odot$ 3D model sampled between $r = 63$ km and 80 km at post-bounce times of 222 ms (black) and 259 ms (red). At 222 ms, the strong SASI produces a distinctive peak at $l = 1$, which is absent during the later, convection-dominated phase.

bounce at the infall of the Si/SiO interface for the $27 M_\odot$ progenitor and between 240 ms and 280 ms after bounce for the $20 M_\odot$ progenitor while strongest SASI activity.

The same picture emerges when we consider the kinetic energies E_θ and E_φ associated with motions in the θ - and φ -directions in the gain region,

$$E_\theta = \frac{1}{2} \int_{V_{\text{gain}}} \rho v_\theta^2 dV, \quad E_\varphi = \frac{1}{2} \int_{V_{\text{gain}}} \rho v_\varphi^2 dV. \quad (5.7)$$

As shown in Figure 5.9, the total energy contained in non-radial motions of the 3D simulations of the $27 M_\odot$ progenitor is also larger than in the corresponding 2D run during the relevant phase around ~ 230 ms. In the period of continuous increase of the SASI amplitude in the 3D model between $t \sim 155$ ms and ~ 240 ms, the kinetic energy grows and σ exhibits quasi-periodic modulations signaling the shock sloshing motions. In the phase of a higher shock deformation in 3D compared to 2D, the angular kinetic energies is also higher for the $27 M_\odot$ progenitor. Most interestingly, the other 3D simulation of the $20 M_\odot$ progenitor experiences a very long time period between $t \sim 220$ ms and ~ 310 ms of higher angular kinetic energies indicating more vivid SASI and convective activity in the 3D run compared to the 2D model. While the angular kinetic energies of the 2D models of both progenitors increases continuously towards the explosion, the ongoing decrease of the respective kinetic energies of non-radial motions in the 3D simulations reflects the insufficient turbulent mass motions behind the shock.

Interestingly, during the phase of strongest SASI activity we find rough equipartition between the kinetic energies of non-radial motions $E_\theta + E_\varphi$, and the energy E_r contained in fluctuating radial velocities,

$$E_r = \frac{1}{2} \int_{V_{\text{gain}}} \rho (v_r - \langle v_r \rangle)^2 dV, \quad (5.8)$$

where $\langle v_r \rangle$ is the angle-averaged radial velocity. This equipartition is apparently not a unique feature of buoyancy-driven turbulence (cf. Murphy et al. 2013), at least not as far as these volume-integrated quantities are concerned.

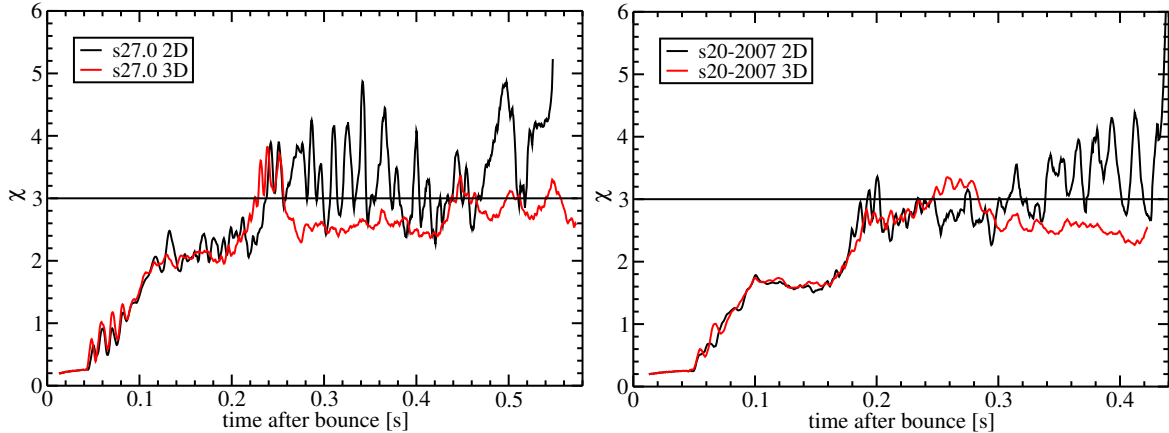


Figure 5.11: Time evolution of stability parameter χ for the gain layer as function of time after bounce for the $27 M_{\odot}$ SN progenitor (left panel) and the $20 M_{\odot}$ SN progenitor (right panel). The 3D results (red) are shown together with the corresponding 2D run (black). Note that the curves have been smoothed using a running average over 5 ms. During most of the time $\chi < 3$. This suggests conditions in the postshock accretion flow which disfavor the growth of neutrino-driven convection relative to the development of the SASI in analogy to the 2D model of $27 M_{\odot}$ SN progenitor discussed by Müller et al. (2012a). Indicating convective activity the threshold value $\chi = 3$ is exceeded in the phase of largest shock expansion and strongest SASI activity in both models.

A clear difference between SASI dominated and convection dominated phases of the $27 M_{\odot}$ 3D model can be observed in the power spectrum of the azimuthal velocity v_{φ} as a function of multipole order ℓ . Figure 5.10 shows the spectra for the $27 M_{\odot}$ progenitor case during a SASI active phase (222 ms p.b.) compared to the later time (259 ms) when the SASI motions cease and convective plumes with their higher-order multipole pattern determine the asphericities in the postshock region again. The power spectra are evaluated with Equation (8) of Hanke et al. (2012) for v_{φ} (weighted with the square root of the density) integrated over a radial region between 63 km and 80 km. The presence of the SASI low-mode deformation at 222 ms leads to a prominent peak of the power spectrum at low multipole orders, which is absent in the later spectrum.

In the case of the $27 M_{\odot}$ progenitor, the shock deformation and SASI amplitude moderately increase as the shock retreats between ~ 100 ms and 200 ms p.b. (The same is true for the specific nonradial kinetic energy in the gain layer, although the kinetic energy decreases temporarily because of the decreasing mass in the gain region.) It is noteworthy that the few tens of milliseconds of stronger SASI activity in the 3D model of the $27 M_{\odot}$ progenitor coincide with a phase of more rapid shock expansion than in 2D. Conceivably, the more energetic SASI motions provide a stronger push against the pre-shock ram pressure. A close examination of the $\langle r_{\text{sh}} \rangle$ in Figure 5.5 shows that some (oscillatory modulated) SASI-aided shock expansion seems to set in around 190 ms, i.e. already before the rapid drop of the preshock mass-accretion rate that begins at ~ 220 ms. Therefore one might speculate that with slightly more time available for the growth of the SASI, the extra support by nonradial SASI motions might have driven the 3D model over the threshold for a neutrino-powered runaway expansion of the shock after the infall of the Si/SiO interface.

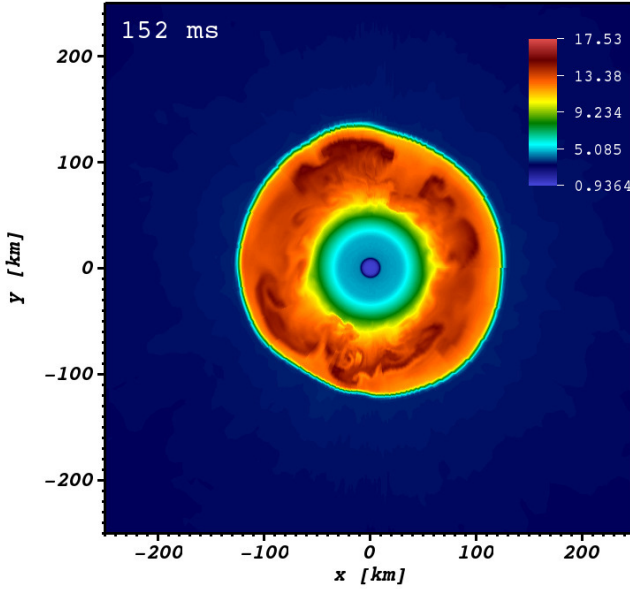


Figure 5.12: Snapshot of the entropy (color coded according to color bar at the upper left corner, in units of Boltzmann's constant k_b per nucleon) in the plane through the origin normal to the vector $\mathbf{n} = (-0.35, 0.93, 0.12)$ at a post-bounce time of 152 ms in the $27 M_\odot$ 3D model. The high-entropy plumes with high-order spherical harmonics pattern suggest buoyancy-driven convective overturn of neutrino-heated matter.

The case of the $20 M_\odot$ progenitor provides more insight for such a speculation. In this 3D model the conditions for longer growth of the SASI are fulfilled. Nonradial mass motions set in earlier and cease later than in the $27 M_\odot$ progenitor model reflected in a more continuous growth of the average radius $\langle r_{\text{sh}} \rangle$ in Figure 5.5. The rms shock deformation depicted in Figure 5.8 remains for a much longer time period at least on the level of the corresponding 2D run. Nevertheless, the SASI activity ceases similarly to the $27 M_\odot$ progenitor model. Because of the inverse dependence of the SASI growth conditions to the shock radius and thus the advection timescale (see Section 3.5 in the discussion of our set of 2D models), we argue that SASI activity dies, when the shock attempts to enlarge to radii more than around 200 km. Later on, we aim to discuss possible reasons why our 3D models are failing in Section 5.6. With respect to the outcome of our two 3D simulation runs based on progenitors incorporating a rapid drop of the preshock mass-accretion rate connected to the arrival of a strong Si/SiO composition-shell interface, an interesting question is indeed the investigation of further progenitor models. For example, the $15 M_\odot$ progenitor of Woosley & Heger (2007) as discussed in Section 3.7 does not incorporate a significant drop of the mass accretion rate at the arrival of the Si/SiO composition-shell interface (see Figure 3.21 for the respective 2D run) and thus, violent SASI activity could be maintained sufficiently long to act against the higher pre-shock ram pressure. The effect of such a different progenitor structure on the postbounce evolution of a 3D model remains to be investigated by future simulations.

Quite remarkably, the SASI is not only able to reach larger amplitudes in 3D than in 2D as

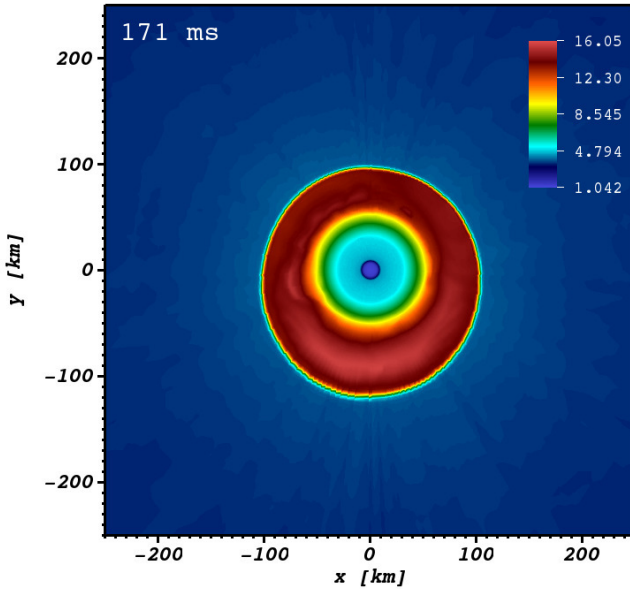


Figure 5.13: Snapshot of the entropy (color coded according to color bar at the upper left corner, in units of Boltzmann’s constant k_B per nucleon) in the plane through the origin normal to the vector $\mathbf{n} = (-0.56, -0.82, -0.20)$ at a post-bounce time of 171 ms in the $20 M_\odot$ 3D model. The absent of strong high-entropy plumes and the bipolar shock deformation indicates SASI domination of neutrino-heated matter at the early evolution phase of the $20 M_\odot$ 3D model.

long as its growth conditions remain favorable, but it is even found to develop despite some earlier convective activity. Already introduced in Section 3.5 for our set of 2D simulations, Figure 5.11 displays the critical parameter χ for the growth of convection as evaluated from spherically averaged stellar quantities in the gain layer of our 3D simulation of the $27 M_\odot$ and the $20 M_\odot$ progenitor models according to Equation (3.19). Despite $\chi < 3$ (Figure 5.11), however, convection develops around 80 ms after bounce in both of our 3D simulations. This happens because convective activity is not only seeded by the artificially imposed, random density perturbations of 0.1% amplitude (cf. Sect. 5.1) but also by numerical perturbations along the axis of the computational polar grid in one hemisphere, which we are not able to damp perfectly. Although still small, these numerical effects are sufficiently large to trigger the rise of a buoyant plume against the advection flow, which instigates further perturbations that exceed the linear regime. In this case convection can be initiated although $\chi < 3$ signals stability according to linear analysis (Foglizzo et al. 2006). We note in passing that the level of seed perturbations was smaller and well compatible with linear theory in the 2D models of Müller et al. (2012a), and we also emphasize that the axial perturbations have a noticeable effect only in the early growth phase of convection whereas no significant axial artifacts or alarming flow perturbations near the polar axis can be observed during the later phases of fully developed nonradial flow activity in the postshock flow (see Figures 5.1 and 5.2 for the $27 M_\odot$ model and Figures 5.3 and 5.4 for the $20 M_\odot$ progenitor). Most

noticeably, in line with the discussion of the driving hydrodynamic instabilities emerging in our 2D simulations in Section 3.5, the critical parameter exceeds the threshold value $\chi = 3$ for convective activity in the phase of largest shock expansion and strongest SASI activity triggering secondary convection (see Section 3.5 and e.g. Scheck et al. 2008). While the condition $\chi > 3$ remains fulfilled for the 2D models towards the explosion, the respective value for the 3D models drops below the threshold value again emphasizing the important supportive role of convective activity for driving. Once strong SASI and convective mass motions have developed in the flow, the supernova core contains a noise level so high that a subsequent decline of χ below the critical threshold of ~ 3 does not imply that convective activity is unable to continue (Müller et al. 2012a). However, it is questionable if the turbulent motion of our 3D models is strong enough for enlarging the shock surface. By trend, the postshock flow is dominated by a progressing fragmentation of the flow with small mushroom-like plumes typical for neutrino-driven convection bubbles (lower right panel of Figure 5.2 for the $27 M_\odot$ model and of Figures 5.4 for the $20 M_\odot$ progenitor, respectively), while flows on the largest-possible scale are actually responsible for shock expansion (Hanke et al. 2012).

Investigating the $27 M_\odot$ progenitor model, Figure 5.12 shows a snapshot of the entropy in a 2D slice at 152 ms. Here, the post-shock flow is still dominated by multiple, intermediate-scale plumes as familiar from buoyancy-driven convection. SASI shock sloshing becomes strong and temporarily dominant only afterward. The argument that any convective activity arising from sufficiently large seed perturbations will quench the SASI thus seems to be invalid. However, the $20 M_\odot$ model evolves somewhat different in the early postbounce evolution. Figure 5.13 shows analogously to Figure 5.12 a snapshot of the entropy in a 2D slice at 171 ms for the $20 M_\odot$ progenitor model. Here, the post-shock flow is dominated by strong SASI shock sloshing motions and convection plumes are almost absent. Only lateron convection increases as a consequence of the SASI when the shock expands due to strong SASI shock motion at 200 ms. Thus, this model provides an example of a vivid SASI growth despite any earlier convective activity much clearer than $27 M_\odot$ progenitor case. Thus, the competition between convection and the SASI is obviously more subtle than a superficial reading of recent papers (Burrows et al. 2012; Murphy et al. 2013; Müller et al. 2012b; Ott et al. 2013) might suggest. Some relevant aspects of the competing growth conditions and interaction of the two instabilities were discussed on the basis of 2D supernova simulations by Scheck et al. (2008).

5.3 The Spiral Mode of the SASI

While the SASI is limited to a sloshing motion along the symmetry axis in 2D, there is the possibility of a spiral mode in 3D (Blondin & Mezzacappa 2007; Iwakami et al. 2009; Fernández 2010), which could provide a means for angular momentum separation between the PNS and the ejecta, and might also have different saturation properties in the non-linear phase. In this context, based on an analysis of the models of Fernández (2010), Guilet & Fernández (2013) derived an analytical description of the angular momentum redistribution driven by a spiral mode of the SASI.

Detecting the spiral mode is not straightforward, as the time evolution of the coefficients a_ℓ^m needs to be taken into account. Merely computing the coefficients with $m \neq 0$ is not sufficient. In principle, spiral and sloshing modes can be disentangled by a Fourier analysis

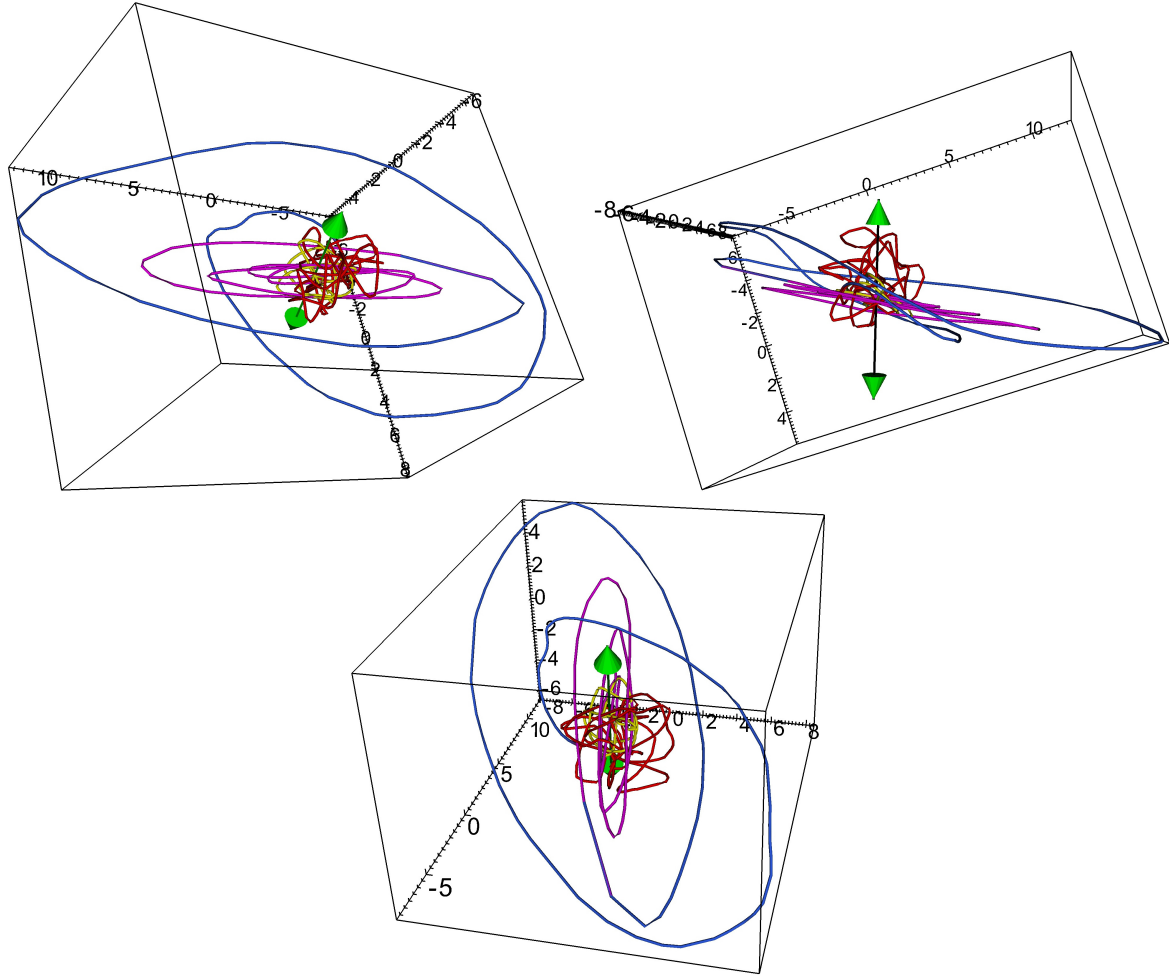


Figure 5.14: Evolution of the $\ell = 1$ amplitude vector \mathbf{a}_1 for the $27 M_{\odot}$ simulation from three different viewing angles. Different colors are used for the phase up to 177 ms (yellow), the phase of strong SASI sloshing activity (magenta, up to 225 ms), clearly developed SASI spiral motion (blue, up to 265 ms), and the late, SASI-quiet phase (red). The arrows indicate the vector $\mathbf{n} = (-0.35, 0.93, 0.12)$ and its counter-vector perpendicular to the rotational plane of the SASI (see also Figure 5.15). Note that the transition from SASI sloshing to spiral behavior is gradual (and associated with a strong growth of the angular momentum in the gain layer; Figure 5.17), and the color coding is based on eye inspection rather than a precise definition.

of $a_{\ell}^m(t)$ (Iwakami et al. 2008) if they remain stable over several oscillation periods. We use a somewhat different approach to visualize the character of the $\ell = 1$ mode in our 3D model of the $27 M_{\odot}$ progenitor here. The coefficients a_1^m can be combined into a vector,

$$\mathbf{a}_1 = (a_1^1, a_1^{-1}, a_1^0) = (a_x, a_y, a_z), \quad (5.9)$$

which is a rough measure of the angle-averaged displacement of the shock center from the origin and also indicates the direction and amplitude of the shock deformation (neglecting modes with higher ℓ). We visualize the time evolution of this amplitude vector in 3D space in Figure 5.14 with different colors of the trajectory indicating different phases of the $27 M_{\odot}$ progenitor simulation.

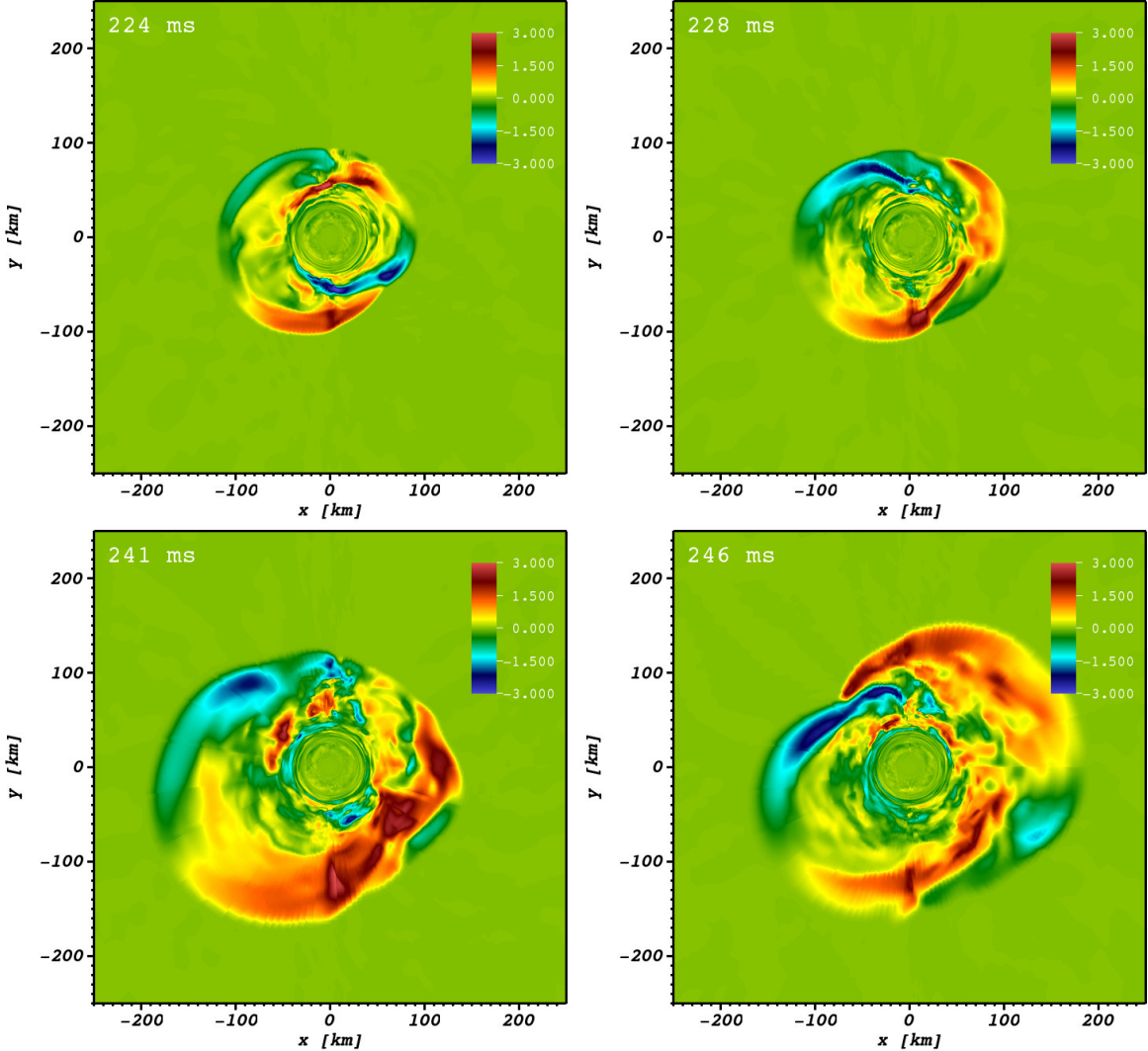


Figure 5.15: Snapshots of the rotational velocity around the origin in the plane perpendicular to $\mathbf{n} = (-0.35, 0.93, 0.12)$ at post-bounce times of 224 ms, 228 ms, 241 ms, and 246 ms during the 3D simulation of the $27 M_{\odot}$ progenitor. Red and yellow (positive velocity values) correspond to counterclockwise rotation.

Once the SASI starts to grow vigorously (blue curve), \mathbf{a}_1 initially moves along a narrow elliptical path with growing semi-major axis, indicating a predominant sloshing mode. Towards the phase of strongest SASI activity, the trajectory becomes more circular, signaling the transition to a spiral mode. The plane of the spiral remains relatively stable until the maximum amplitude is reached and the SASI dies down again. It is roughly perpendicular to the vector $\mathbf{n} = (-0.35, 0.93, 0.12)$, i.e. there is no alignment with the axis of the spherical polar grid. Figure 5.14 also further illustrates the different behavior during the “SASI-dominated” phase compared to the earlier and later “convectively-dominated” phases, during which \mathbf{a}_1 evolves in a more random fashion.

Slicing the $27 M_{\odot}$ progenitor model along the plane in which \mathbf{a}_1 predominantly moves allows us to visualize the distinctive spiral mode pattern, as shown in Figure 5.15. The snapshots of

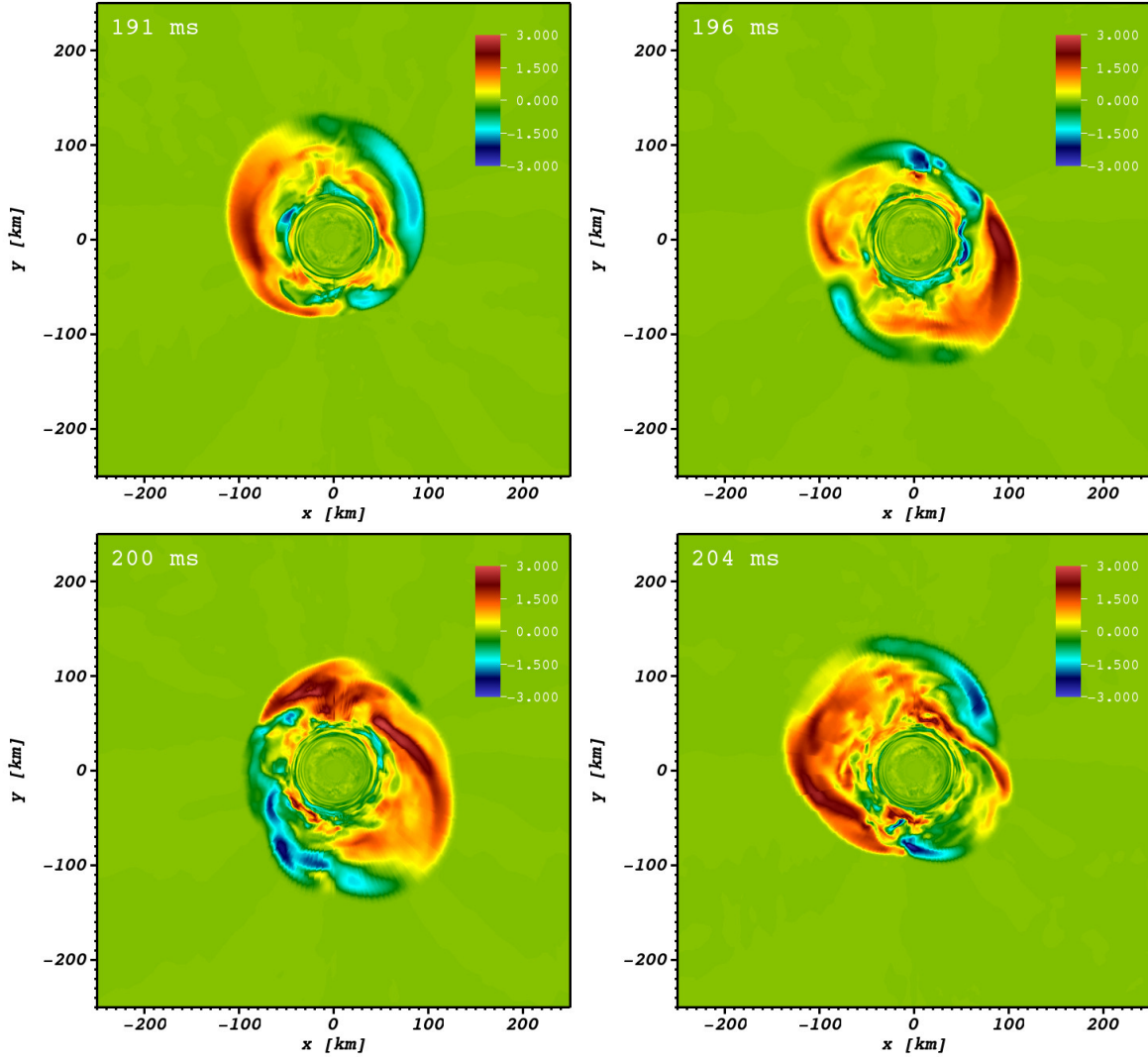


Figure 5.16: Snapshots of the rotational velocity around the origin in the plane perpendicular to $\mathbf{n} = (-0.56, -0.81, -0.20)$ at post-bounce times of 191 ms, 196 ms, 200 ms, and 204 ms during the 3D simulation of the $20 M_{\odot}$ progenitor.

the rotational velocity around the “axis” of the spiral mode (in the plane through the origin perpendicular to that axis) reveal two counter-rotating regions. While these regions are initially of comparable size, the flow in the counter-clockwise direction eventually dominates, and the rotation of the mode pattern with a continuously shifting triple point can clearly be seen.

Analogously, in the simulation of the $20 M_{\odot}$ progenitor model a pronounced spiral mode pattern develops, which lies in the plane roughly perpendicular to the vector $\mathbf{n} = (-0.56, -0.82, -0.20)$. As depicted in Figure 5.16 the snapshots of the rotational velocity around the “axis” of the spiral mode and indicates an earlier growth of the spiral mode in this model. Thus, the spiral model develops simultaneously to the sloshing mass motions instead of the transition of sloshing into spiral motions in the $27 M_{\odot}$ progenitor model. Between the onset of SASI activity at $t \sim 170$ ms and the arrival of the Si/SiO composition-shell interface at the shock

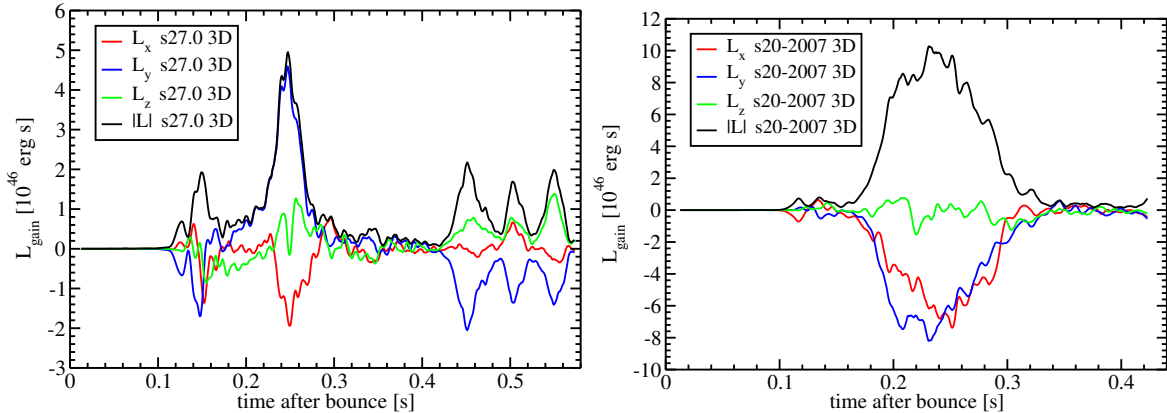


Figure 5.17: Time evolution of angular momentum components L_x , L_y , and L_z , and of the absolute magnitude $|L|$ of the total angular momentum contained in the gain region of the $27 M_\odot$ SN progenitor (left panel) and the $20 M_\odot$ SN progenitor (right panel). Note that the curves have been smoothed using a running average over 5 ms.

(Figure 5.6) (especially at postbounce times displayed in Figure 5.16) the spiral mass motions rotate very fast and are much longer active than in the $27 M_\odot$ progenitor model.

During the short phase of strong SASI activity, angular momentum separation by the spiral mode proceeds very efficiently, transferring a total angular momentum of $\sim 5 \times 10^{46}$ erg s for the $27 M_\odot$ progenitor model and $\sim 10 \times 10^{46}$ erg s for the $20 M_\odot$ progenitor model into the gain region (Figure 5.17). As expected, the angular momentum separation maintains much longer and is even stronger for the $20 M_\odot$ progenitor model indicating more vivid SASI activity in this case. In both models, the direction of the angular momentum vector is extremely similar to the normal vector of the spiral plane. However, all the angular momentum is eventually advected out of the gain region after the SASI has died down.

5.4 Revival of SASI Activity

After reporting, for the first time, about unambiguously identified SASI activity in a 3D simulation with detailed neutrino transport in Hanke et al. (2013), we have continued the 3D run of the $27 M_\odot$ progenitor to later postbounce times. As indicated in Figure 5.5 after reaching its maximum extension at ~ 250 ms the average shock radius is continuously shrinking because of the missing support of SASI activity and insufficient neutrino heating. The postshock region is dominated by small buoyant mushrooms (Figure 5.18, upper left panel). At around ~ 430 ms an interesting development in the time evolution of the postshock dynamics sets in. The supernova shock surface stops to shrink. As discussed in Section 3.5 the growth conditions for SASI activity become more and more favorable with a shrinking supernova shock radius. Indeed, coherent entropy structures of dipolar asymmetry are developing, which engulf the still visible buoyant plume (Figure 5.18, upper right panel). Similar to the $20 M_\odot$ progenitor case, as indicated by the following snapshots in Figure 5.18 (both lower panels) and in Figure 5.19 (upper left panel) an obvious fast spiral SASI mode is forming, which is again separating angular momentum (Figure 5.17). After some time, the spiral

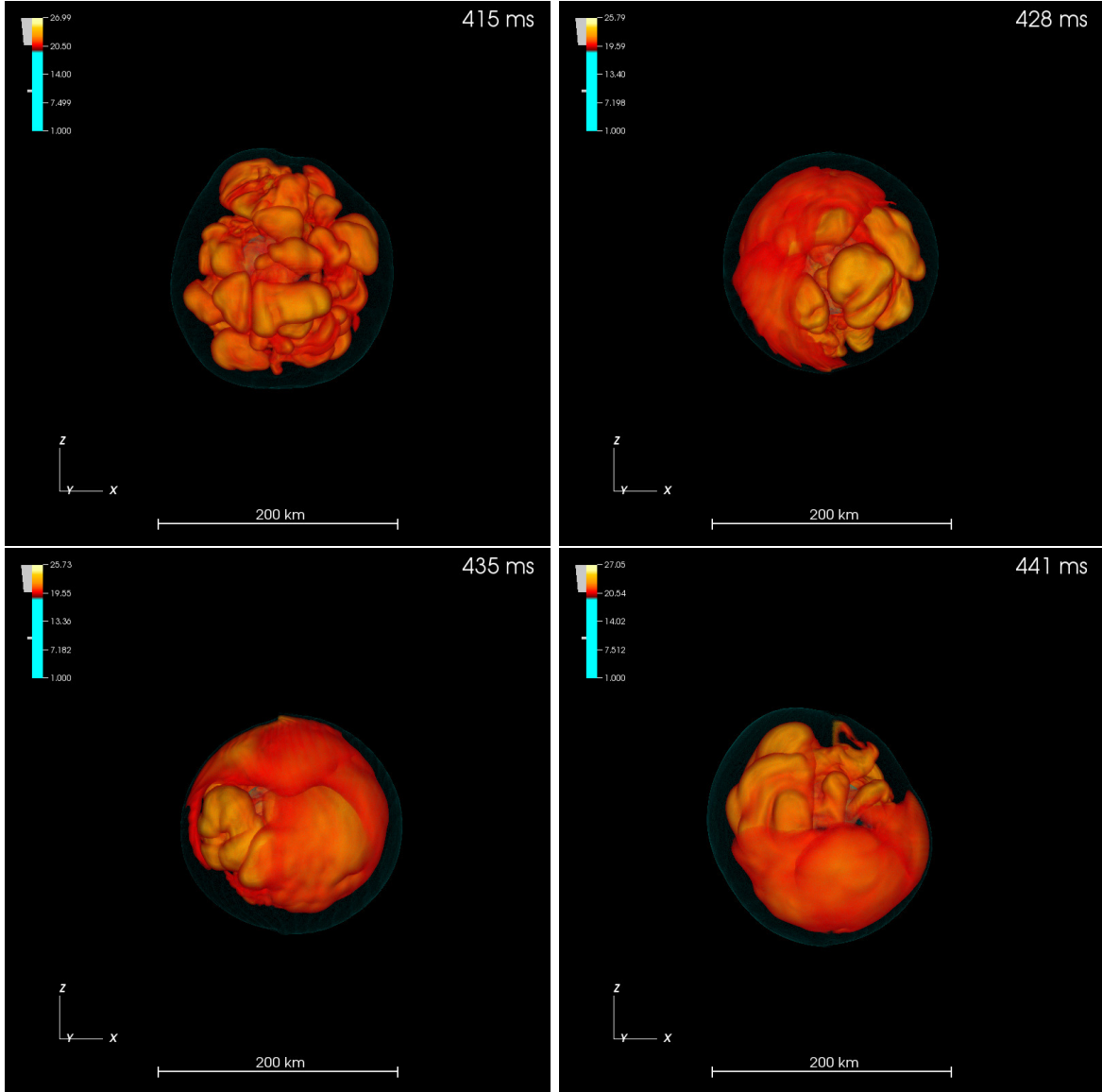


Figure 5.18: Snapshots of the first phase with revid SASI activity in the evolution of the $27 M_{\odot}$ progenitor at post-bounce time of 415 ms, 428 ms, 435 ms, and 441 ms. As previously, the same volume rendering visualizing surfaces of constant entropy is used. The upper left panel displays the significantly shrunk postshock region dominated by small buoyant mushrooms. The upper right and both lower panels show coherent entropy structures of dipolar asymmetry, which engulf the still visible buoyant plume and turn into spiral moss motions.

mode induces additionally a sloshing motion of the supernova shock surface (Figure 5.19, upper right panel) pushing its radius to larger values again (Figure 5.5). The revived SASI activity is reflected in a corresponding increase of the kinetic energy into angular directions (Figure 5.9) and of the deformation of the shock surface (Figure 5.8). Quantitatively, the amplitudes of the respective SASI coefficients are already growing again before low-mode entropy structures are showing up in the snapshots (Figure 5.7) indicating that the shrunk

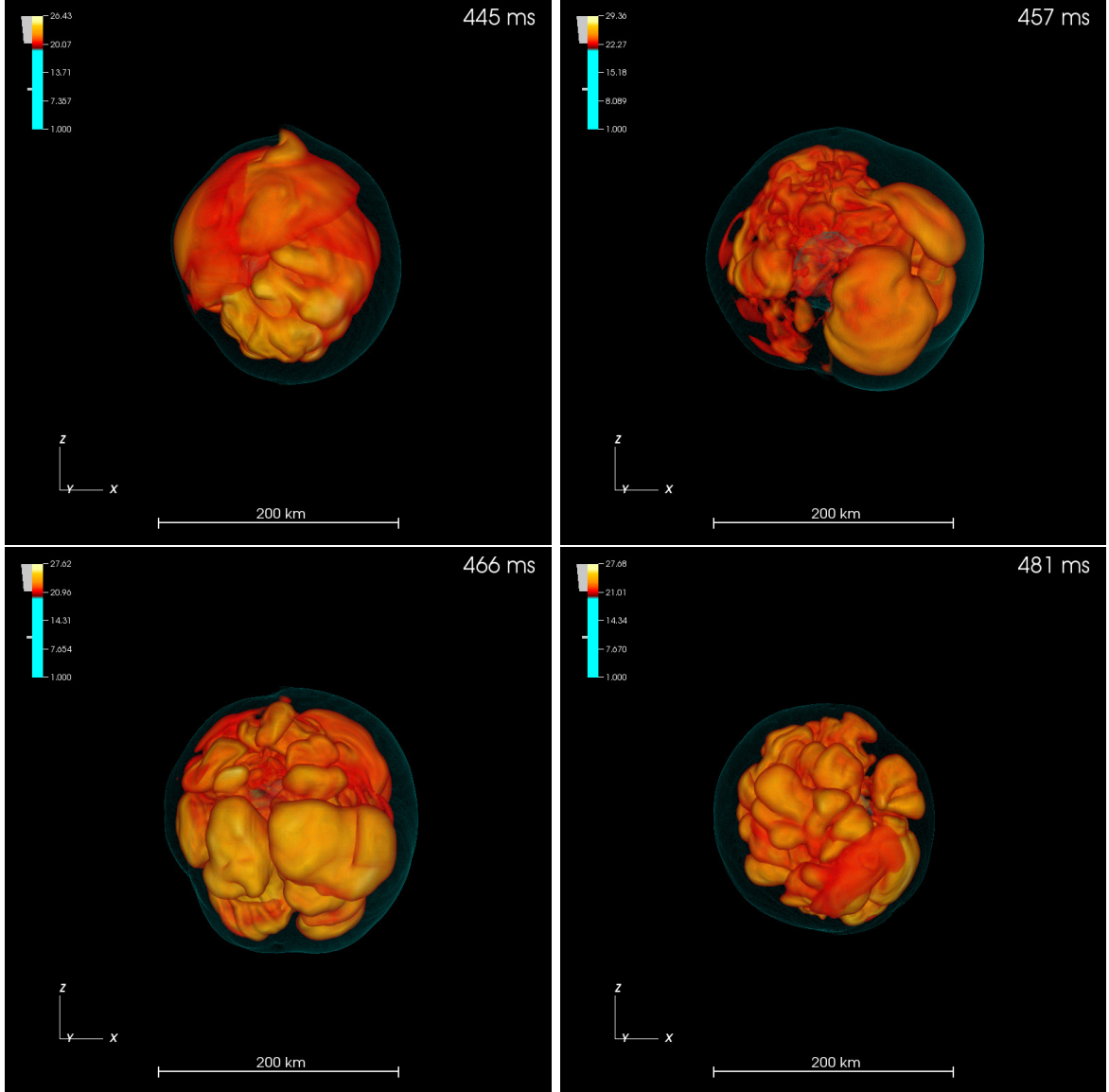


Figure 5.19: Further snapshots of the first phase with revid SASI activity in the evolution of the $27 M_{\odot}$ progenitor at post-bounce time of 445 ms, 457 ms, 466 ms, and 481 ms. The upper left panel depicts the still active SASI sloshing and motions, while in the upper right panel the shock surface reaches its maximum extension and the SASI ceases of. In the lower left panel convection is dominating again and in the lower right panel the postshock region is reduced again.

postshock region provides favorable conditions for the observed SASI revival. However, as the shock is pushed out with an absolute increase of ~ 35 km by sloshing motions, SASI activity ceases once more (Figure 5.19, lower left panel). Afterwards, convection dominates and the size of the postshock region is reduced again (Figure 5.19, lower right panel). Continuing the simulation of this model further, the shock radius is reduced so far that a new phase SASI spiral and sloshing motions sets in, which dies again analogously to the first phase of revived SASI activity. Finally, we follow the hydrodynamic evolution of the supernova core even into

a third phase with an increasing and again shrinking shock surface and revived SASI activity. We argue that this interesting behavior of the postshock flow recurs repeatedly at later postbounce times, but is never sufficient for pushing out the shock far enough.

At the termination of the simulation of the $20 M_{\odot}$ progenitor (~ 425 ms after bounce) a similar behavior can be observed. In the last ten milliseconds the shock surface starts to expand again because of revived SASI sloshing and particularly spiral motions. While the once again active SASI is not yet reflected in an increase of the respective SASI coefficients (Figure 5.7), the deformation of the shock surface (Figure 5.8) as well as the kinetic energy in angular directions (Figure 5.9) is already larger. Unfortunately, because of limited availability of computer time resources, a phase of revived SASI activity could be not tracked completely.

5.5 Runaway Conditions and Explosion Indicators

As discussing the outcome of our set of 2D simulations in Section 3.3 favorable conditions of the gain layer can be determined by ratio $\tau_{\text{adv}}/\tau_{\text{heat}}$ (Janka 2001; Thompson et al. 2005; Fernández 2012). This runaway criterion is depicted in Figure 5.6 and reflects the different evolution of 2D and 3D runs of the $27 M_{\odot}$ SN progenitor and the $20 M_{\odot}$ SN progenitor. Prior to the infall of the Si/SiO shell interface through the shock the hydrodynamic conditions in the postshock flow are similar, while afterwards both progenitor models are more optimistic for ~ 80 ms in the 3D case. The timescale ratio of $20 M_{\odot}$ SN progenitor reaches 0.8 and thus is close to the critical value of unity in 3D. However, lateron both 3D models become continuously more pessimistic, while the 2D models exceed the threshold criteria and go on to explode.

Favorable conditions for an explosion are directly connected with the strength of SASI activity in our models. Large-scale mass motions associated with sloshing and spiral shock motions can stabilize the amount of mass in the gain layer (Figure 5.20, bottom panels), stopping the contraction of the shock surface at $t \sim 210$ ms for the $27 M_{\odot}$ progenitor model and at $t \sim 170$ ms for the $20 M_{\odot}$ progenitor model. At this point SASI activity allows more mass in the gain layer to be accumulated by pushing the shock outwards and thus extending the gain layer. Since the SASI is even stronger in 3D (Figure 5.7), the content of mass between the gain radius and the shock surface that can be heated by neutrino energy deposition becomes larger compared to 2D. While initially the extension of the shock surface is larger in 2D for the $20 M_{\odot}$ progenitor model, the amount of mass can be maintained in 3D for more than 100 ms and thus, more mass is exposed to neutrino heating than in 2D in this time period. As we observed in Hanke et al. (2012) in a parametric study, the postshock volume of models closer to an explosion is more extended and thus the accumulated mass behind the shock surface is higher. This is a further support that our 3D models are at least for certain periods of time more favorable than the corresponding 2D run. However, when the SASI dies off (see Section 5.2), the shock radius and the gain layer shrinks. On the contrary, at the onset of the explosion more and more mass is accumulated behind the expanding shock surface in the 2D case.

The effect of the different strength of SASI activity on the situation of the gain layer in 2D and 3D is reflected similarly by the time matter can stay in the gain layer, i.e. the dwell time

5. SASI Activity and Convective Overture in Fully Self-consistent 3D Core-Collapse Supernova Simulations

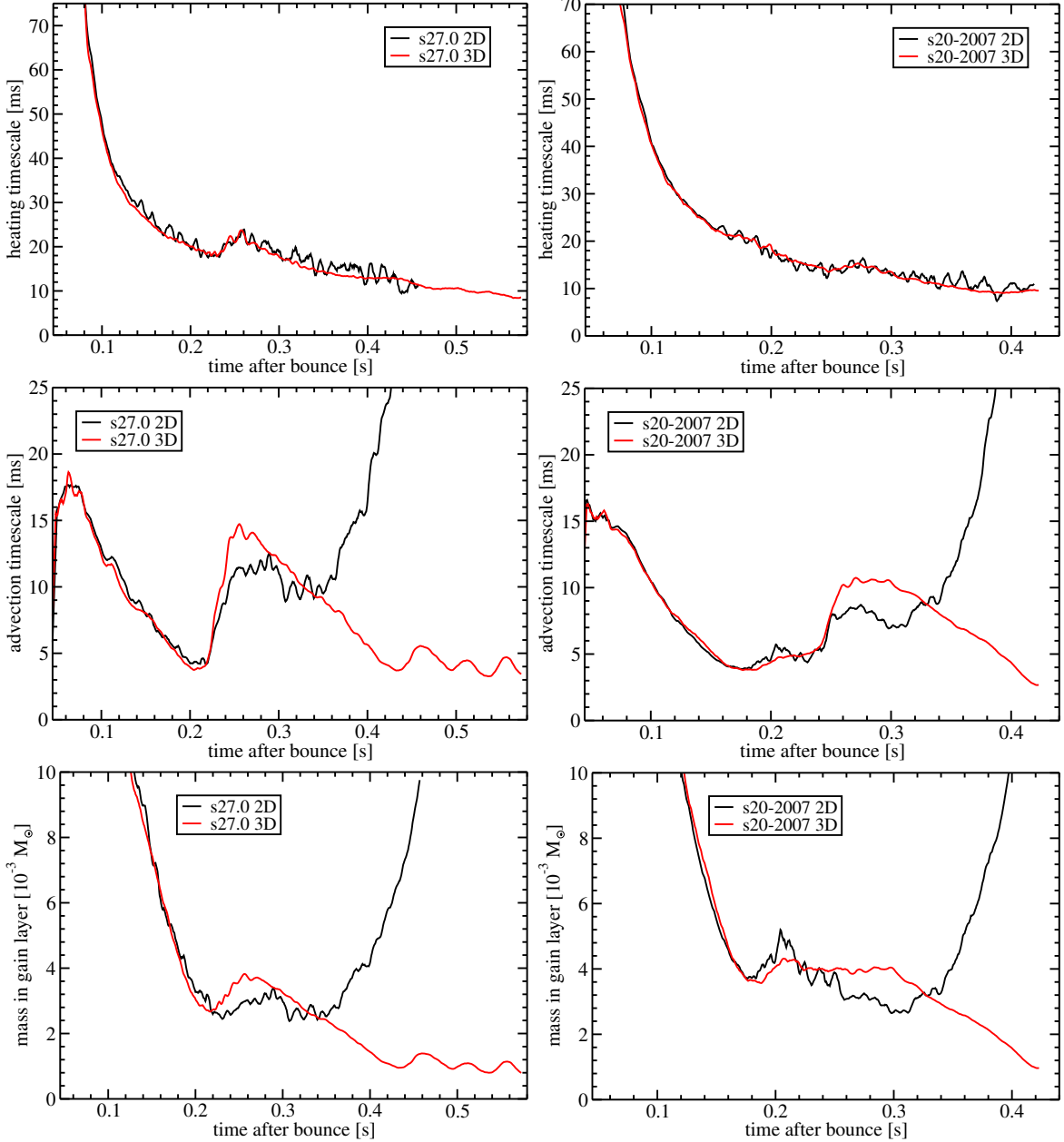


Figure 5.20: Time evolution of diagnostic quantities for the conditions in the gain layer for the $27 M_{\odot}$ SN progenitor (left panel) and the $20 M_{\odot}$ SN progenitor (right panel). The 3D results (red) are shown together with the corresponding 2D run (black). The heating timescale (top), the advection timescale (middle), and the mass in gain layer (bottom) are shown. Note that the curves have been smoothed using a running average over 5 ms. The advection timescale as well as the mass in the gain layer evolves more optimistic in 3D case for some time after the arrival of the Si/SiO composition-shell interface at the shock.

of matter, since a larger value of τ_{adv} correlates with a higher mass M_{gain} as $\tau_{\text{adv}} \approx M_{\text{gain}}/\dot{M}$ holds (see Section 3.3 and cf. Marek & Janka 2009). As depicted in Figure 5.20 (middle panels) indeed the dwell times of matter in the gain layer are longer for certain periods in our

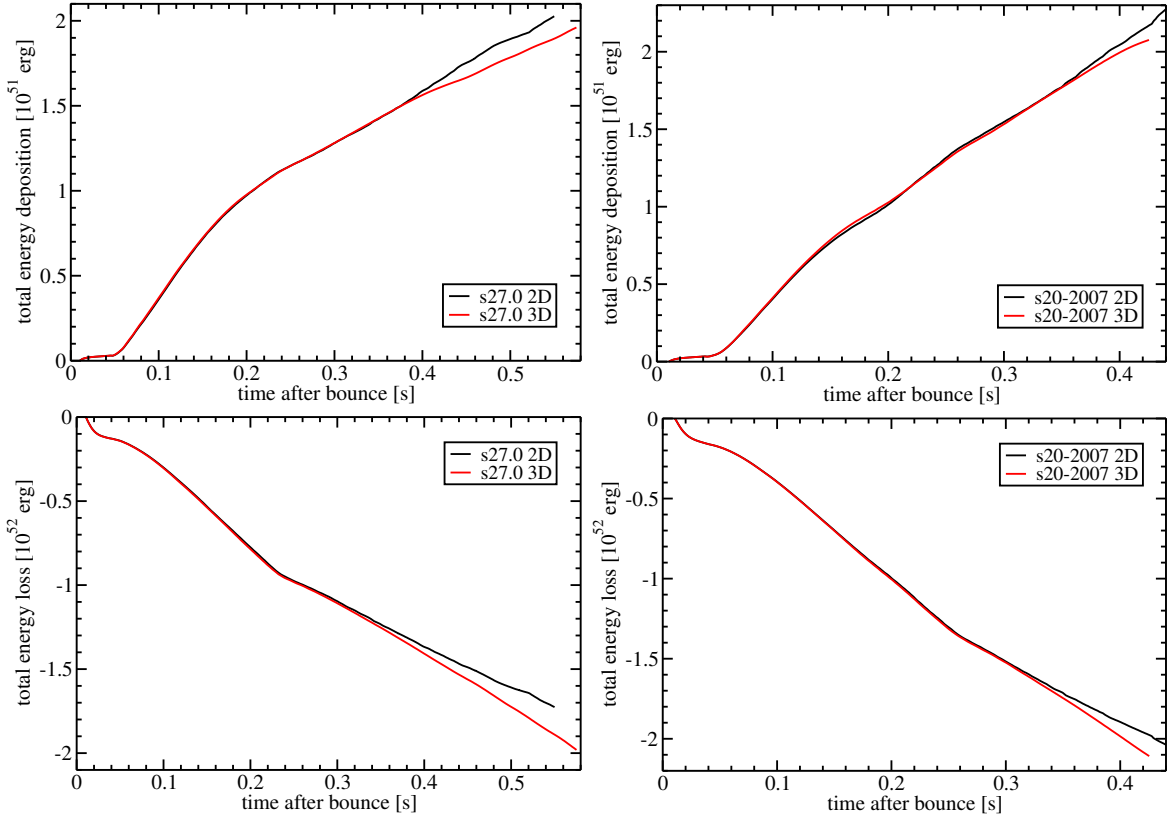


Figure 5.21: Time evolution of the total (time-integrated) energy deposited in the gain region (upper panel) and of the total energy loss (lower panel) for the $27 M_{\odot}$ SN progenitor (left panel) and the $20 M_{\odot}$ SN progenitor (right panel). The 3D results (red) are shown together with the corresponding 2D run (black). After the 2D models start to explode the corresponding 2D and 3D curves diverge.

3D simulations after the respective arrival of the Si/SiO shell interface at the shock.

While the dynamics of the postshock flow are substantially different in 2D and 3D, interestingly, both in 2D and in 3D, neutrinos are heating up the gain layer and cooling the region in front of the neutron star each with the same strength as depicted in Figure 5.21. Merely, after the 2D models develop an explosion, neutrino heating in 2D is stronger because of a smaller gain radius, where neutrino-energy deposition is maximal. Since the neutrino energy deposition rate scales with $L_{\nu_e} \langle E_{\nu_e} \rangle^2$ according to Equation 3.9 noted in the discussion of our set of 2D models in Section 3.3, the equal strength of neutrino heating is reflected in a very similar time evolution of the neutrino luminosity and mean energy shown in Figure 5.22 and Figure 5.23 for both progenitors. Both curves of each neutrino quantity are lying perfectly on top of each other prior to the explosion of the 2D models. Accordingly, the heating timescale (Figure 5.20, upper panels) evolves similar in 2D and 3D and no effect of avoiding the artificial symmetry restriction can be detected.

Finally, we want to stress that the late time periods of revived SASI activity discussed in Section 5.4 are too weak for pushing the shock outwards because of the very small amount of mass that can be heated up by neutrinos and the very small dwelling time of matter in

5. SASI Activity and Convective Overtur in Fully Self-consistent 3D Core-Collapse Supernova Simulations

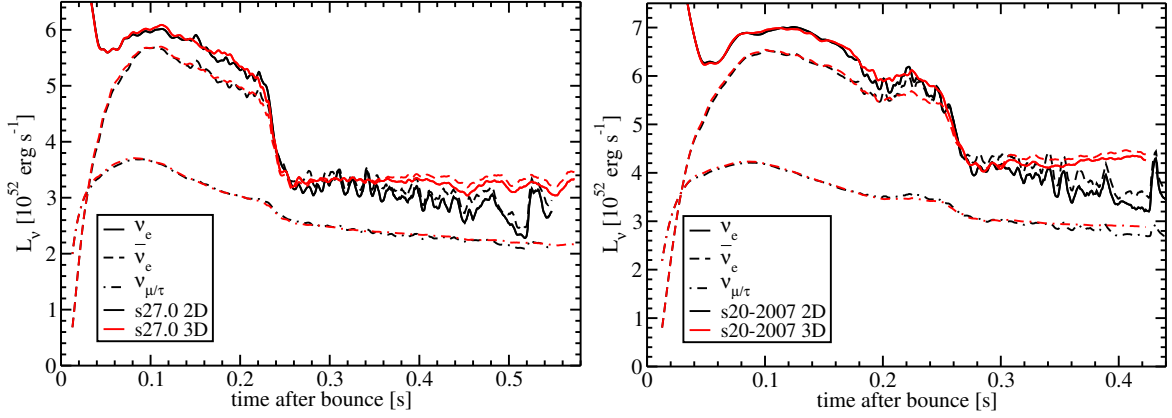


Figure 5.22: Time evolution of the neutrino luminosities (ν_e solid, $\bar{\nu}_e$ dashed, and $\nu_{\mu/\tau}$ dashed-dotted) as function of time after bounce for the $27 M_\odot$ SN progenitor (left panel) and the $20 M_\odot$ SN progenitor (right panel). The 3D results (red) are shown together with the corresponding 2D run (black). Note that the curves have been smoothed using a running average over 5 ms. Until the onset of explosion of the 2D models, the neutrino luminosities evolve equally in 2D and 3D for both progenitors. Afterwards, the neutrino luminosities for the 2D models is reduced, while they remain almost constant in the 3D case.

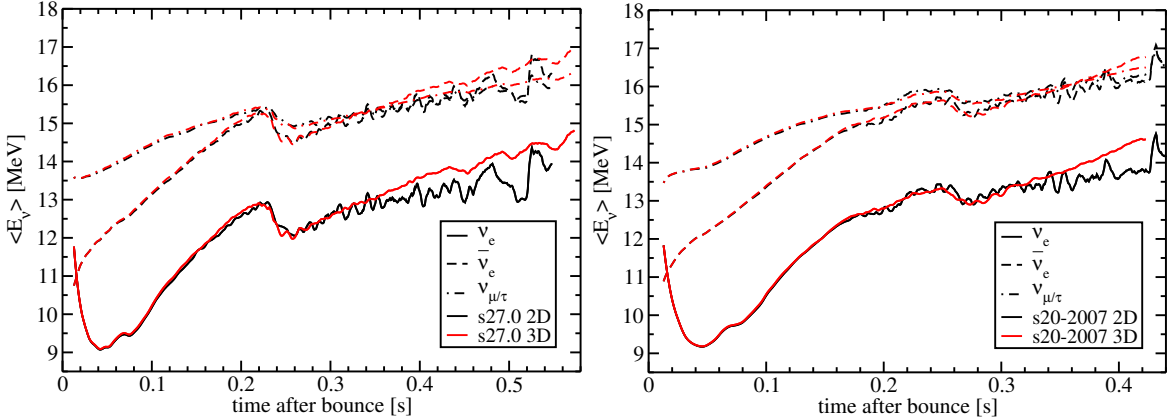


Figure 5.23: Time evolution of the neutrino mean energies (ν_e solid, $\bar{\nu}_e$ dashed, and $\nu_{\mu/\tau}$ dashed-dotted) as function of time after bounce for the $27 M_\odot$ SN progenitor (left panel) and the $20 M_\odot$ SN progenitor (right panel). The 3D results (red) are shown together with the corresponding 2D run (black). Note that the curves have been smoothed using a running average over 5 ms. Until the onset of explosion of the 2D models, the neutrino mean energies evolve equally in 2D and 3D for both progenitors. Afterwards, the increase of the mean energies for the 2D model is reduced, while they rise steadily in the 3D case.

the gain layer. Thus, at very late times of our 3D simulations neutrino heating cannot be sufficient anymore to heat enough matter for a powerful shock expansion.

5.6 Turbulent Mass Motions and the Rise of Buoyant Plumes

Let us now turn to the most important issue in the two presented 3D simulations of the $27 M_{\odot}$ and the $20 M_{\odot}$ progenitor: The failure of an explosion in 3D. While the corresponding 2D simulations can maintain shock expansion even at larger shock radii towards developing an explosion, there is a fixed distance from the center of the supernova core at around 220 km for both models, which cannot be passed by the 3D shock surface. At this radius SASI activity ceases in 3D, because the advective-acoustic time of a SASI cycle scales with the advection time (Foglizzo et al. 2007), which increases for an extended shock surface and a higher amount of accumulated matter in the gain layer (Figure 5.20). The advective-acoustic cycle breaks down when pushing the shock sufficiently far out (Figure 5.5 and 5.7). However, the 2D model maintains large, albeit less regular, shock oscillations with the shock radius pushing continuously out. Are the violent sloshing motions responsible for driving the explosion in the 2D simulations an artifact of the artificial symmetry restriction as argued by Burrows et al. (2012) and Dolence et al. (2013) on the basis of simplified simulations? This argument is further supported by the strong, prolate deformation of our successful 2D explosions of Chapter 3 enabling the shock outwards along the artificial symmetry axis. Because of this geometric effect a much smaller amount of mass in the gain layer has to be initially pushed out in 2D for launching the explosion.

In the framework of our parametrized models based on simple neutrino heating and cooling source terms we have observed in Hanke et al. (2012) that mass motions on the largest possible scale rather than the small scales are the actual driving agent for a successful neutrino-driven explosion. Indeed, inspecting the volume rendering visualization of the entropy distribution of our 3D models in Figures 5.1 and 5.2 for the $27 M_{\odot}$ and in Figures 5.3 and 5.4 for the $20 M_{\odot}$ progenitor, one can prove that the shock is driven outwards once a sufficiently large high-entropy bubble has formed typically by SASI sloshing motions, while shock recession is associated with a progressing fragmentation of the postshock flow. Thus, the question of successful revival of the shock seems to be tightly linked to the ability of the postshockflow to generate powerful coherent mass motions.

In this context, the more favorable outcome of the 2D model is connected to the fundamentally different nature of turbulence in 2D and 3D, which has been suggested to play a crucial role in the postshock dynamics in multidimensional simulations (Murphy & Meakin 2011; Murphy et al. 2013). The opposite action of turbulence manifests as a consequence of the “inverse” turbulent energy cascade (Kraichnan 1967), which pumps turbulent energy fed into the flow by external sources from small to large scales in two dimensions, while in three dimensions turbulent energy is redistributed to smaller scales. Neutrino energy deposition as well as potential energy released by accreted matter falling through the supernova shock are sources, which supply the postshock flow with additional energy.

The different character of the turbulence energy distribution in 2D and 3D can be studied by computing the kinetic energy spectrum $E(k)$ of turbulent motions as a function of wavenumber k in the gain region. The spectral shape of $E(k)$ can already be adequately established by considering only the azimuthal velocity v_{θ} at a given radius using a decomposition into

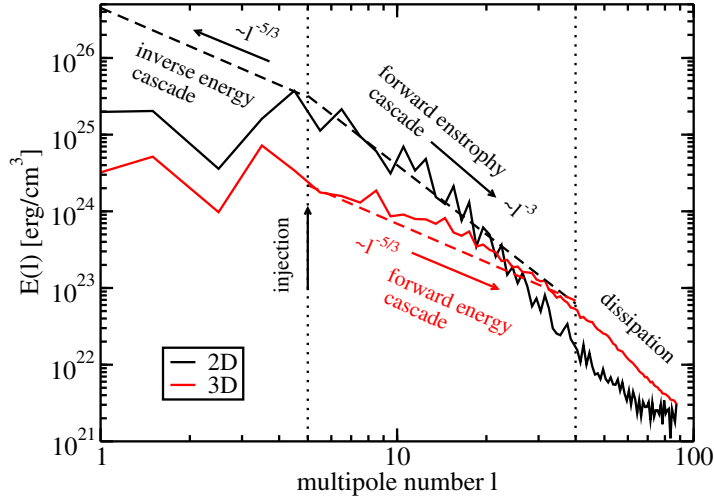


Figure 5.24: Turbulent energy spectra $E(l)$ as functions of the multipole order l . The spectra are based on a decomposition of the azimuthal velocity v_θ into spherical harmonics at radius $r = 120$ km and 300 ms post-bounce time for $27 M_\odot$ SN progenitor. The 2D model is depicted by the black curve and the 3D model by the red curve. The power-law dependence and direction of the inverse energy and forward enstrophy cascades are indicated by black dashed lines and labels for 2D and the shifted forward energy cascade by a red dashed line for 3D. The left vertical, dotted line roughly marks the energy-injection scale, and the right vertical, dotted line denotes the onset of dissipation at high l for the employed resolution.

spherical harmonics $Y_{lm}(\theta, \phi)$:

$$E(l) = \sum_{m=-l}^l \left| \int_{\Omega} Y_{lm}^*(\theta, \phi) \sqrt{\rho} v_\theta(r, \theta, \phi) d\Omega \right|^2. \quad (5.10)$$

Here, the velocity fluctuations have been expressed in terms of the multipole order l instead of the wave number k . A summation over the energies of modes with the same l has been carried out, and in order to obtain smoother spectra, we average $E(l)$ over 30 km in radius and over 5 ms. One expects that the resulting spectrum $E(l)$ directly reflects the properties of $E(k)$ such as the slopes in different regimes of the turbulent cascade (Hanke et al. 2012).

The computed spectra $E(l)$ displayed in Figure 5.24 are evaluated at ~ 300 ms after bounce, when the shock position of the 2D and 3D model is similar, and at 120 km somewhat behind the shock. The shape of the obtained spectra indeed confirms the different character of turbulence in 2D and 3D. At wavenumbers around $l = 5$ kinetic energy is injected into the postshock flow. For our neutrino-hydrodynamic simulation of the $27 M_\odot$ progenitor this driving scale, which is typical of the order of a convective plume, is chosen smaller compared to Hanke et al. (2012), because the typical size of a convective bubble is smaller for the full-scale models presented here with a significantly shrunked shock radius. In the 3D model, beginning at the injection scale, the energy spectra is consistent with a characteristic power-law of the forward energy cascade with $E(l) \propto l^{-5/3}$ (Landau & Lifshitz 1959) transporting energy to smaller scale until dissipation sets in at large l . Contrary, the 2D spectra roughly follows a different power-law with $E(l) \propto l^{-3}$ consistent with turbulence theory (Kolmogorov

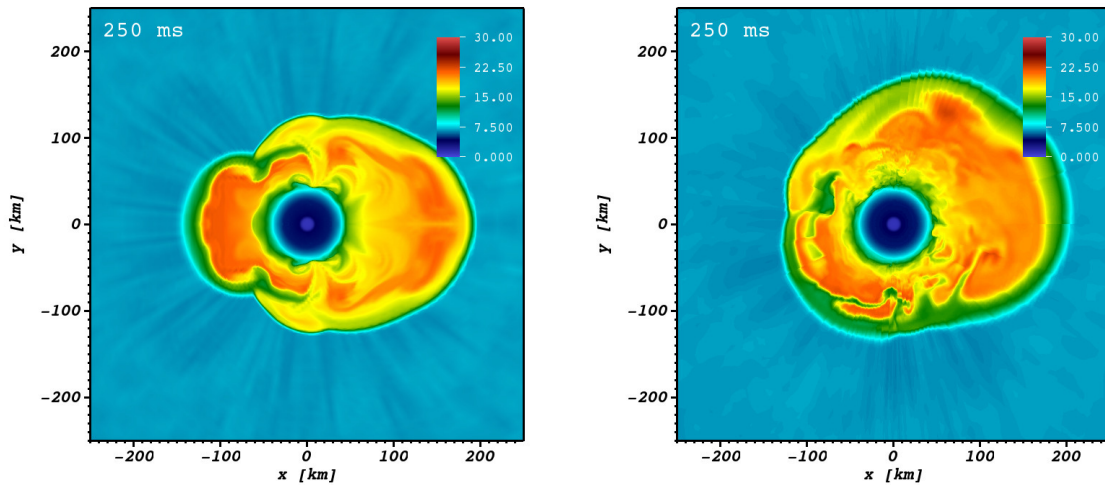


Figure 5.25: Snapshots of the entropy per baryon s in the $27 M_{\odot}$ progenitor at 250 ms after bounce, when the shock surface of the 3D model reaches its maximal extension. In the left panel the 3D model is depicted in the plane of former SASI activity, while 2D model mirrored at the symmetry axis is shown in the right panel. At this particular time the 3D shock surface is further enlarged than the corresponding 2D case. The imprint of SASI activity is visible in both snapshots, although the entropy structure of the 3D model is more fragmented into fine-structured convective plumes.

1941; Kraichnan 1967), although only enstrophy, the squared vorticity of the velocity field, is transferred to the dissipation range in this so-called forward cascade. Instead, energy is transported in 2D towards large by the reverse energy cascade (Kraichnan 1967). In our self-consistent 2D model, the energy cascade towards large scales deviates from the power-law of the expected power law as symbolized in Figure 5.24, because SASI activity dominates convection at least at the largest scales of the postshock flow. Analogously, the energy cascade towards dissipation at high multipole number is not fully established, because convection with vortices acting towards smaller scales has not completely developed and is engulfed partially by SASI activity.

Our analysis of the turbulent energy spectra reflects the observation that the amount of kinetic energy accumulated in the fluid motion on the largest possible scales is crucial to assist the development of an explosion by the neutrino-heating mechanism. Figure 5.24 proves that there is much more energy at large scales (actually from the highest order up to $l = 20$) in 2D, while the turbulent energy stored in the nonradial flow in our 3D model is dominant at small scales ($l > 20$ towards dissipation). This evidence provides a natural explanation of the finally more optimistic outcome of our 2D models and the maintainance of the SASI activity at larger shock radius in 2D, while in 3D SASI activity ceases and the model fails to explode.

The inspection of color coded snapshots of the entropy distribution confirms the importance of large-scale mass motions to foster the explosion (Hanke et al. 2012). Although at first glance the convective structures of the postshock flow are fairly similar in 2D and 3D, in Figure 5.25 and Figure 5.26 the pattern of convection and turbulence in the 3D case incorporates more

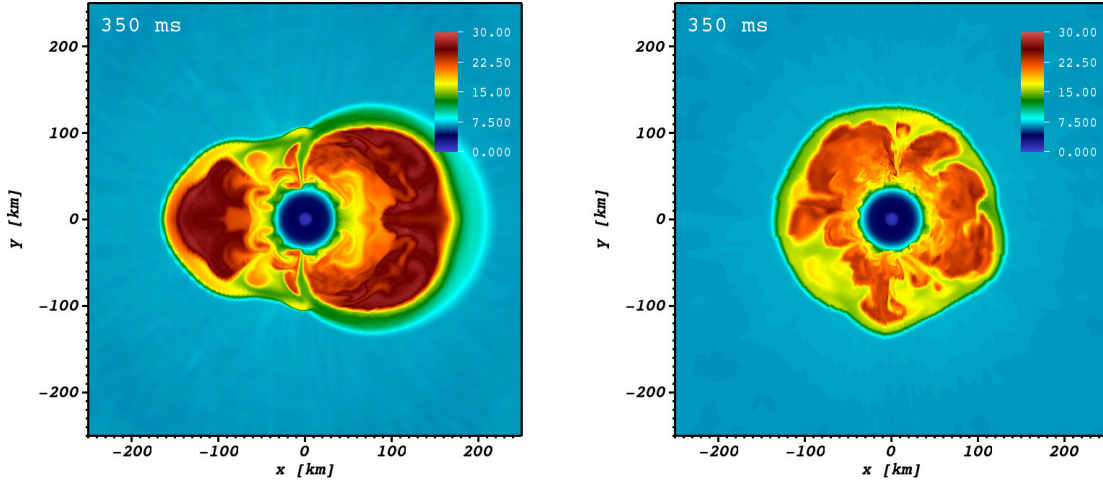


Figure 5.26: Analogous to Figure 5.25, snapshots of the entropy per baryon s in the $27 M_{\odot}$ progenitor at 350 ms after bounce, shortly before the onset of the explosion in the 2D case. The convective plumes are considerably smaller in 3D, while the 2D entropy distribution is dipolar and dominated by two large buoyant plumes along the axis.

small structures and is fragmented into fine-structured plumes. When the SASI activity ceases at around ~ 250 ms after bounce in the 3D case, a large region of the postshock flow is still dominated by a coherent entropy structure (Figure 5.25). Nevertheless, the turbulent energy cascade distributes more energy to small spatial scales in 3D resulting into a growing variety of small vortex structures and finer filaments at least in some parts of the flow. In the next hundred milliseconds, this progress continues such that the 3D flow consists of an increasing number of small buoyant plumes and fine filaments (Figure 5.26). Instead, the evolution of the postshock flow in the 2D model is dominated by a dipolar low-mode structure with two large, buoyant plumes behind the SASI deformed supernova shock along the artificial symmetry axis. Small scale structures are almost not visible in clear contrast to the 3D case. Indeed, Figure 5.26 demonstrate that the shock is successfully pushed out by the continuous expansion of one dominant large buoyant bubble leading to an explosion (see also the discussion of the representative 2D model “s12-2007” in Section 3.7).

Discussing the snapshots of the entropy distribution in Figures 5.25 and 5.26, we inevitably encountered that SASI activity is not sufficient to finally launch an explosion. Since the growth conditions of the SASI are inverse dependent on the shock radius (see Section 3.5), the SASI ceases after sloshing motions have pushed out the shock surface sufficiently out as observed for both 3D models of the $27 M_{\odot}$ as well as the $20 M_{\odot}$ progenitor. While driven by buoyancy a large plume is able to grow in size along the symmetry axis in 2D, in our 3D simulations the dominant bubble behind the SASI deformed shock visible in the volume rendering images of the postshock distribution (Figures 5.1, lower right panel for $27 M_{\odot}$ progenitor and Figures 5.4, lower left panel for $20 M_{\odot}$ progenitor) stops to expand at a certain radius. Assuming the hydrodynamic flow behind the stalled shock is dominated by buoyancy-driven convection (Burrows et al. 2012; Murphy et al. 2013), one can roughly describe shock

expansion by an interplay between the buoyancy force rising a convective plume upwards and the drag force exerted by the postshock accretion flow (Dolence et al. 2013). In this context, the size of a buoyant bubble depends on the competition between neutrino-heating and the energy loss by the interaction between the bubble and the surrounding flow. If neutrino-heating is dominant over the repulsive force of the accretion flow a bubble grows and thus rises pushing the shock locally outwards. How is such a picture of buoyancy-driven growth of bubbles helpful in distinguishing our 2D and 3D models? According to Couch (2013) the buoyancy force of a bubble is proportional to its volume, while the drag force on the bubble depends on the surface area of the bubble. Thus, larger bubbles rise faster than smaller, because the ratio of both forces is more favorable for a larger bubble size. Figures 5.25 and 5.26 clearly demonstrate that in 2D buoyant plumes have much smaller surface area-to-volume ratios than in 3D, because the 3D hydrodynamics flow consists of numerous small convective bubbles, whereas the artificial symmetry results in large bubbles in 2D. Thus, the 3D convective structures experience a greater drag-to-buoyant force ratio hampering the rise of plumes and consequently shock expansion.

In the framework of a buoyancy-dominated shock expansion overtaking the initial SASI driven shock revival, shock expansion is fostered by the growth of large buoyant plumes. For several reasons, as the forward turbulent energy cascade to smaller scales and the unfavorable ratio of surface area-to-volume ratio of a plume, the growth of bubbles in 3D is obviously less favorable than in 2D. This issue provides a natural explanation of failing explosions of our 3D simulations, while the corresponding 2D runs explode marginally. Using a neutrino leakage scheme, the results of Couch & O’Connor (2013) are in line with our observations, since their 3D models explode only if the neutrino heating energy deposition rate is increased artificially by more than 10% compared to 2D. In this spirit, we argue that the neutrino energy deposition calculated by full up-to-date neutrino interaction rates of the VERTEX-PROMETHEUS code is insufficient to compensate the hampering influence of the 3D hydrodynamics.

5.7 Discussion and Conclusions

We have simulated the post-bounce evolution of the $27 M_{\odot}$ progenitor of Woosley et al. (2002) and of the $20 M_{\odot}$ progenitor of Woosley & Heger (2007) in 2D and 3D, using the VERTEX-PROMETHEUS code with detailed multi-group neutrino transport including the full, sophisticated set of neutrino reactions applied previously for our 2D simulation set discussed in Chapter 3.

Our simulations for the first time provide unambiguous evidence of the occurrence of large-amplitude SASI shock sloshing and spiral motions and of their interplay with neutrino-driven convection in 3D supernova core environments modeled with a “realistic” treatment of neutrino transport and the corresponding heating and cooling effects. Previous hydrodynamic studies have been able to identify SASI activity, and in particular SASI spiral modes, only in 3D setups with adiabatic postshock accretion flows (Blondin & Mezzacappa 2007; Fernández 2010) and in some simulations with a simple neutrino light-bulb treatment (Iwakami et al. 2008, 2009). The shallow water analogue of the SASI was also observed experimentally, however again without the presence of buoyancy motions (Foglizzo et al. 2012). On the basis of more recent 3D simulations with a simple neutrino light-bulb approximation (Burrows et al.

2012; Murphy et al. 2013; Dolence et al. 2013) and 3D general relativistic models with a neutrino leakage scheme (Ott et al. 2013) it was even concluded that the SASI is at most of minor relevance for the dynamics of the postshock layer in collapsing stellar cores (see also Burrows 2013).

Our findings indicate that the SASI is potentially much more important in 3D than suggested by these previous investigations. Besides the core-density profile of the progenitor star, which determines the temporal evolution of the mass infall rate, the more elaborate neutrino transport treatment may partly be responsible for the different accretion-flow dynamics seen in our models. The details of the neutrino description are relevant, because they can cause differences in the contraction behavior of the proto-neutron star and in the neutrino-heating in the gain layer. Both affect the evolution of the stagnation radius of the accretion shock and thus have a strong impact on the growth conditions for convection and the SASI. In the artificial setup used by Burrows et al. (2012); Murphy et al. (2013); Dolence et al. (2013), the neutron star is not allowed to deleptonize and radiate energy, therefore its radius stays unrealistically large (50–60 km) during the whole simulated postbounce evolution (up to ~ 1 s). Also the leakage scheme of Ott et al. (2013), which can track the contraction of the proto-neutron star and the time evolution of the neutrino emission to a certain extent, deviates significantly from full transport models. For example, in the work of Ott et al. (2013) the mean energy of the radiated electron neutrinos around 100 ms after core bounce is more than 60% higher than those found with the VERTEX transport code by Müller et al. (2012a), although both groups investigated the same $27 M_{\odot}$ progenitor with relativistic methods. It is clear that the neutrino heating found by Ott et al. (2013) was stronger and thus more favorable for larger shock radii, which in turn was supportive of neutrino-driven convection instead of the SASI.

In contrast to the findings by Burrows et al. (2012); Murphy et al. (2013); Dolence et al. (2013) and by Ott et al. (2013), we observe strong SASI activity in our 3D simulations both for the $27 M_{\odot}$ progenitor and the $20 M_{\odot}$ star. The SASI can become the strongest nonradial instability during at least some parts of the evolution and can be clearly identified by its oscillatory growth properties and even in the nonlinear regime by its characteristic low-order spherical harmonics modes of coherent shock motion and shock deformation. In detail, we can draw the following conclusions from our models:

- SASI activity can develop in 3D despite and in addition to the earlier presence of neutrino-driven buoyancy. Different from the higher-order multipole pattern that is typical of convective plumes and downdrafts, the SASI reveals itself by coherent, large-amplitude shock sloshing and spiral motions.
- Because of the absence of a flow-constraining symmetry axis, which also directs the structure of neutrino-driven buoyancy in 2D models, SASI shock motions and deformation modes can be recognized more easily and more clearly in the 3D case. Interestingly, both the $27 M_{\odot}$ and the $20 M_{\odot}$ models exhibit evolution phases in which the SASI in 3D can become stronger than in the corresponding 2D runs. The dominance of the SASI and greater strength in 3D can be concluded not only from the large dipole and quadrupole amplitudes of the shock deformation, but also from the higher nonradial kinetic energy of the postshock flow (Figure 5.9) and from a prominent peak at low-order multipoles in the power spectrum of the nonradial kinetic energy (Figure 5.10). While some authors hypothesized (Iwakami et al. 2008) that the SASI amplitudes in 3D re-

main smaller than those in 2D because the kinetic energy of the nonradial flow is shared with an additional degree of freedom, our results suggest that there is no such limitation of the kinetic energy that can be stored in lateral and azimuthal mass motions. The fraction of the huge reservoir of accretion energy that is converted to nonradial flows in the postshock layer can be larger in 3D than in 2D.

- The growth of the SASI is favored by fast advection flows, because its growth rate in an advective-acoustic cycle scales roughly inversely with the advection timescale of the accretion flow from the shock to the neutron star surface (e.g., Scheck et al. 2008). This is opposite to neutrino-driven buoyancy, whose growth in the accretion flow requires that the critical ratio χ of advection timescale to buoyancy timescale exceeds a value of about 3 (Foglizzo et al. 2006). Fully consistent with this dimension-independent theoretical understanding, which was developed by linear analysis and hydrodynamic modeling in 2D, we find SASI growth also in the 3D case to be strongest in phases of small shock stagnation radii, which are connected to rapidly shrinking and more compact proto-neutron stars as well as relatively weak neutrino heating.
- Preferentially in phases of strongest shock recession we observe bipolar ($\ell = 1, m = 0$) SASI sloshing motions to change over to a spiral ($\ell = 1, m = 1$) mode in the 3D simulations of both the $27 M_{\odot}$ and $20 M_{\odot}$ models (Figures 5.14 and 5.15 as well as 5.16). The transition to the time-dependent rotating shock-deformation pattern therefore seems to be favored by particularly small shock radii as demonstrated clearly in the $20 M_{\odot}$ case with its much faster development of a spiral mode. In general, the character of the 3D accretion flow during shock oscillation and spiraling phases with wandering directions reveals close similarity to the behavior of the hydraulic jump observed in the SWASI experiment (Foglizzo et al. 2012).

Our comparison of the SASI activity in the fully self-consistent 2D and 3D simulations of the $27 M_{\odot}$ model as well as the $20 M_{\odot}$ progenitor is particularly interesting. Both models revealed that at an early stage, when the mass accretion rate is still high and the shock correspondingly retreats in response to the proto-neutron star contraction, the SASI can grow despite some prior neutrino-driven convective activity. The SASI can reach even higher amplitudes in 3D than in 2D before the accretion of the Si/SiO interface in the case of $27 M_{\odot}$ model and similarly, $20 M_{\odot}$ progenitor simulation shows a phase of stronger SASI activity in 3D, although at much later postbounce times. In the case of the $27 M_{\odot}$ progenitor, the large-amplitude shock-sloshing mode eventually makes the transition to a spiral mode in 3D, which, however, is quenched around 260 ms after bounce once the accretion rate has dropped significantly and the shock has expanded to radii of nearly 200 km on average. Because of faster shock recession prior to the infall of the Si/SiO interface, a spiral modes develops faster and persists much longer in the case of the $20 M_{\odot}$ progenitor until around 290 ms, when the shock surface has reached its maximal prolongation. Despite the faster shock expansion and higher kinetic energy of the postshock flow, the 3D models of both progenitors nevertheless falls short of an explosive runaway unlike the 2D simulation.

Following shock recession of our 3D model of the $27 M_{\odot}$ progenitor to later and later postbounce times, the advection timescale of matter becomes such short (Figure 5.20, middle panels) that the conditions for the advective-acoustic cycle feeding the SASI are favorable again. Coherent mass motions are showing up again, which are resulting in a fast spiral SASI

mode. After the shock is pushed out by some extent, the revived phase of SASI activity is over again. Although we track several such phases of late-time SASI activity, the extension of the shock remains always at small radii. This interesting phenomenon is not powerful enough anymore for initiating an explosion lateron.

The important difference in the explosion behavior of 2D and 3D models, which is fully consistent with the results obtained in the simulations with simple neutrino heating and cooling treatments of Hanke et al. (2012) and Couch (2013), is remarkable. Although the relevance of the SASI in competition with neutrino-driven convection for getting explosions in 3D can be identified only by the means of a rigorous analysis, particularly a Fourier decomposition of the turbulent flow (Fernández et al. 2013), we have discussed possible reasons for the failing explosions of our 3D models in respect to the successful 2D models. It seems that the presence of SASI activity is only temporary and that neutrino-driven convection must dominate when the explosion sets in and the preceding shock expansion leads to disfavorable conditions for the advective-acoustic cycle feeding the SASI. That observation is the only plausible explanation why the SASI driven shock expansion stops in 3D. Even in the latter case, the SASI could still play an essential role in the explosion mechanism by pushing out the shock far enough for convection to take over in cases where convection cannot develop on its own in an initially stabilized post-shock flow.

As observed by Fernández et al. (2013); Hanke et al. (2012); Couch (2013), in successful axisymmetric models large-scale, high-entropy bubbles are driving the explosion, if they can survive sufficiently long. Indeed, such a large plume continuously grows in size driving the explosion of our 2D models (Figure 5.26 for the $27 M_{\odot}$ progenitor), while such large plumes are also visible, but they loose all of its energy while rising in the 3D case (Figure 5.25). We have identified two reasons why the growth of bubbles is damped in 3D:

- Turbulence in the hydrodynamic postshock flow with its opposite turbulent energy cascade in two and three dimensions acts differently. While in 3D the forward energy cascade transports energy to smaller and smaller scales until dissipation sets in, in 2D the inverse energy cascade erroneously transports energy pumped into the gain layer by neutrino heating and the release of gravitational binding energy from the injection scale to large scales. This behavior is evident in the energy power spectra of the postshock flow in 2D and 3D (Figure 5.24) and explains the easier growth of large buoyant plumes in 2D conducive to the explosion.
- The raise of buoyant bubbles is determined by the competition of the buoyancy force depending on neutrino heating and the drag force of the surrounding accretion flow. Under the assumption of neutrino-driven convection responsible for the bubble growth (Burrows et al. 2012; Murphy et al. 2013), shock expansion is mediated by the rise of a sufficient large buoyant bubble (Dolence et al. 2013). Since the ratio of buoyancy to drag force scales with the volume-to-surface area ratio of a plume (Couch 2013), such buoyant plumes with its increasing extension ascend easier and quicker pushing the shock outwards. While the imposed 2D geometry results in very large “3D” plumes of a toroidal structure, no such artificial coherent structures can exist in 3D. Moreover, the 3D postshock flow is typically fragmentated into much more bubbles on smaller structures, while a few, large-scale plumes along the symmetry axis are driving the explosion (Figure 5.25 and 5.26). Thus, the different convective structures of the postshock flow

with is hampering effect on the rise of bubbles in 3D provide a further explanation why our self-consistent 3D simulations are failing in respect to the marginal successful 2D case.

In future prospective sophisticated 3D supernova models one has to discover how the effects of the disadvantageous 3D flow geometry can be compensated by e.g. stronger neutrino heating to finally reproduce the successful explosions in previous axisymmetric simulations (see Chapter 3).

6 A Purely Convective model: The $11.2 M_{\odot}$ SN Progenitor

In this chapter we report about a further 3D hydrodynamic simulation, which we have performed with our detailed, energy-dependent, three-flavor neutrino transport code VERTEX-PROMETHEUS. The setup is the same in the previous simulations described in Section 5.1. In addition to the models discussed so far experiencing vigorous SASI activity, here we investigate the $11.2 M_{\odot}$ progenitor of the Woosley et al. (2002) presupernova series, which has been studied intensively in previous works (Buras et al. 2006b; Marek & Janka 2009; Müller et al. 2012b). As noted in the discussion of our set of two-dimensional simulations in Section 3.2, this star is particularly interesting because of its distinct presupernova structure compared to the more massive stars discussed in Chapter 5. Because the Si/SiO composition-shell interface of this progenitor arrives already at around 80 ms after bounce at the shock, the mass accretion rate is extraordinary low and the shock surface is extended to much larger radii compared to the other presupernova models in the first 120 ms of postbounce evolution (see left panel of Figure 3.3 in Section 3.2). Thus, we can expect that this model shows violent convective activity in the postshock flow, while SASI shock oscillations should be suppressed in this model because of the large advection timescales (see middle panel of Figure 3.7). The $11.2 M_{\odot}$ progenitor will provide more insight into the differences of the hydrodynamic postshock flow in 2D and 3D simulations and the resulting consequences for the explosion mechanism.

6.1 Shock Propagation and Heating Conditions

The 3D postbounce evolution of the $11.2 M_{\odot}$ progenitor is visualized by images of the entropy distribution in Figures 6.1 and 6.2. Triggered by initial seed perturbations, numerous mushroom-like, buoyant plumes have already developed at around 120 ms after bounce. At the early postbounce evolution, the growth of convective bubbles is significantly enhanced compared to the previously studied progenitor models in Chapter 5, because the shock radius increases to 200 km after the very early arrival of the Si/SiO composition-shell interface at the shock surface at around 90 ms after bounce (Figures 6.3). Mediated by neutrino heating, the initially small buoyant bubbles are rising and then successively replaced by larger ones. Such large bubbles rise until they reach the shock and push it outwards until 210 ms after bounce, when the shock has locally reached a maximum extension of 300 km at solid angles, where the largest bubbles have formed. The shock surface can be pushed out relatively far compared to the other two investigated progenitor models, because of the low amount of matter falling onto the supernova shock front (Figures 6.4). However, neutrino heating is not sufficient to finally push out the shock driving an explosion. Subsequently, the shock surface is shrinking slowly, but monotonically until the end of the simulation.

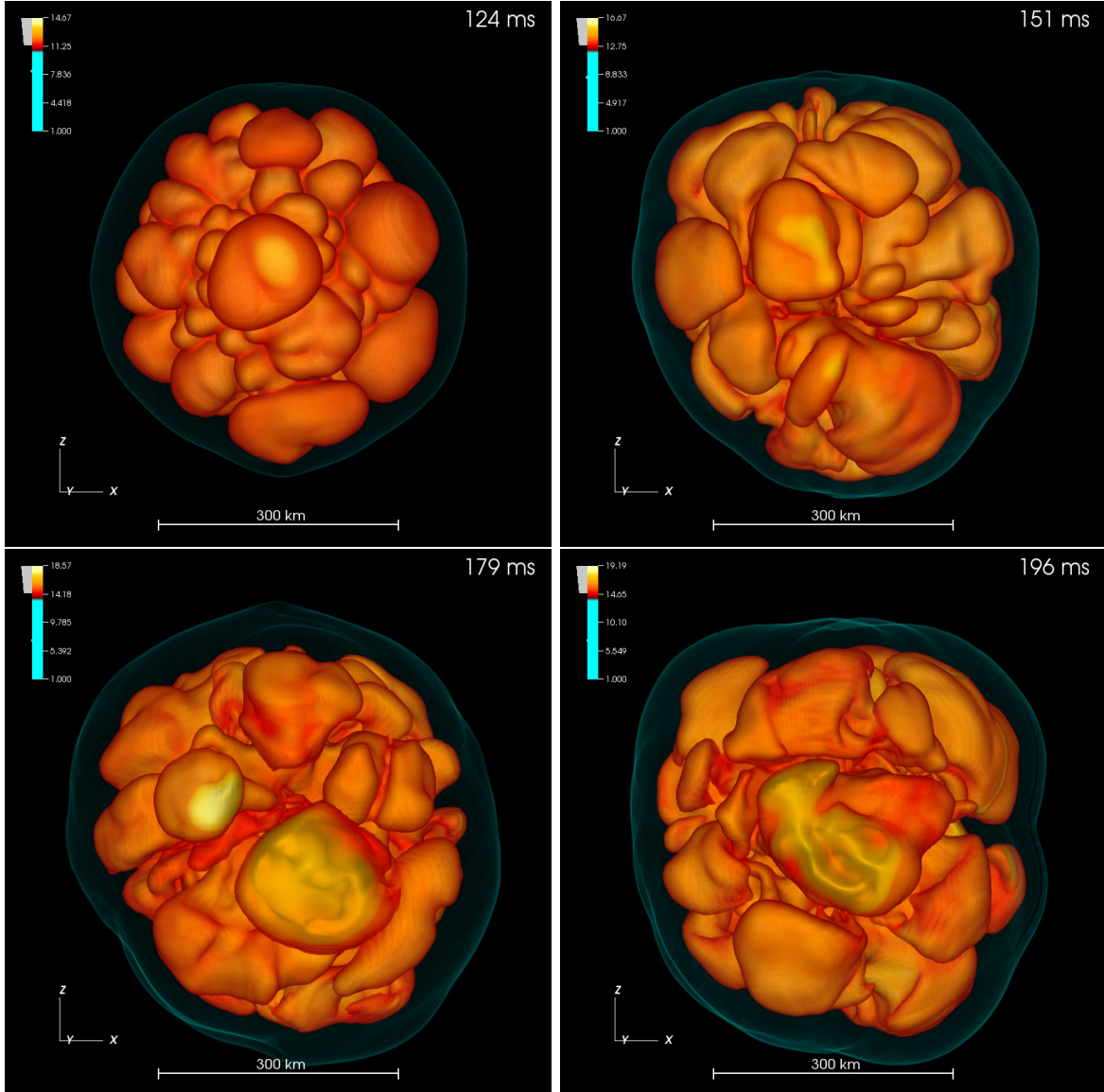


Figure 6.1: Snapshots of the convective overturn activity in the evolution of the $11.2 M_{\odot}$ progenitor at post-bounce times of 124 ms, 151 ms, 179 ms, and 196 ms. The volume rendering visualizes surfaces of constant entropy: The outer, bluish, semi-transparent surface is the supernova shock, the red-orange-yellow surfaces are entropy structures in the postshock region. In the upper left panel at 123 ms numerous mushroom-like, buoyant plumes have already developed. Neutrino-heated, high-entropy matter expands in typical mushroom-like, buoyant plumes pushing the shock surface to larger radii until 210 ms (upper right and both lower panels).

When we have stopped the 3D simulation of the $11.2 M_{\odot}$ progenitor, the postbounce dynamic is similarly pessimistic as the other 3D simulations presented in Chapter 5, while the corresponding 2D runs with identical numerical treatment (see Section 5.1) show large-amplitude shock oscillations amplified by the imposed artificial 2D geometry along the symmetry axis. Depicted in Figures 6.3, the shock trajectories evolve very similar in the first two hundred

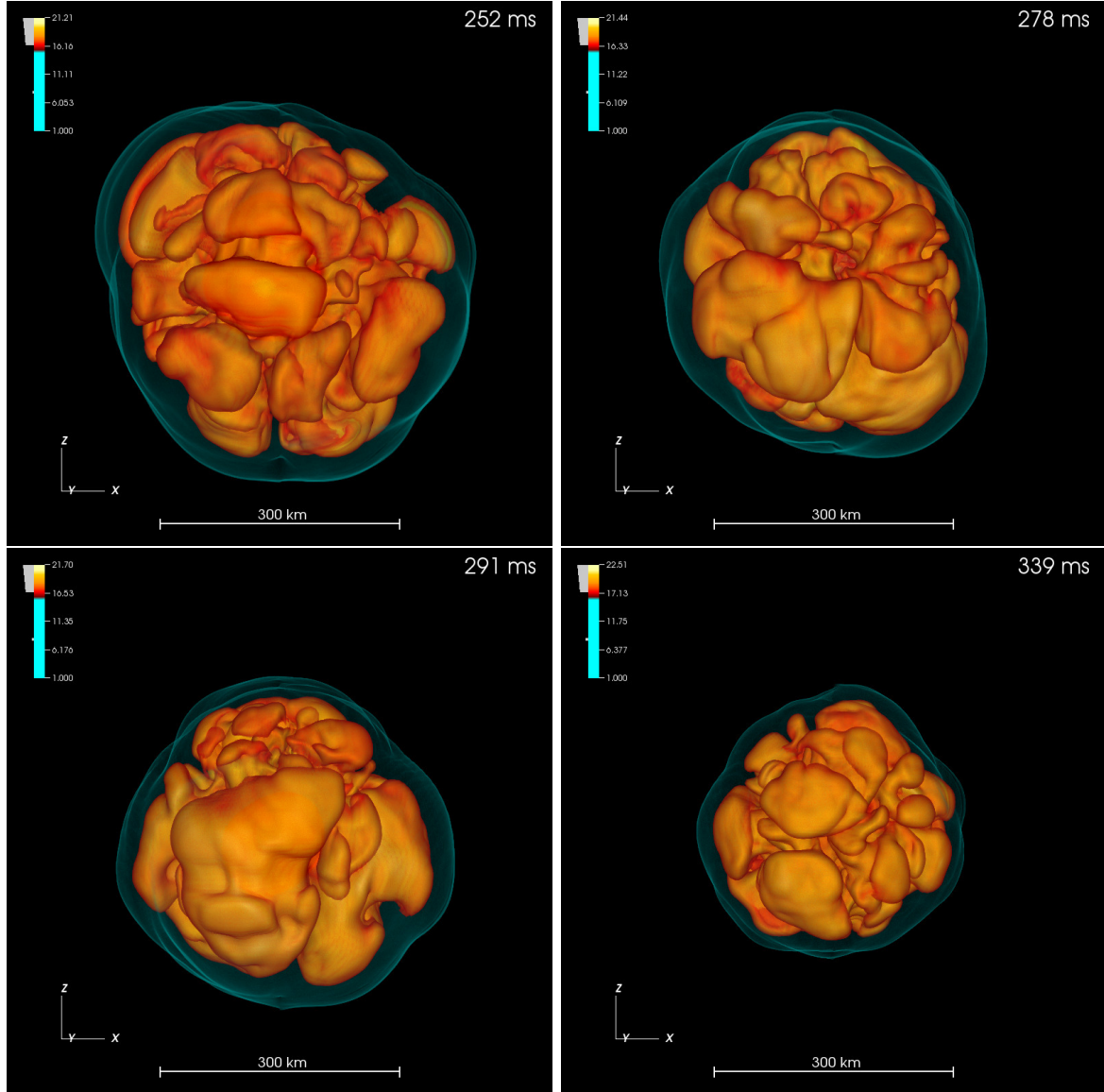


Figure 6.2: Further snapshots of the convective overturn activity in the evolution of the $11.2 M_{\odot}$ progenitor at post-bounce times of 252 ms, 278 ms, 291 ms, and 339 ms. Bubbles are continuously appearing, expanding and rising, but because of insufficient neutrino heating they are receding allowing other convective plumes to take its place. Subsequently, the shock surface is shrinking until the end of the simulation.

milliseconds after bounce in 2D and 3D, until in the axisymmetric model a first large bubble grows along one side of the symmetry axis, then is pushed back, and finally grows continuously in an oscillatory manner by time. Noticeable, the shock surface is increasing on one side, while most part of the matter is still at rest as the average shock radius does not yet rise accordingly.

The runaway criterion determined by the ratio $\tau_{\text{adv}}/\tau_{\text{heat}}$ (see Section 3.3 for the employed definitions of the advection and heating timescale) reflects the supposedly favorable conditions

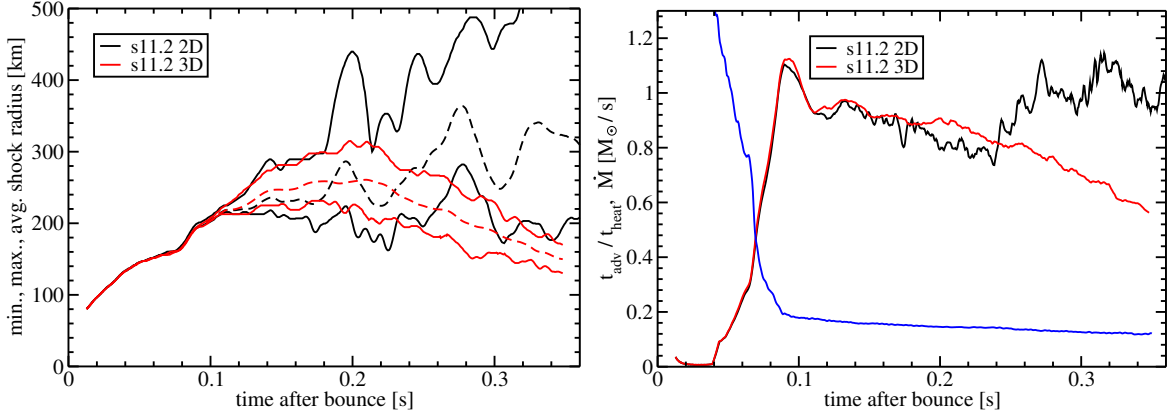


Figure 6.3: Time evolution of the minimum, maximum (solid line), and average (dashed line) shock radius as function of time after bounce for the $11.2 M_{\odot}$ SN progenitor. The 3D result is depicted by the red curve and the corresponding 2D run in black. Note that the curves have been smoothed using a running average over 5 ms.

Figure 6.4: Time evolution of the runaway criterion $t_{\text{adv}}/t_{\text{heat}}$ for the 2D (black) and 3D (red) simulations and the mass accretion rate of the stellar core at 400 km (blue) as function of time after bounce for the $11.2 M_{\odot}$ SN progenitor. The runaway criterion is smoothed using a running average over 5 ms.

of this progenitor (Figures 6.4). At the infall of the Si/SiO composition-shell interface at the shock surface at around 90 ms after bounce, the timescale ratio exceeds the threshold value of unity. Later on, the runaway criterion decreases with time almost continuously in the 3D simulation, which thus evolves very pessimistically. Contrary, the 2D model stabilizes its even more unfavorable evolution until a runaway situation is established at 370 ms after bounce. Depicted in Figure 6.5, the conditions of the gain layer provide further evidence of the particular situation in this presupernova model. Because of the very low mass accretion rate of the infalling matter on the shock, on the one hand the advection timescale is about 4–8 times higher than of the SASI dominated models of Chapter 5, and on the other hand the accretion part of the luminosity is accordingly much lower (Figures 6.7) and thus, the energy deposition of neutrino (Figures 6.6) results in a 2–4 times higher heating timescale. Choosing this progenitor one hopes that the very low ram pressure on the supernova shock can overcompensate the lower neutrino heating. Obviously, that is not the case. The gain layer monotonically loses its mass content and as $\tau_{\text{adv}} \approx M_{\text{gain}}/\dot{M}$ holds (see Section 3.3 and cf. Marek & Janka 2009), the advection timescale decreases in the same. However, as the heating timescale decreases more slowly, both timescale will never meet and a runaway situation cannot be established anymore. Fortunately, in 2D large-amplitude shock-sloshing motions along the symmetry axis can stabilize the amount of matter in the gain layer that can be heated up and the conditions for an explosion become more favorable until the explosion sets in.

In retrospective, this model might be not the optimal choice for one of our three 3D models, which were possible to simulate within our compute time grant. While this model was motivated by the previous works of Buras et al. (2006b); Marek & Janka (2009); Müller et al. (2012b), our the set of two-dimensional models in Section 3.2 provides more optimistic cases

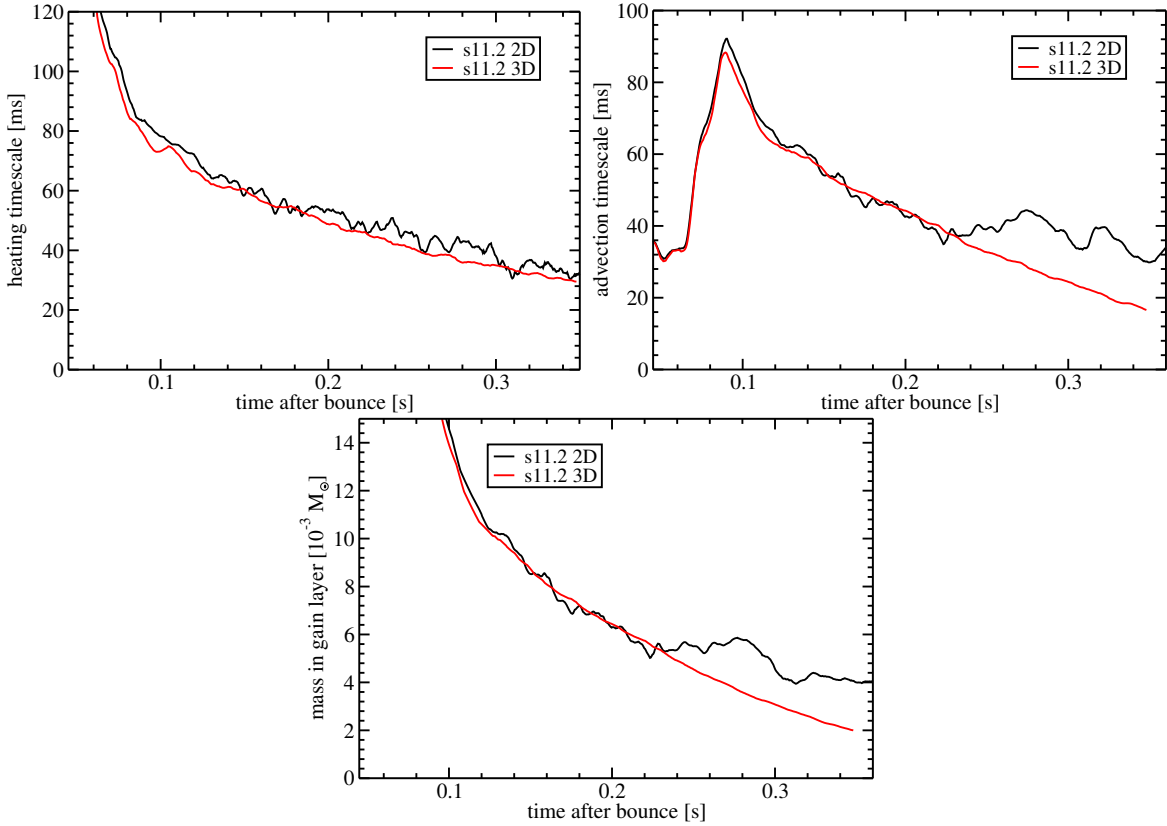


Figure 6.5: Time evolution of diagnostic quantities for the conditions in the gain layer for the $11.2 M_{\odot}$ SN progenitor. The 3D results (red) are shown together with the corresponding 2D run (black). The heating timescale (top), the advection timescale (middle), and the mass in gain layer (bottom) are shown. Note that the curves have been smoothed using a running average over 5 ms.

for a successful 3D explosion (e.g. “s18.4”, “s19.6”, and “s20.2”).

6.2 Growth of Convection and the Suppression of SASI Activity

While both 3D models presented in Chapter 5 show periods of vigorous SASI activity, the $11.2 M_{\odot}$ SN progenitor does not exhibit any clear evidence of SASI motions. The entropy structures of the postshock region visible in Figures 6.1 and 6.2 are typical for convective overturn driven by neutrino-heating. In this section we quantify the description of the postbounce dynamics in the $11.2 M_{\odot}$ model. A time-dependent decomposition of the shock surface into spherical harmonics as defined in Equation 5.1 reveals that the 3D shock surface indeed does not show any quasi-periodic oscillations typical for SASI activity (Figures 6.9). Although the 2D model experiences large shock oscillations, a dominant periodicity, which is typical for SASI dominated models (Fernández et al. 2013), is missing. This result is along our expectations of Section 3.5 as the growth rate of the SASI depends inverse on the advection timescale, which is not small enough for this model. Contrary, the large shock radius of the $11.2 M_{\odot}$ model favors the growth of convection. Figures 6.10 displays the critical parameter

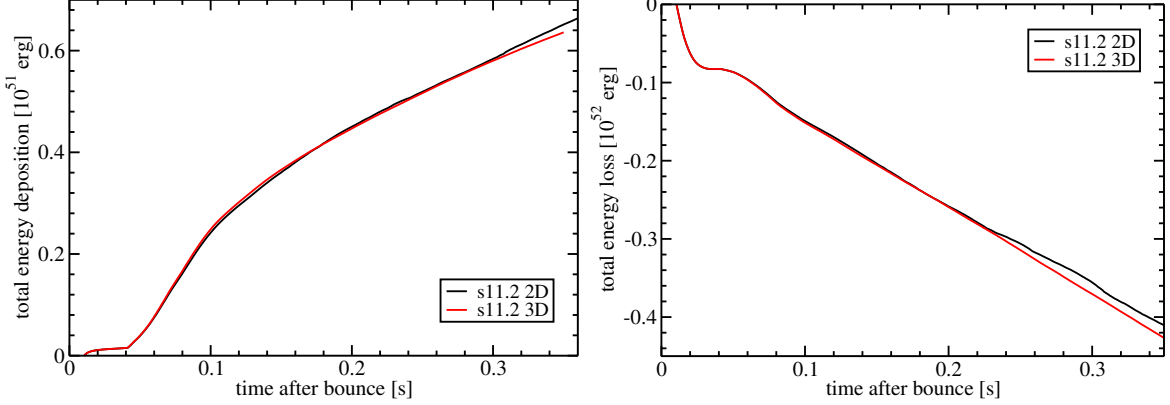


Figure 6.6: Time evolution of the total (time-integrated) energy deposited in the gain region (upper panel) and of the total energy loss (lower panel) for the $11.2 M_{\odot}$ SN progenitor. The 3D results (red) are shown together with the corresponding 2D run (black).

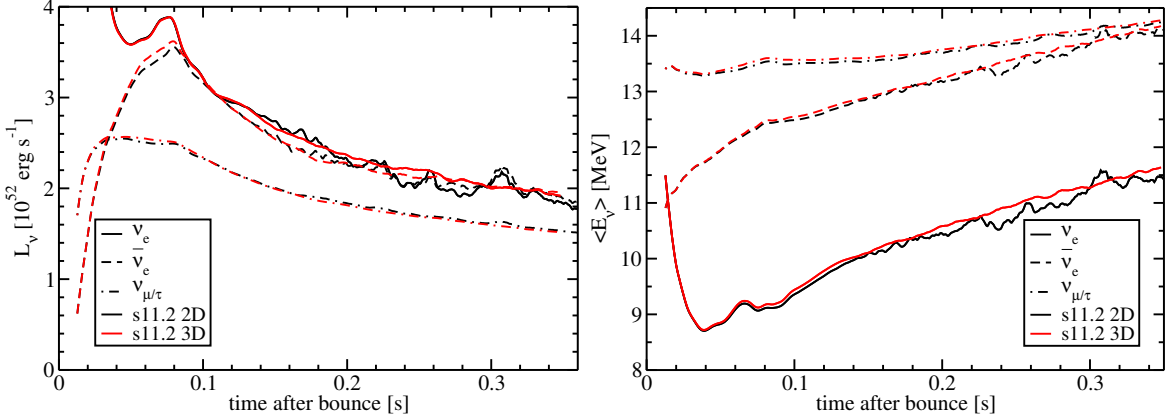


Figure 6.7: Time evolution of neutrino luminosities (ν_e solid, $\bar{\nu}_e$ dashed, and $\nu_{\mu/\tau}$ dashed-dotted) as function of time after bounce for the $11.2 M_{\odot}$ SN progenitor. The 3D result is depicted by the red curve and the corresponding 2D run in black. Note that the curves have been smoothed using a running average over 5 ms.

Figure 6.8: Time evolution of neutrino mean energies (ν_e solid, $\bar{\nu}_e$ dashed, and $\nu_{\mu/\tau}$ dashed-dotted) as function of time after bounce for the $11.2 M_{\odot}$ SN progenitor. The 3D result is depicted by the red curve and the corresponding 2D run in black. Note that the curves have been smoothed using a running average over 5 ms.

χ for the growth of convection evaluated according to Equation 3.19. Although $\chi < 3$ signals convective stability (Foglizzo et al. 2006), initiated by the initial random perturbations buoyant plumes develop and rise towards the shock. The bubbles are initially small and successively replaced by larger ones (Figures 6.1 and 6.2). Surprisingly, the critical parameter χ , although increasing, remains obviously below the threshold value for convective activity of Foglizzo et al. (2006) during the whole simulation of the 3D model. This fact is an indication of insufficient bubble growth, although Müller et al. (2012a) emphasized that the criterion for convective activity derived by Foglizzo et al. (2006) is only valid in the linear regime and cannot be applied for postshock flows significantly perturbed by aspherical mass motions. While in the respective 2D case the condition $\chi > 3$ indicates that convection has developed

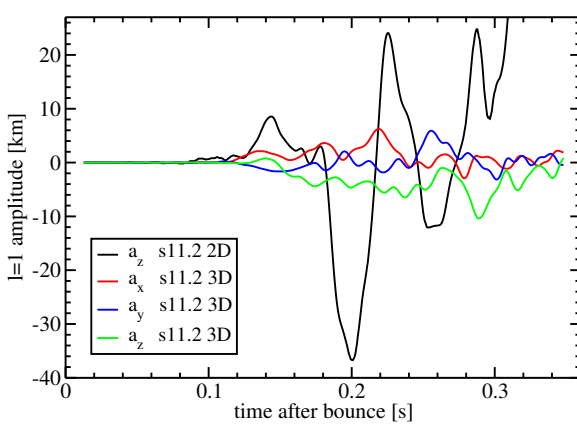


Figure 6.9: Time evolution of the first coefficient of the spherical harmonics expansion of the shock surface a_1 as function of time after bounce for the $11.2 M_{\odot}$ SN progenitor. The 3D result is depicted by the red curve and the corresponding 2D run in black. Note that the curves have been smoothed using a running average over 5 ms.

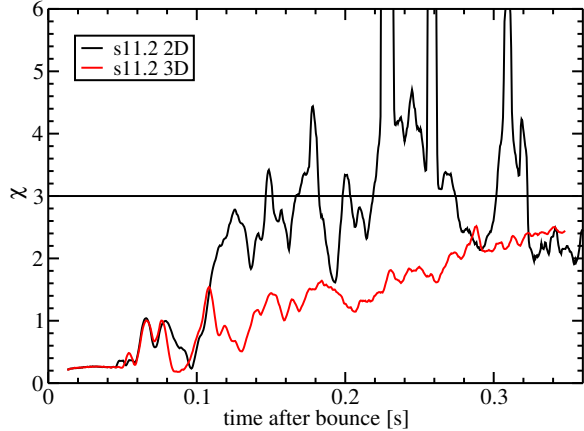


Figure 6.10: Time evolution of the stability parameter χ for the gain layer as function of time after bounce for the $11.2 M_{\odot}$ SN progenitor. The 3D result is depicted by the red curve and the corresponding 2D run in black. Note that the curves have been smoothed using a running average over 5 ms.

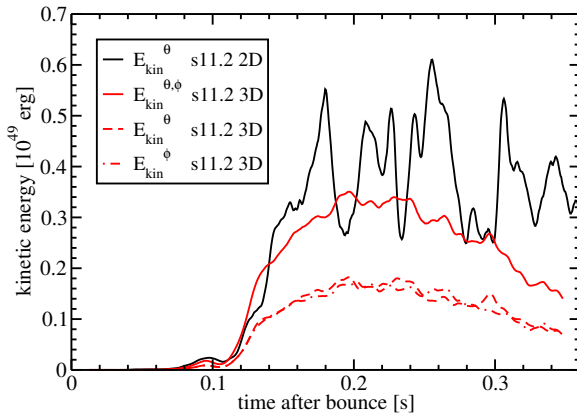


Figure 6.11: Time evolution of the kinetic energy of lateral mass motions in the gain layer for the 2D (black) and 3D (red) simulations of the $11.2 M_{\odot}$ SN progenitor. The runaway criterion is smoothed using a running average over 5 ms.

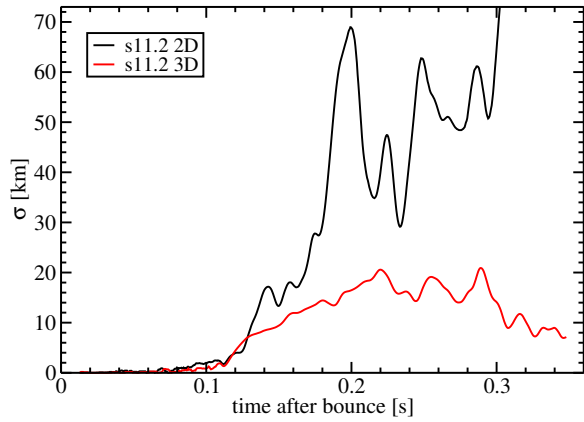


Figure 6.12: Time evolution of the rms shock deformation σ as function of time after bounce for the $11.2 M_{\odot}$ SN progenitor. The 3D result is depicted by the red curve and the corresponding 2D run in black. Note that the curves have been smoothed using a running average over 5 ms.

its full strength at about 140 ms, the bubble growth in the 3D case is not enough for sufficient shock expansion. For a discussion of the different growth of buoyant bubbles in 2D and 3D giving reasons for the failure of our 3D models we refer to Section 5.6. The overall stronger convective activity of the 2D model is reflected by the kinetic energies of non-radial mass motions (Figures 6.11), which are larger for the whole postbounce evolution in the 2D case.

In 3D, the strength of non-radial mass motion weakens at 210 ms, when the shock surface reaches its maximal extension and shrinks afterwards.

As the images of the entropy distribution in Figures 6.1 and 6.2 displays, the size of buoyant bubbles is locally very different and the shock surface is enlarged at angular positions, where large bubbles rise faster pushing the shock locally outwards. As the ratio of maximum to minimum shock radius reaches a maximum of up to $R_{s,\text{max}}/R_{s,\text{min}} \sim 1.4$, the root-mean-square deviation σ (Equation 5.5 in Section 5.2) provides further confirmation that the shock is significantly deformed by the rise of buoyant plumes (Figures 6.12). The value for this convective model is as large as for the $20 M_{\odot}$ progenitor during its phase of vigorous SASI activity (see Figures 5.8, right panel). Indeed, a global, quasi-stationary dipolar deformation of the accretion shock establishes, which is connected to a persistent asymmetry of electron neutrino and electron anti-neutrino fluxes in one hemisphere, i.e. an asymmetry in the lepton-number emission. However, in this thesis we focus on differences in the postbounce evolution between 2D and 3D models, and we refer the reader to the respective publication of Tamborra et al. (2014), which explains the subtle mechanism of this spectacular phenomenon visible in this model termed LESA for “Lepton-number Emission Self-sustained Asymmetry”.

7 Summary and Conclusions

In this thesis, we have presented a variety of multi-dimensional simulations of core-collapse supernovae employing the neutrino radiation-hydrodynamics code VERTEX-PROMETHEUS. With the help of the performed simulations, we have gained further insight into the explosion mechanism of massive stars towards a finally comprehensive understanding of this spectacular phenomenon. Until the advent of the newest generation of supercomputing systems, neutrino radiation-hydrodynamics simulations have long been forced to assume axisymmetry (2D), since simulations without any symmetry restrictions are computationally very expensive. To overcome the artificial imposition of 2D symmetry, in which the turbulent energy cascade is reversed and hydrodynamic instabilities are artificially amplified along the axis, we have extended the 2D VERTEX-PROMETHEUS code of Buras et al. (2006a) to a 3D version to be able to perform the first fully self-consistent simulations of core-collapse supernovae without any symmetry restrictions.

Before turning to the main results of this thesis, in a first step, we have performed a large set of axisymmetric simulations to prove the viability of the neutrino-driven explosion mechanism for a great number of stellar progenitors. As eighteen different massive stars could be evolved into the explosion phase, we have significantly increased the amount of successful explosion models compared to previous studies with the same level of accuracy (Buras et al. 2006a,b; Marek & Janka 2009; Müller et al. 2012b,a). This promising outcome of our set of simulation runs is a great success.

Contrary to the results of Bruenn et al. (2013), our 2D models explode rather late and at completely different postbounce times strongly depending on the specific progenitor structure. The explosion sets in faster for models, which experience a steep drop of the mass accretion rate on the supernova shock at the arrival of a strong Si/SiO composition-shell interface. Stars without such a pronounced shell interface, especially the lighter investigated ones in the mass range between twelve and fourteen solar masses, meet the conditions for shock revival very late.

In the presented axisymmetric simulations, the growth of the so-called “standing-accretion shock instability” (SASI; Blondin et al. 2003) is favored. It manifests in large-scale mass motions in the postshock layer associated with low-mode oscillations of the supernova shock front along the symmetry axis. This instability supports the growth of large bubbles, which finally initiates the shock expansion.

Our set of self-consistent simulations in axisymmetry demonstrated the importance of non-radial hydrodynamic instabilities, such as convection and the SASI, for reviving the stalled supernova shock. However, overcoming this forced symmetry, the fluid dynamics in the postshock layer will change fundamentally. For this reason, in this thesis we have presented the first three-dimensional simulations of core-collapse supernova explosions with full neutrino

transport performed with the same level of accuracy as in the presented 2D simulations. This important step in the numerical modeling of core-collapse supernova explosions allows a deeper insight into the crucial ingredients for the neutrino-driven mechanism:

The presented 3D simulations of the $27 M_{\odot}$ progenitor of Woosley et al. (2002) and of the $20 M_{\odot}$ progenitor of Woosley & Heger (2007) for the first time provide unambiguous evidence of the occurrence of large-amplitude SASI shock sloshing and spiral motions in a fully self-consistent setup. Our findings demonstrate the importance of the SASI also in 3D. This instability can become the clearly strongest nonradial instability during at least some parts of the evolution. Because of the absence of a flow-constraining symmetry axis, SASI shock motions can be recognized and distinguished from neutrino-driven buoyancy more easily and more readily in the 3D case. Interestingly, both 3D models exhibits evolution phases in which the SASI in 3D can become stronger than in the corresponding 2D runs. In phases of strongest shock recession the SASI sloshing motions change over to a spiral mode in the 3D simulations of both the $27 M_{\odot}$ and the $20 M_{\odot}$ model. As also observed in the late-time SASI activity, particularly small shock radii are favorable for the development of a spiral mode associated with its rotating shock-deformation pattern.

As the growth of the SASI is favored by fast advection flows (Scheck et al. 2008), in our 3D simulations of both the $27 M_{\odot}$ and the $20 M_{\odot}$ models SASI activity is strongest in phases of small shock stagnation radii and thus, short advection timescales. As the dependence of neutrino-driven buoyancy on the advection timescale is opposite (Foglizzo et al. 2006), in phases of strong SASI activity convection is almost absent. As the SASI pushes the shock front farther out, it dies off and convection becomes active in our 3D models.

To continue studying the dependence of both crucial instabilities in the supernova core, convection and the SASI, we have presented a further 3D simulation of the $11.2 M_{\odot}$ progenitor of Woosley et al. (2002). As in this model the mass accretion rate on the supernova shock front is very low resulting in a slow advection flow. Thus, convection dominates and SASI activity is absent.

Unfortunately, all investigated 3D models fail to explode. Although the 3D models evolve very similar to the corresponding 2D runs for hundreds of milliseconds after the core bounce, the difference in the explosion behavior is remarkable. This negative result is fully consistent with the findings of Hanke et al. (2012) and Couch (2013) based on simplified simulations. As the shock expansion initiated by the SASI leads to unfavorable conditions for the advective-acoustic cycle feeding the SASI, neutrino-driven buoyancy must take over to finally initiate successful shock revival. Along the lines of the findings of Dolence et al. (2013) and Couch (2013), we have demonstrated that the growth and rise of large buoyant bubbles to push the shock front further out is facilitated in 2D. Reasons for an easier growth of large buoyant plumes in 2D conducive to the explosion are the inverse turbulent energy cascade erroneously pumping energy from small to large scales (Kraichnan 1967), the more fragmented postshock flow in 3D compared to artificially large coherent entropy structures in 2D, and finally the unfavorable volume-to-surface ratio of a buoyant bubble in 3D.

This first generation of three-dimensional simulations of core-collapse supernovae employing the full neutrino transport provides new insight into the effects of the 3D postbounce dynamics on observable supernova signals, for example the neutrino emission. The presence of SASI mass motions in the $27 M_{\odot}$ and the $20 M_{\odot}$ models leads to large-amplitude, quasi-periodical

modulations of the neutrino emission, which could be detectable for a future galactic supernova (Tamborra et al. 2013). Lower-mass stellar core-collapse events, such as the investigated $11.2 M_{\odot}$ progenitor case, are dominated by neutrino-driven convection and lead only to small, stochastic fluctuations in the neutrino signal. Furthermore, analyzing the neutrino emission of this latter progenitor, we discovered a completely unexpected instability, which manifests in a long-lasting, global, dipolar asymmetry of the emission of electron neutrinos and antineutrinos (Tamborra et al. 2014). With respect to these first very exciting results of the analysis of the presented 3D simulations, our results provide the so far most realistic simulation data, which can be used to predict observable supernova signals, such as the already investigated neutrino signal and gravitational wave emission.

This thesis is an important step towards a more complete understanding of the underlying explosion mechanism of core-collapse supernovae. Of course, a lot of work remains to be done to further investigate the crucial effects for successful and robust supernova explosions. The newly developed 3D version of the neutrino radiation-hydrodynamics code VERTEX-PROMETHEUS provides an ideal tool to accurately study the missing ingredients, such as new nuclear equation of states for neutron star matter, updated neutrino-matter-interaction rates, the possible supportive effect of stellar core rotation (Nakamura et al. 2014; Iwakami et al. 2014), the influence of initial presupernova asperities (Couch & Ott 2013), and finally different progenitor structures as investigated in our study with axisymmetric simulations.

Bibliography

- Arnett, W. D., Bahcall, J. N., Kirshner, R. P., & Woosley, S. E. 1989, ARA&A, 27, 629
- Bethe, H. A. 1990, Reviews of Modern Physics, 62, 801
- Bethe, H. A. 1993, ApJ, 412, 192
- Blondin, J. M. & Mezzacappa, A. 2006, ApJ, 642, 401
- Blondin, J. M. & Mezzacappa, A. 2007, Nature, 445, 58
- Blondin, J. M., Mezzacappa, A., & DeMarino, C. 2003, ApJ, 584, 971
- Bruenn, S. W. 1985, ApJS, 58, 771
- Bruenn, S. W. 1987, Physical Review Letters, 59, 938
- Bruenn, S. W. 1993, in Nuclear Physics in the Universe, Ed. Guidry, M. W. and Strayer, M. R., 31–50
- Bruenn, S. W., Mezzacappa, A., Hix, W. R., et al. 2013, ApJ, 767, L6
- Buras, R., Janka, H.-T., Keil, M. T., Raffelt, G. G., & Rampp, M. 2003a, ApJ, 587, 320
- Buras, R., Janka, H.-T., Rampp, M., & Kifonidis, K. 2006b, A&A, 457, 281
- Buras, R., Rampp, M., Janka, H.-T., & Kifonidis, K. 2003b, Physical Review Letters, 90, 241101
- Buras, R., Rampp, M., Janka, H.-T., & Kifonidis, K. 2006a, A&A, 447, 1049
- Burrows, A. 2013, Reviews of Modern Physics, 85, 245
- Burrows, A., Dolence, J. C., & Murphy, J. W. 2012, ApJ, 759, 5
- Burrows, A. & Fryxell, B. A. 1992, Science, 258, 430
- Burrows, A. & Goshy, J. 1993, ApJ, 416, L75+
- Burrows, A., Hayes, J., & Fryxell, B. A. 1995, ApJ, 450, 830
- Burrows, A. & Sawyer, R. F. 1998, Phys. Rev. C, 58, 554
- Cernohorsky, J. 1994, ApJ, 433, 247
- Colella, P. & Glaz, H. M. 1985, Journal of Computational Physics, 59, 264

- Colella, P. & Woodward, P. R. 1984, *Journal of Computational Physics*, 54, 174
- Colgate, S. A. & White, R. H. 1966, *ApJ*, 143, 626
- Couch, S. M. 2013, *ApJ*, 775, 35
- Couch, S. M. & O'Connor, E. P. 2013, ArXiv:1310.5728
- Couch, S. M. & Ott, C. D. 2013, *ApJ*, 778, L7
- Courant, R., Friedrichs, K. O., & Lewy, H. 1928, *Math. Ann.*, 100, 32
- Demorest, P. B., Pennucci, T., Ransom, S. M., Roberts, M. S. E., & Hessels, J. W. T. 2010, *Nature*, 467, 1081
- Dolence, J. C., Burrows, A., Murphy, J. W., & Nordhaus, J. 2013, *ApJ*, 765, 110
- Einfeldt, B. 1988, *SIAM Journal on Numerical Analysis*, 25, 294
- Fernández, R. 2010, *ApJ*, 725, 1563
- Fernández, R. 2012, *ApJ*, 749, 142
- Fernández, R., Müller, B., Foglizzo, T., & Janka, H.-T. 2013, ArXiv:1310.0469
- Fernández, R. & Thompson, C. 2009a, *ApJ*, 703, 1464
- Fernández, R. & Thompson, C. 2009b, *ApJ*, 697, 1827
- Foglizzo, T. 2002, *A&A*, 392, 353
- Foglizzo, T., Galletti, P., Scheck, L., & Janka, H.-T. 2007, *ApJ*, 654, 1006
- Foglizzo, T., Masset, F., Guilet, J., & Durand, G. 2012, *Physical Review Letters*, 108, 051103
- Foglizzo, T., Scheck, L., & Janka, H.-T. 2006, *ApJ*, 652, 1436
- Fryer, C. L. & Heger, A. 2000, *ApJ*, 541, 1033
- Fryxell, B., Müller, E., & Arnett, W. 1989, *Hydrodynamics and Nuclear Burning*, preprint MPA-449, Max Planck Institut für Astrophysik, Garching
- Fryxell, B., Olson, K., Ricker, P., et al. 2000, *ApJS*, 131, 273
- Godunov, S. K. 1959, *Matematicheskii Sbornik*, 47, 271
- Guilet, J. & Fernández, R. 2013, ArXiv:1310.2616
- Guilet, J. & Foglizzo, T. 2012, *MNRAS*, 421, 546
- Hammer, N. J., Janka, H., & Müller, E. 2010, *ApJ*, 714, 1371
- Hanke, F. 2010, Diplomarbeit, Technische Universität München
- Hanke, F., Marek, A., Müller, B., & Janka, H.-T. 2012, *ApJ*, 755, 138

- Hanke, F., Müller, B., Wongwathanarat, A., Marek, A., & Janka, H.-T. 2013, ApJ, 770, 66
- Hannestad, S. & Raffelt, G. 1998, ApJ, 507, 339
- Hebeler, K., Lattimer, J. M., Pethick, C. J., & Schwenk, A. 2010, Physical Review Letters, 105, 161102
- Hebeler, K., Lattimer, J. M., Pethick, C. J., & Schwenk, A. 2013, ApJ, 773, 11
- Hempel, M., Fischer, T., Schaffner-Bielich, J., & Liebendörfer, M. 2012, ApJ, 748, 70
- Herant, M., Benz, W., & Colgate, S. 1992, ApJ, 395, 642
- Herant, M., Benz, W., Hix, W. R., Fryer, C. L., & Colgate, S. A. 1994, ApJ, 435, 339
- Hillebrandt, W., Höflich, P., Janka, H.-T., & Mönchmeyer, R. 1989, in Big Bang, Active Galactic Nuclei and Supernovae, Ed. Hayakawa, S. and Sato, K., 441
- Horowitz, C. J. 1997, Phys. Rev. D, 55, 4577
- Horowitz, C. J. 2002, Phys. Rev. D, 65, 043001
- Iwakami, W., Kotake, K., Ohnishi, N., Yamada, S., & Sawada, K. 2008, ApJ, 678, 1207
- Iwakami, W., Kotake, K., Ohnishi, N., Yamada, S., & Sawada, K. 2009, ApJ, 700, 232
- Iwakami, W., Nagakura, H., & Yamada, S. 2014, ArXiv e-prints
- Janka, H.-T. 1999, unpublished
- Janka, H.-T. 2001, A&A, 368, 527
- Janka, H.-T. 2012, Annual Review of Nuclear and Particle Science, 62, 407
- Janka, H.-T., Hanke, F., Hüdepohl, L., et al. 2012, Progress of Theoretical and Experimental Physics, 2012, 010000
- Janka, H.-T., Langanke, K., Marek, A., Martínez-Pinedo, G., & Müller, B. 2007, Phys. Rep., 442, 38
- Janka, H.-T. & Mueller, E. 1995, ApJ, 448, L109+
- Janka, H.-T. & Müller, E. 1996, A&A, 306, 167
- Keil, W. 1997, PhD thesis, Technische Universität München
- Kifonidis, K., Plewa, T., Janka, H.-T., & Müller, E. 2003, A&A, 408, 621
- Kifonidis, K., Plewa, T., Scheck, L., Janka, H.-T., & Müller, E. 2006, A&A, 453, 661
- Kitaura, F. S., Janka, H.-T., & Hillebrandt, W. 2006, A&A, 450, 345
- Kolmogorov, A. 1941, Akademii Nauk SSSR Doklady, 30, 301
- Kotake, K., Sumiyoshi, K., Yamada, S., et al. 2012, Progress of Theoretical and Experimental Physics, 2012, 010000

- Kraichnan, R. H. 1967, Physics of Fluids, 10, 1417
- Kuroda, T., Kotake, K., & Takiwaki, T. 2012, ApJ, 755, 11
- Laming, J. M. 2007, ApJ, 659, 1449
- Landau, L. D. & Lifshitz, E. M. 1959, Fluid mechanics
- Langanke, K., Martínez-Pinedo, G., Sampaio, J. M., et al. 2003, Physical Review Letters, 90, 241102
- Langanke, K., Martínez-Pinedo, G., Müller, B., et al. 2008, Physical Review Letters, 100, 011101
- Lattimer, J. M., Pethick, C. J., Ravenhall, D. G., & Lamb, D. Q. 1985, Nuclear Physics A, 432, 646
- Lattimer, J. M. & Prakash, M. 2010, ArXiv:1012.3208
- Lattimer, J. M. & Swesty, F. D. 1991, Nuclear Physics A, 535, 331
- Liebendörfer, M., Messer, O. E. B., Mezzacappa, A., & Hix, W. R. 2001, in American Institute of Physics Conference Series, Vol. 586, 20th Texas Symposium on relativistic astrophysics, ed. J. C. Wheeler & H. Martel (American Institute of Physics), 472–477
- Liebendörfer, M., Rampp, M., Janka, H.-T., & Mezzacappa, A. 2005, ApJ, 620, 840
- Marek, A., Dimmelmeier, H., Janka, H.-T., Müller, E., & Buras, R. 2006, A&A, 445, 273
- Marek, A. & Janka, H.-T. 2009, ApJ, 694, 664
- McCray, R. 1993, ARA&A, 31, 175
- Mezzacappa, A. & Bruenn, S. W. 1993a, ApJ, 410, 740
- Mezzacappa, A. & Bruenn, S. W. 1993b, ApJ, 405, 637
- Mezzacappa, A., Liebendörfer, M., Messer, O. E., et al. 2001, Physical Review Letters, 86, 1935
- Mihalas, D. & Mihalas, B. 1984, Foundations of Radiation Hydrodynamics (Oxford University Press)
- Müller, B., Janka, H., & Dimmelmeier, H. 2010, ApJS, 189, 104
- Müller, B. & Janka, H.-T. 2014, in preparation
- Müller, B., Janka, H.-T., & Heger, A. 2012a, ApJ, 761, 72
- Müller, B., Janka, H.-T., & Marek, A. 2012b, ApJ, 756, 84
- Müller, B., Janka, H.-T., & Marek, A. 2013, ApJ, 766, 43
- Müller, E. 1998, Simulation of Astrophysical Fluid Flow, ed. O. Steiner & A. Gautschy, 343–+

- Müller, E. & Janka, H.-T. 1997, A&A, 317, 140
- Müller, E., Janka, H.-T., & Wongwathanarat, A. 2012c, A&A, 537, A63
- Müller, E. & Steinmetz, M. 1995, Computer Physics Communications, 89, 45
- Murphy, J. W. & Burrows, A. 2008, ApJ, 688, 1159
- Murphy, J. W., Dolence, J. C., & Burrows, A. 2013, ApJ, 771, 52
- Murphy, J. W. & Meakin, C. 2011, ApJ, 742, 74
- Nakamura, K., Kuroda, T., Takiwaki, T., & Kotake, K. 2014, ArXiv e-prints
- Nomoto, K. 1987, ApJ, 322, 206
- Nomoto, K., Shigeyama, T., Kumagai, S., Yamaoka, H., & Suzuki, T. 1994, in Supernovae, Ed. Bludman, S. A. and Mochkovitch, R. and Zinn-Justin, J., 489–+
- Nordhaus, J., Burrows, A., Almgren, A., & Bell, J. 2010, ApJ, 720, 694
- O'Connor, E. & Ott, C. D. 2011, ApJ, 730, 70
- O'Connor, E. & Ott, C. D. 2013, ApJ, 762, 126
- Ohnishi, N., Kotake, K., & Yamada, S. 2006, ApJ, 641, 1018
- Ott, C. D., Abdikamalov, E., Mösta, P., et al. 2013, ApJ, 768, 115
- Pejcha, O. & Thompson, T. A. 2012, ApJ, 746, 106
- Plewa, T. & Müller, E. 1999, A&A, 342, 179
- Pons, J. A., Miralles, J. A., & Ibanez, J. M. A. 1998, A&AS, 129, 343
- Quirk, J. J. 1994, International Journal for Numerical Methods in Fluids, 18, 555
- Rampp, M. & Janka, H.-T. 2000, ApJ, 539, L33
- Rampp, M. & Janka, H.-T. 2002, A&A, 396, 361
- Scheck, L., Janka, H.-T., Foglizzo, T., & Kifonidis, K. 2008, A&A, 477, 931
- Scheck, L., Kifonidis, K., Janka, H.-T., & Müller, E. 2006, A&A, 457, 963
- Shlomo, S., Kolomietz, V. M., & Colò, G. 2006, European Physical Journal A, 30, 23
- Smartt, S. J. 2009, ARA&A, 47, 63
- Steiner, A. W., Hempel, M., & Fischer, T. 2013, ApJ, 774, 17
- Steiner, A. W., Lattimer, J. M., & Brown, E. F. 2010, ApJ, 722, 33
- Sumiyoshi, K. & Yamada, S. 2012, in IAU Symposium, Vol. 279, Death of Massive Stars: Supernovae and Gamma-Ray Bursts, 395–396

- Suwa, Y., Kotake, K., Takiwaki, T., et al. 2010, PASJ, 62, L49
- Takiwaki, T., Kotake, K., & Suwa, Y. 2012, ApJ, 749, 98
- Takiwaki, T., Kotake, K., & Suwa, Y. 2013, ArXiv:1308.5755
- Tamborra, I., Hanke, F., Janka, H.-T., et al. 2014, ArXiv:1402.5418
- Tamborra, I., Hanke, F., Müller, B., Janka, H.-T., & Raffelt, G. 2013, Physical Review Letters, 111, 121104
- Tanaka, M., Tominaga, N., Nomoto, K., et al. 2009, ApJ, 692, 1131
- Thompson, T. A., Burrows, A., & Pinto, P. A. 2003, ApJ, 592, 434
- Thompson, T. A., Quataert, E., & Burrows, A. 2005, ApJ, 620, 861
- Uglian, M., Janka, H.-T., Marek, A., & Arcones, A. 2012, ApJ, 757, 69
- Utrobin, V. P. & Chugai, N. N. 2011, A&A, 532, A100
- Wongwathanarat, A., Janka, H.-T., & Müller, E. 2010, ApJ, 725, L106
- Wongwathanarat, A., Janka, H.-T., & Müller, E. 2013, A&A, 552, A126
- Woosley, S. E. & Heger, A. 2007, Phys. Rep., 442, 269
- Woosley, S. E., Heger, A., & Weaver, T. A. 2002, Reviews of Modern Physics, 74, 1015
- Yamasaki, T. & Foglizzo, T. 2008, ApJ, 679, 607
- Yamasaki, T. & Yamada, S. 2007, ApJ, 656, 1019